CHAPTER

5

Radar Scattering

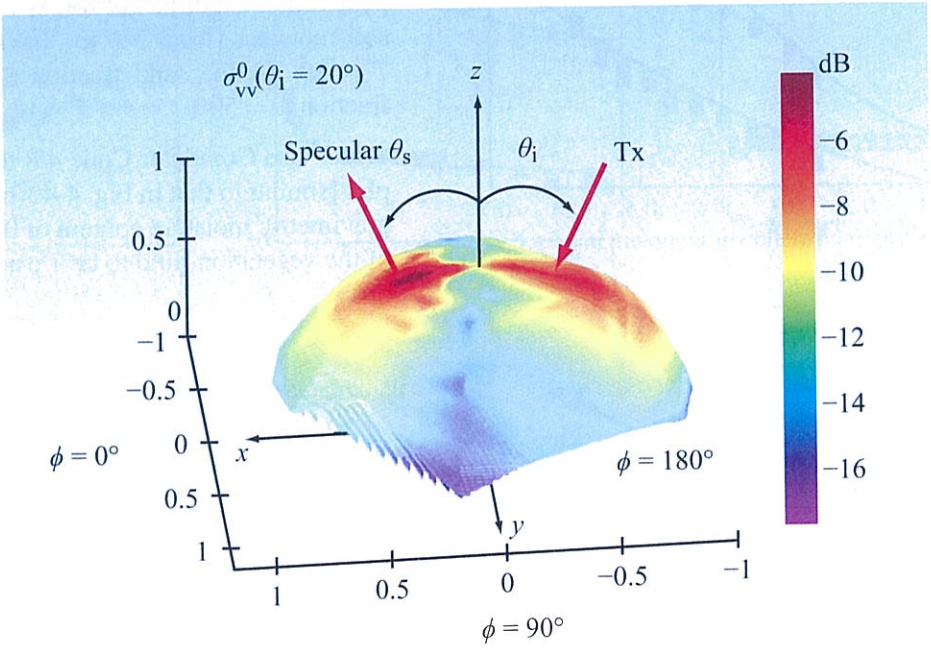

Bistatic scattering

CONTENTS

Overview

This chapter establishes the framework and associated terminology for how electromagnetic waves are scattered by point and distributed targets, the role of wave polarization, and how polarimetric radar can capture the full polarimetric response of the target. In the language of radar, any object "seen" by its antenna beam is called a "target," it is called a ***point target*** if it is self-contained—such as a car or aircraft, and it is called a ***distributed target*** if it is terrain-like.

5-1 Wave Polarization in a Spherical Coordinate System

The polarization of a plane wave describes the shape traced by the tip of its electric field in a plane orthogonal to the direction of propagation, as the wave passes through that plane. In Section 2-3, we examined the properties of linear, circular, and elliptical polarizations for a wave traveling in the z direction in a Cartesian (x,y,z) system. Orthogonality required $\mathbf{E}$ to reside in the x–y plane. When modeling radar scattering from the earth's surface, it is more convenient to represent the earth's surface by the x–y plane and to represent the polarization vector $\mathbf{E}$ of waves incident upon or scattered from the surface in terms of the spherical angles θ and ϕ. For a plane EM wave traveling in the direction $\hat{\mathbf{k}}$, as shown in Fig. 5-1, its electric field phasor $\mathbf{E}$ consists of a ***horizontal polarization*** component, $\hat{\mathbf{h}}E_\mathrm{h}$, and a ***vertical polarization*** component, $\hat{\mathbf{v}}E_\mathrm{v}$, defined such that the coordinate system $(\hat{\mathbf{k}},\hat{\mathbf{v}},\hat{\mathbf{h}})$ coincides with $(\hat{\mathbf{R}},\hat{\boldsymbol{\theta}},\hat{\boldsymbol{\phi}})$ of a standard spherical coordinate system. Thus, in a medium with wave number $k = 2\pi/\lambda$,

$$\mathbf{E} = (\hat{\mathbf{v}}E_\mathrm{v} + \hat{\mathbf{h}}E_\mathrm{h})e^{-jk\hat{\mathbf{k}}\cdot\hat{\mathbf{R}}}, \tag{5.1}$$

with

$$\hat{\mathbf{k}} = \hat{\mathbf{x}}\sin\theta\cos\phi + \hat{\mathbf{y}}\sin\theta\sin\phi + \hat{\mathbf{z}}\cos\theta, \tag{5.2a}$$

$$\hat{\mathbf{h}} = \frac{\hat{\mathbf{z}}\times\hat{\mathbf{k}}}{|\hat{\mathbf{z}}\times\hat{\mathbf{k}}|} = -\hat{\mathbf{x}}\sin\phi + \hat{\mathbf{y}}\cos\phi, \tag{5.2b}$$

and

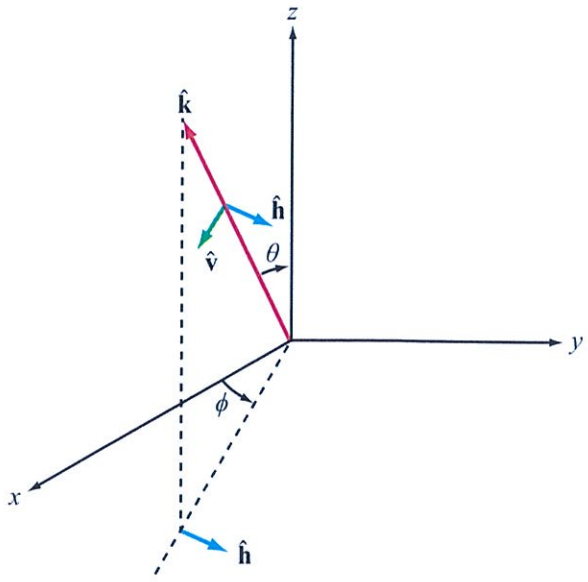

Figure 5-1: Spherical coordinate system for a wave traveling in the $\hat{\mathbf{k}}$ direction.

$$\hat{\mathbf{v}} = \hat{\mathbf{h}}\times\hat{\mathbf{k}} = \hat{\mathbf{x}}\cos\theta\cos\phi + \hat{\mathbf{y}}\cos\theta\sin\phi - \hat{\mathbf{z}}\sin\theta. \tag{5.2c}$$

In future sections, we use the matrix notation for $\mathbf{E}$ as

$$\mathbf{E} = \begin{bmatrix} E_\mathrm{v} \\ E_\mathrm{h} \end{bmatrix}, \tag{5.3}$$

where it is understood that E_v and E_h are the ***complex amplitudes*** of $\mathbf{E}$ along $\hat{\mathbf{v}}$ and $\hat{\mathbf{h}}$, respectively, and associated with both components is a ***propagation phase factor*** $e^{-jk\hat{\mathbf{k}}\cdot\hat{\mathbf{R}}}$.

In Section 2-3, for a wave traveling in the z direction, its wave polarization was defined by the magnitudes and phases of its electric field complex amplitudes E_x and E_y. Conversion to the spherical coordinate system entails the simple change of subscripts from (x,y) to (v,h) in all of the expressions given in Section 2-3. Specifically,

$$E_\mathrm{v} = a_\mathrm{v}, \tag{5.4a}$$

$$E_\mathrm{h} = a_\mathrm{h}e^{j\delta}, \tag{5.4b}$$

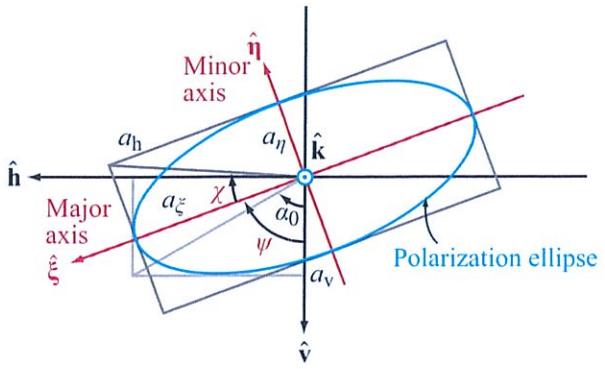

Figure 5-2: Polarization ellipse in the v–h plane for a wave traveling in the $\hat{\mathbf{k}}$ direction.

where $a_v = |E_v|$, $a_h = |E_h|$, and for convenience we assigned E_v a phase of zero. Thus, δ is the phase difference between the h and v components of $\mathbf{E}$.

If a_v, a_h, and δ all have nonzero values, the trace of the tip of $\mathbf{E}$ as a function of time (at a fixed R) forms an ellipse with rotation angle ψ and ellipticity angle χ (Fig. 5-2) given by

$$\tan 2\psi = (\tan 2\alpha_0)\cos\delta = \frac{2a_v a_h}{a_v^2 - a_h^2}\cos\delta \qquad (5.5a)$$

$$(-\pi/2 \le \psi \le \pi/2),$$

$$\sin 2\chi = (\sin 2\alpha_0)\sin\delta = \frac{2a_h a_v}{a_h^2 + a_v^2}\sin\delta \qquad (5.5b)$$

$$(-\pi/4 \le \chi \le \pi/4),$$

where α_0 is an auxiliary angle defined by

$$\tan\alpha_0 = \frac{a_h}{a_v}. \qquad (5.6)$$

For $\delta = 0$ or π, the ellipse collapses into a line and the wave polarization becomes linear, and if $\delta = \pm\pi/2$ and $a_v = a_h$, the polarization becomes circular (see Section 2-3).

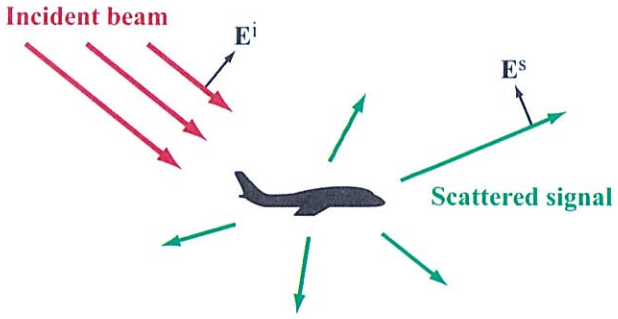

Figure 5-3: EM beam incident upon an object is scattered along many directions.

5-2 Scattering Coordinate Systems

When illuminated by a plane wave with electric field $\mathbf{E}^i$, an object (Fig. 5-3) absorbs part of the energy it intercepts and scatters the remainder along many directions. If the object is a perfect conductor, it can scatter energy but not absorb any of it. Associated with each scattered wave is an electric field $\mathbf{E}^s$ whose magnitude and direction (polarization) are related to the incident field $\mathbf{E}^i$, the shape and orientation of the object relative to the incident and scattered directions, and the electrical properties of the object (permittivity ε' and conductivity σ).

In its simplest form, a radar is an instrument that uses a transmit antenna to illuminate an object, as depicted by Fig. 5-4(a), and then intercepts and measures part of the scattered energy. The scenario shown in Fig. 5-4(a), in which the transmitter and receiver are at different locations, is called a ***bistatic radar*** configuration. Most radars, however, operate in the ***monostatic radar*** configuration shown in Fig. 5-4(b) wherein the transmitter and receiver are collocated, and in most cases the same antenna is used for both transmission and reception. The monostatic configuration also is known as the ***backscatter configuration*** because the receiver measures the energy *scattered back* towards the radar.

Scattering calculations are performed in two major types of coordinate systems, the ***forward scatter alignment*** (FSA) convention and the ***backscatter alignment*** (BSA) convention. In both cases, the electric fields

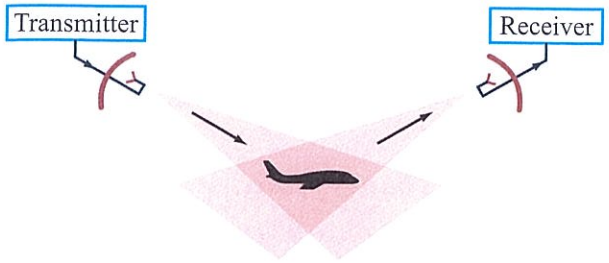

(a) Bistatic radar

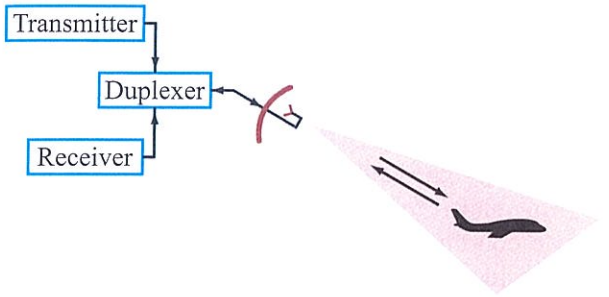

(b) Monostatic radar

Figure 5-4: The duplexer used by a monostatic radar allows the antenna to be shared between the transmitter and the receiver.

of the incident and scattered waves are expressed in local coordinate systems centered on the transmitting and receiving antennas, respectively. All coordinate systems are defined in terms of a global coordinate system centered inside the scattering object, as shown in Fig. 5-5.

Both conventions are used in the literature, with the FSA being the preferred system for problems involving bistatic scattering from particles and inhomogeneous media and the BSA being the preferred system for calculating the radar backscatter from a given target or medium. Because both conventions are used in this book, we define and interrelate their individual coordinate systems in the following subsections.

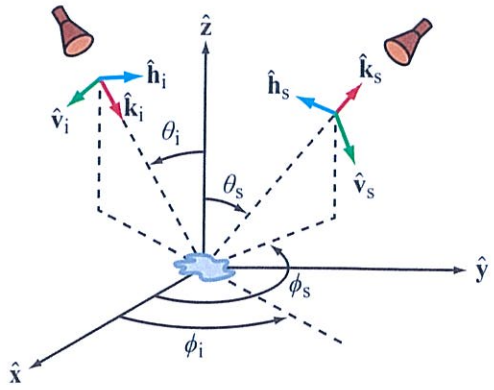

(a) FSA convention

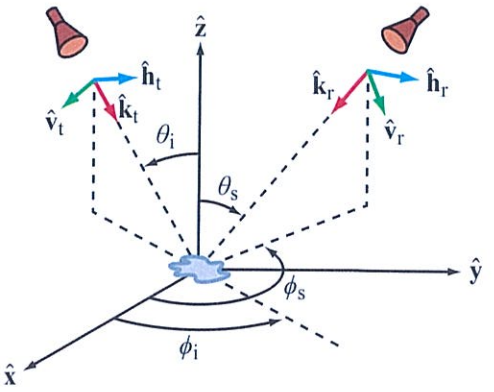

(b) BSA convention

Figure 5-5: Coordinate systems and scattering geometry for (a) the forward scattering alignment convention and (b) the backscatter alignment (BSA) convention.

5-2.1 Forward Scattering Alignment (FSA) Convention

FSA is a "wave-oriented" convention in that the directions of the vertical and horizontal unit vectors, $\hat{\mathbf{v}}$ and $\hat{\mathbf{h}}$, are always defined with respect to the direction of propagation of the wave, $\hat{\mathbf{k}}$. The coordinate system $(\hat{\mathbf{k}}, \hat{\mathbf{v}}, \hat{\mathbf{h}})$ is chosen to coincide with $(\hat{\mathbf{R}}, \boldsymbol{\theta}, \boldsymbol{\phi})$ in a standard spherical coordinate system, as shown earlier in Section

5-1. Thus, for a wave incident in the direction $\hat{\mathbf{k}}_i$ and scattered in the direction $\hat{\mathbf{k}}_s$, as shown in Fig. 5-5(a), the unit vectors are

$$\hat{\mathbf{k}}_i = \hat{\mathbf{x}}\cos\phi_i \sin\theta_i + \hat{\mathbf{y}}\sin\phi_i \sin\theta_i - \hat{\mathbf{z}}\cos\theta_i, \tag{5.7a}$$

$$\hat{\mathbf{h}}_i = \frac{\hat{\mathbf{z}} \times \hat{\mathbf{k}}_i}{|\hat{\mathbf{z}} \times \hat{\mathbf{k}}_i|} = -\hat{\mathbf{x}}\sin\phi_i + \hat{\mathbf{y}}\cos\phi_i, \tag{5.7b}$$

$$\begin{aligned}\hat{\mathbf{v}}_i &= \hat{\mathbf{h}}_i \times \hat{\mathbf{k}}_i \\ &= -\hat{\mathbf{x}}\cos\phi_i \cos\theta_i - \hat{\mathbf{y}}\sin\phi_i \cos\theta_i - \hat{\mathbf{z}}\sin\theta_i,\end{aligned} \tag{5.7c}$$

$$\hat{\mathbf{k}}_s = \hat{\mathbf{x}}\cos\phi_s \sin\theta_s + \hat{\mathbf{y}}\sin\phi_s \sin\theta_s + \hat{\mathbf{z}}\cos\theta_s, \tag{5.7d}$$

$$\hat{\mathbf{h}}_s = \frac{\hat{\mathbf{z}} \times \hat{\mathbf{k}}_s}{|\hat{\mathbf{z}} \times \hat{\mathbf{k}}_s|} = -\hat{\mathbf{x}}\sin\phi_s + \hat{\mathbf{y}}\cos\phi_s, \tag{5.7e}$$

$$\begin{aligned}\hat{\mathbf{v}}_s &= \hat{\mathbf{h}}_s \times \hat{\mathbf{k}}_s \\ &= \hat{\mathbf{x}}\cos\phi_s \cos\theta_s + \hat{\mathbf{y}}\sin\phi_s \cos\theta_s - \hat{\mathbf{z}}\sin\theta_s.\end{aligned} \tag{5.7f}$$

▶ In the FSA convention, the forward scattering direction corresponds to $\theta_s = \pi - \theta_i$ and $\phi_s = \phi_i$, and the backscattering direction corresponds to $\theta_s = \theta_i$ and $\phi_s = \phi_i + \pi$. ◀

For forward scattering, we have $\hat{\mathbf{k}}_s = \hat{\mathbf{k}}_i$, $\hat{\mathbf{v}}_s = \hat{\mathbf{v}}_i$, and $\hat{\mathbf{h}}_s = \hat{\mathbf{h}}_i$. In contrast, for backscattering, the relations are $\hat{\mathbf{k}}_s = -\hat{\mathbf{k}}_i$, $\hat{\mathbf{v}}_s = \hat{\mathbf{v}}_i$, $\hat{\mathbf{h}}_s = -\hat{\mathbf{h}}_i$. The direction of propagation $\hat{\mathbf{k}}_s$ is opposite to $\hat{\mathbf{k}}_i$, as expected, but only one of the two polarization vectors reverses direction upon backscattering.

5-2.2 Backscatter Alignment (BSA) Convention

In contrast to the FSA convention, in the BSA convention the polarization unit vectors are defined with respect to the radar antennas. This is in accordance with the standard convention that defines the polarization state of an antenna to be the polarization of the wave radiated by the antenna, even when it is used as a receiving antenna. Consequently, for the backscatter case under the BSA convention, the vertical and horizontal unit polarization vectors of the scattered wave are identical with their counterparts of the incident wave. The local coordinate system unit vectors are [Fig. 5-5(b)]:

$$\hat{\mathbf{k}}_t = \hat{\mathbf{k}}_i = \hat{\mathbf{x}}\cos\phi_i \sin\theta_i + \hat{\mathbf{y}}\sin\phi_i \sin\theta_i - \hat{\mathbf{z}}\cos\theta_i, \tag{5.8a}$$

$$\hat{\mathbf{h}}_t = \hat{\mathbf{h}}_i = -\hat{\mathbf{x}}\sin\phi_i + \hat{\mathbf{y}}\cos\phi_i, \tag{5.8b}$$

$$\hat{\mathbf{v}}_t = \hat{\mathbf{v}}_i = -\hat{\mathbf{x}}\cos\phi_i \cos\theta_i - \hat{\mathbf{y}}\sin\phi_i \cos\theta_i - \hat{\mathbf{z}}\sin\theta_i, \tag{5.8c}$$

$$\begin{aligned}\hat{\mathbf{k}}_r = -\hat{\mathbf{k}}_s = -[&\hat{\mathbf{x}}\cos(\phi_s)\sin(\theta_s) \\ &+ \hat{\mathbf{y}}\sin\phi_s \sin\theta_s + \hat{\mathbf{z}}\cos\theta_s],\end{aligned} \tag{5.8d}$$

$$\hat{\mathbf{h}}_r = -\hat{\mathbf{h}}_s = \hat{\mathbf{x}}\sin\phi_s - \hat{\mathbf{y}}\cos\phi_s, \tag{5.8e}$$

$$\hat{\mathbf{v}}_r = \hat{\mathbf{v}}_s = \hat{\mathbf{x}}\cos\phi_s \cos\theta_s + \hat{\mathbf{y}}\sin\phi_s \cos\theta_s - \hat{\mathbf{z}}\sin\theta_s, \tag{5.8f}$$

where the subscripts t and r refer to the transmitting (or incident) and receiving antenna orientations. Because the two coordinates systems, $(\hat{\mathbf{k}}_t, \hat{\mathbf{v}}_t, \hat{\mathbf{h}}_t)$ and $(\hat{\mathbf{k}}_r, \hat{\mathbf{v}}_r, \hat{\mathbf{h}}_r)$, are coincident when the two antennas are collocated, the BSA convention has been the preferred system in the area of radar polarimetry (van Zyl et al., 1987a, b; Zebker et al., 1987).

To distinguish easily between the coordinate systems of the two conventions, we choose the subscripts i and s (which denote incident and scattered) for the FSA and the subscripts t and r (which denote transmitted and received) for the BSA convention. We must keep in mind, however, that the i coordinate system and the t coordinate systems are identical. To denote whether a given symbol represents a quantity that has been defined according to the FSA or BSA convention, we adopt the rule that a quantity is defined according to the FSA (or BSA) convention if its symbol has (or does not have) a tilde ($\sim$) over it.

▶ Thus, the scattering matrix $\widetilde{\mathbf{S}}$ introduced in the next section, for example, is defined in the FSA convention, whereas $\mathbf{S}$ is defined in the BSA convention. ◀

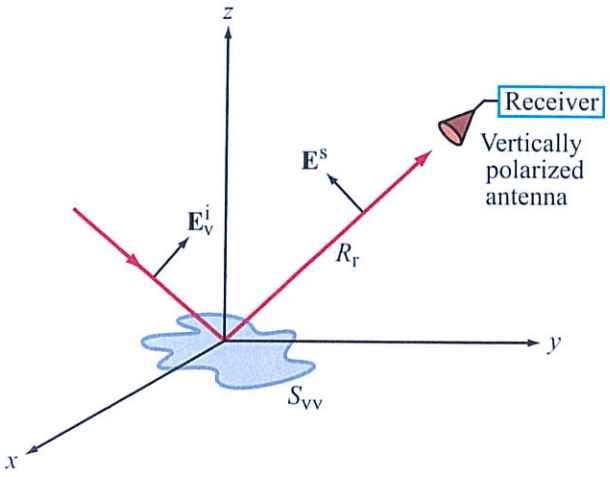

Figure 5-6: A vertically polarized incident wave E^i_v, defined at the location of the scattering object, generates a scattered wave with $\mathbf{E}^s$ defined at range R_r from the object. A vertically polarized receiving antenna measures $E^s_v = (e^{-jkR_r}/R_r)\widetilde{S}_{vv}E^i_v$.

5-3 Scattering Matrix

5-3.1 FSA Convention

Consider a small scattering object illuminated by a plane wave with incident electric field $\mathbf{E}^i = \hat{\mathbf{v}}_i E^i_v$ (Fig. 5-6). That is, $\mathbf{E}^i$ is vertically polarized. Moreover, *E^i_v is defined at the location of the object*. In the far zone of the scattering object, the scattered wave at a range R_r from the object is an outgoing spherical wave that can be approximated by a plane wave over the relatively small aperture of the receiving antenna. In general, the electric field $\mathbf{E}^s$ of the scattered wave consists of components along $\hat{\mathbf{v}}_s$ and $\hat{\mathbf{h}}_s$. If the antenna is vertically polarized, it will intercept only the vertically polarized component E^s_v, which is related to E^i_v by

$$E^s_v = \left(\frac{e^{-jkR_r}}{R_r}\right)\widetilde{S}_{vv}\,E^i_v \qquad \textbf{(vv polarization)}, \tag{5.9}$$

where (e^{-jkR_r}/R_r) is the spherical propagation factor and $\widetilde{S}_{vv}$ is the vv-polarized ***scattering amplitude*** of the scattering object, defined in the FSA convention.

▶ Scattering amplitude is denoted as:

$\widetilde{S}$ in FSA convention,
S in BSA convention. ◀

Similarly, had the receiving antenna been horizontally polarized instead, it would have measured the horizontal polarization component of $\mathbf{E}^s$, namely

$$E^s_h = \left(\frac{e^{-jkR_r}}{R_r}\right)\widetilde{S}_{hv}\,E^i_v \qquad \textbf{(hv polarization)}. \tag{5.10}$$

▶ Note that the first subscript of the scattering amplitude $\widetilde{S}_{pq}$ (where p and q may each be either v or h) refers to the polarization component of the scattered wave intercepted by the receive antenna and the second subscript refers to the polarization of the incident wave. ◀

In the general case, the incident wave may have both $\hat{\mathbf{h}}$ and $\hat{\mathbf{v}}$ polarization components, and the same is true for the scattered wave. That is,

$$\mathbf{E}^i = \hat{\mathbf{v}}_i E^i_v + \hat{\mathbf{h}}_i E^i_h, \tag{5.11a}$$

$$\mathbf{E}^s = \hat{\mathbf{v}}_s E^s_v + \hat{\mathbf{h}}_s E^s_h, \tag{5.11b}$$

and the two fields are related by

$$\begin{bmatrix} E^s_v \\ E^s_h \end{bmatrix} = \left(\frac{e^{-jkR_r}}{R_r}\right)\begin{bmatrix} \widetilde{S}_{vv} & \widetilde{S}_{vh} \\ \widetilde{S}_{hv} & \widetilde{S}_{hh} \end{bmatrix}\begin{bmatrix} E^i_v \\ E^i_h \end{bmatrix}. \tag{5.12}$$

The four scattering amplitudes characterize the scattering behavior of the object for the four possible combinations of the v and h polarization orientations of the incident and scattered fields. Each may be a real or complex quantity and may be a function of not only the target shape, size, orientation, permittivity, and conductivity, but also of the illumination and scattering angles, (θ_i, ϕ_i) and (θ_s, ϕ_s), respectively.

Equation (5.12) can be cast in the abbreviated form

$$\mathbf{E}^s = \left(\frac{e^{-jkR_r}}{R_r}\right)\widetilde{\mathbf{S}}\,\mathbf{E}^i, \tag{5.13}$$

where $\widetilde{\mathbf{S}}$ is the ***scattering matrix*** of the target in the FSA convention,

$$\widetilde{\mathbf{S}} = \begin{bmatrix} \widetilde{S}_{vv} & \widetilde{S}_{vh} \\ \widetilde{S}_{hv} & \widetilde{S}_{hh} \end{bmatrix} \qquad \textbf{(FSA)}. \tag{5.14}$$

As stated earlier, each component of $\widetilde{\mathbf{S}}$ is a function of the illumination and scattering angles. That is, for any polarization combination pq,

$$\begin{aligned} \widetilde{S}_{pq} &= \widetilde{S}_{pq}(\theta_i, \phi_i;\ \theta_s, \phi_s; \theta_j, \phi_j), \qquad p, q = \text{v or h}, \\ &= \lim_{R_r \to \infty} \left[R_r e^{-jkR_r} \left(\frac{E_p^s}{E_q^i} \right) \right], \end{aligned} \tag{5.15}$$

where (θ_j, ϕ_j) are the orientation angles of the object and the limit is used to denote that R_r is in the far-zone region of the scattering object.

5-3.2 BSA Convention

In the BSA convention, the transmitted and received fields are expressed in the form

$$\mathbf{E}^t = \hat{\mathbf{v}}_t E_v^t + \hat{\mathbf{h}}_t E_h^t, \tag{5.16a}$$

$$\mathbf{E}^r = \hat{\mathbf{v}}_r E_v^r + \hat{\mathbf{h}}_r E_h^r, \tag{5.16b}$$

with the unit vectors defined by Eq. (5.8). Upon comparing the expressions for the FSA and BSA local coordinate systems, the following becomes evident:

$$\mathbf{E}^i = \mathbf{E}^t, \tag{5.17}$$

$$\mathbf{E}^s = \begin{pmatrix} 1 & 0 \\ 0 & -1 \end{pmatrix} \mathbf{E}^r. \tag{5.18}$$

Therefore, the fields $\mathbf{E}^t$ and $\mathbf{E}^r$ are related by

$$\mathbf{E}^r = \frac{e^{-jkR_r}}{R_r} \mathbf{S}\, \mathbf{E}^t, \tag{5.19}$$

where

$$\mathbf{S} = \begin{pmatrix} S_{vv} & S_{vh} \\ S_{hv} & S_{hh} \end{pmatrix} \qquad \textbf{(BSA)} \tag{5.20}$$

is the scattering matrix of the object, defined according to the BSA convention. If we use Eqs. (5.17) and (5.18), we obtain the relationship

$$\widetilde{\mathbf{S}} = \begin{pmatrix} 1 & 0 \\ 0 & -1 \end{pmatrix} \mathbf{S}, \tag{5.21}$$

which implies that

$$\begin{aligned} \widetilde{S}_{vv} &= S_{vv}, \qquad \widetilde{S}_{hh} = -S_{hh}, \\ \widetilde{S}_{vh} &= S_{vh}, \qquad \widetilde{S}_{hv} = -S_{hv}. \end{aligned}$$

In general, $\widetilde{S}_{hv}$ and $\widetilde{S}_{vh}$ may not bear a simple relationship to one another, but in the backscatter direction ($\hat{\mathbf{k}}_s = -\hat{\mathbf{k}}_i$), the ***reciprocity theorem*** of electromagnetic scattering (Tsang et al., 1985) asserts that

$$\widetilde{S}_{vh} = -\widetilde{S}_{hv} \qquad \textbf{(backscatter)} \tag{5.22a}$$

and

$$S_{vh} = S_{hv} \qquad \textbf{(backscatter)}. \tag{5.22b}$$

5-3.3 Stokes Parameters and Mueller Matrix

The relationship given by Eq. (5.12) relates the h- and v-polarized components of the electric field $\mathbf{E}^s$ of the wave scattered by an object with scattering matrix $\widetilde{\mathbf{S}}$ to the polarized components of $\mathbf{E}^i$ of the incident wave illuminating the object. Often, the quantities of greater interest are the specific intensities of the incident and scattered waves. To that end, we introduce the ***vector specific intensity*** of an incident wave as

$$\mathbf{I}^i = \begin{bmatrix} I_v^i \\ I_h^i \\ U^i \\ V^i \end{bmatrix} = \begin{bmatrix} |E_v^i|^2 \\ |E_h^i|^2 \\ 2\Re\mathrm{e}(E_v^i E_h^{i*}) \\ 2\Im\mathrm{m}(E_v^i E_h^{i*}) \end{bmatrix} \Big/ \eta, \tag{5.23a}$$

where η is the intrinsic impedance of the medium. The elements of $\mathbf{I}_i$ are called the ***Stokes parameters***, of

which $I_{\mathrm{v}}^{\mathrm{i}}$ and $I_{\mathrm{h}}^{\mathrm{i}}$ represent the specific intensities of the v- and h-polarized components of $\mathbf{I}^{\mathrm{i}}$, and the last two terms, namely U^{i} and V^{i}, jointly account for the phase difference between $E_{\mathrm{v}}^{\mathrm{i}}$ and $E_{\mathrm{h}}^{\mathrm{i}}$.

A similar definition with superscript i replaced with superscript s applies to the vector specific intensity of the scattered wave:

$$\mathbf{I}^{\mathrm{s}} = \begin{bmatrix} I_{\mathrm{v}}^{\mathrm{s}} \\ I_{\mathrm{h}}^{\mathrm{s}} \\ U^{\mathrm{s}} \\ V^{\mathrm{s}} \end{bmatrix} = \begin{bmatrix} |E_{\mathrm{v}}^{\mathrm{s}}|^2 \\ |E_{\mathrm{h}}^{\mathrm{s}}|^2 \\ 2\Re\mathrm{e}(E_{\mathrm{v}}^{\mathrm{s}} E_{\mathrm{h}}^{\mathrm{s}*}) \\ 2\Im\mathrm{m}(E_{\mathrm{v}}^{\mathrm{s}} E_{\mathrm{h}}^{\mathrm{s}*}) \end{bmatrix} \Big/ \eta. \tag{5.23b}$$

By using Eq. (5.12) to evaluate the four quantities in Eq. (5.23b) and then relating their expressions to the four quantities defined in Eq. (5.23a) for the incident wave, we obtain the following relationship:

$$\mathbf{I}^{\mathrm{s}} = \frac{1}{R_{\mathrm{r}}^2} \widetilde{\mathbf{M}}\, \mathbf{I}^{\mathrm{i}} \qquad \textbf{(FSA)}, \tag{5.24a}$$

where R_{r} is the range between the scattering object and the location at which $\mathbf{I}^{\mathrm{s}}$ is measured. The 4×4 matrix $\widetilde{\mathbf{M}}$ is the ***modified Mueller matrix*** of the scattering object, defined in the forward scattering alignment (FSA) convention:

$$\widetilde{\mathbf{M}} = \begin{bmatrix} |\widetilde{S}_{\mathrm{vv}}|^2 & |\widetilde{S}_{\mathrm{vh}}|^2 & \cdots \\ |\widetilde{S}_{\mathrm{hv}}|^2 & |\widetilde{S}_{\mathrm{hh}}|^2 & \\ 2\Re\mathrm{e}(\widetilde{S}_{\mathrm{vv}}\widetilde{S}_{\mathrm{hv}}^*) & 2\Re\mathrm{e}(\widetilde{S}_{\mathrm{vh}}\widetilde{S}_{\mathrm{hh}}^*) & \\ 2\Im\mathrm{m}(\widetilde{S}_{\mathrm{vv}}\widetilde{S}_{\mathrm{hv}}^*) & 2\Im\mathrm{m}(\widetilde{S}_{\mathrm{vh}}\widetilde{S}_{\mathrm{hh}}^*) & \end{bmatrix}$$

$$\begin{bmatrix} \Re\mathrm{e}(\widetilde{S}_{\mathrm{vv}}\widetilde{S}_{\mathrm{vh}}^*) & -\Im\mathrm{m}(\widetilde{S}_{\mathrm{vv}}\widetilde{S}_{\mathrm{vh}}^*) \\ \Re\mathrm{e}(\widetilde{S}_{\mathrm{hv}}\widetilde{S}_{\mathrm{hh}}^*) & -\Im\mathrm{m}(\widetilde{S}_{\mathrm{hv}}\widetilde{S}_{\mathrm{hh}}^*) \\ \Re\mathrm{e}(\widetilde{S}_{\mathrm{vv}}\widetilde{S}_{\mathrm{hh}}^* + \widetilde{S}_{\mathrm{vh}}\widetilde{S}_{\mathrm{hv}}^*) & -\Im\mathrm{m}(\widetilde{S}_{\mathrm{vv}}\widetilde{S}_{\mathrm{hh}}^* - \widetilde{S}_{\mathrm{vh}}\widetilde{S}_{\mathrm{hv}}^*) \\ \Im\mathrm{m}(\widetilde{S}_{\mathrm{vv}}\widetilde{S}_{\mathrm{hh}}^* + \widetilde{S}_{\mathrm{vh}}\widetilde{S}_{\mathrm{hv}}^*) & \Re\mathrm{e}(\widetilde{S}_{\mathrm{vv}}\widetilde{S}_{\mathrm{hh}}^* - \widetilde{S}_{\mathrm{vh}}\widetilde{S}_{\mathrm{hv}}^*) \end{bmatrix}. \tag{5.24b}$$

The scattering amplitudes of the scattering object are defined for the specific combination of the six angles listed explicitly in Eq. (5.15).

The significance of the relationships given by Eq. (5.24) is that it is possible to construct a receiver that can measure all of the elements of the matrix $\widetilde{\mathbf{M}}$, without having to measure the phase angles of any of the scattering amplitudes directly. The Stokes vector–Mueller matrix formulation is at the heart of the radiative transfer models used in Chapters 6, 8, 9, and 12 to compute polarimetric scattering and emission by surfaces and volumes.

Before closing this section, we should note that in the backscatter alignment convention (BSA), the counterpart of Eq. (5.24) takes the form

$$\mathbf{I}^{\mathrm{r}} = \frac{1}{R_{\mathrm{r}}^2} \mathbf{M}\, \mathbf{I}^{\mathrm{t}} \qquad \textbf{(BSA)} \tag{5.25a}$$

with $\mathbf{I}^{\mathrm{t}} = \mathbf{I}^{\mathrm{i}}$,

$$\mathbf{I}^{\mathrm{r}} = \begin{bmatrix} I_{\mathrm{v}}^{\mathrm{r}} \\ I_{\mathrm{h}}^{\mathrm{r}} \\ U^{\mathrm{r}} \\ V^{\mathrm{r}} \end{bmatrix} = \begin{bmatrix} |E_{\mathrm{v}}^{\mathrm{r}}|^2 \\ |E_{\mathrm{h}}^{\mathrm{r}}|^2 \\ 2\Re\mathrm{e}(E_{\mathrm{v}}^{\mathrm{r}} E_{\mathrm{h}}^{\mathrm{r}*}) \\ 2\Im\mathrm{m}(E_{\mathrm{v}}^{\mathrm{r}} E_{\mathrm{h}}^{\mathrm{r}*}) \end{bmatrix} \Big/ \eta. \tag{5.25b}$$

and

$$\mathbf{M} = \begin{bmatrix} |S_{\mathrm{vv}}|^2 & |S_{\mathrm{vh}}|^2 & \cdots \\ |S_{\mathrm{hv}}|^2 & |S_{\mathrm{hh}}|^2 & \\ 2\Re\mathrm{e}(S_{\mathrm{vv}}S_{\mathrm{hv}}^*) & 2\Re\mathrm{e}(S_{\mathrm{vh}}S_{\mathrm{hh}}^*) & \\ 2\Im\mathrm{m}(S_{\mathrm{vv}}S_{\mathrm{hv}}^*) & 2\Im\mathrm{m}(S_{\mathrm{vh}}S_{\mathrm{hh}}^*) & \end{bmatrix}$$

$$\begin{bmatrix} \Re\mathrm{e}(S_{\mathrm{vv}}S_{\mathrm{vh}}^*) & -\Im\mathrm{m}(S_{\mathrm{vv}}S_{\mathrm{vh}}^*) \\ \Re\mathrm{e}(S_{\mathrm{hv}}S_{\mathrm{hh}}^*) & -\Im\mathrm{m}(S_{\mathrm{hv}}S_{\mathrm{hh}}^*) \\ \Re\mathrm{e}(S_{\mathrm{vv}}S_{\mathrm{hh}}^* + S_{\mathrm{vh}}S_{\mathrm{hv}}^*) & -\Im\mathrm{m}(S_{\mathrm{vv}}S_{\mathrm{hh}}^* - S_{\mathrm{vh}}S_{\mathrm{hv}}^*) \\ \Im\mathrm{m}(S_{\mathrm{vv}}S_{\mathrm{hh}}^* + S_{\mathrm{vh}}S_{\mathrm{hv}}^*) & \Re\mathrm{e}(S_{\mathrm{vv}}S_{\mathrm{hh}}^* - S_{\mathrm{vh}}S_{\mathrm{hv}}^*) \end{bmatrix}. \tag{5.25c}$$

Even though the forms of $\mathbf{I}^{\mathrm{r}}$ and $\mathbf{M}$ are the same as those of $\mathbf{I}^{\mathrm{s}}$ and $\widetilde{\mathbf{M}}$, respectively, $\mathbf{I}^{\mathrm{r}} \neq \mathbf{I}^{\mathrm{s}}$ and $\widetilde{\mathbf{M}} \neq \mathbf{M}$. In $\mathbf{I}^{\mathrm{r}}$, for example, $E_{\mathrm{h}}^{\mathrm{r}}$ is defined along $\hat{\mathbf{h}}_{\mathrm{r}}$ and in $\mathbf{I}^{\mathrm{s}}$, $E_{\mathrm{h}}^{\mathrm{s}}$ is defined along $\hat{\mathbf{h}}_{\mathrm{s}}$, but $\hat{\mathbf{h}}_{\mathrm{s}} = -\hat{\mathbf{h}}_{\mathrm{r}}$.

5-4 Radar Equation

Figure 5-7 depicts a bistatic radar system observing a target at a range R_{t} from the transmitter and a range R_{r} from the receiver. The radar transmitter injects power P_q^{t} into a q-polarized transmit antenna. At the receiver,

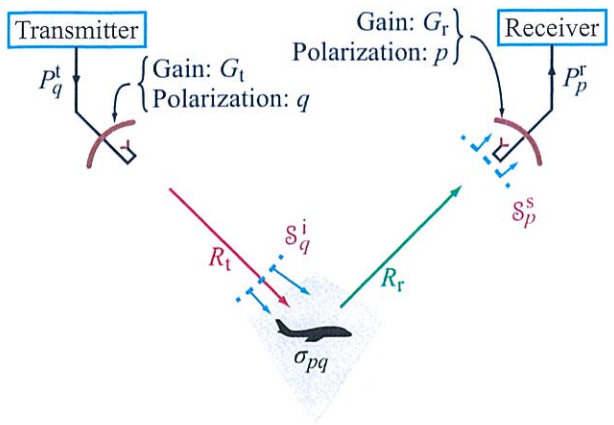

Figure 5-7: Power density $\mathcal{S}_q^i$ of the incident wave is defined at the location of the target, whereas $\mathcal{S}_p^s$ of the scattered energy is defined at the location of the receive antenna.

a p-polarized receive antenna delivers power P_p^r to the receiver.

▶ A pq-polarized radar (with p denoting the polarization of the receive antenna and q denoting the polarization of the transmit antenna, in that order) measures hh scattering by the target if $p = q = \text{h}$; it measures hv scattering if $p = \text{h}$ and $q = \text{v}$; and so on. ◀

At the target location, the power density illuminating the target is

$$\mathcal{S}_q^i = \frac{P_q^t}{4\pi R_t^2} G_t \qquad (\text{W/m}^2), \tag{5.26}$$

where $(P_q^t/4\pi R_t^2)$ represents the power density that would have been radiated had the antenna been isotropic, and G_t is the gain of the transmit antenna in the direction of the target. The power intercepted by the target is scattered (reradiated) along many directions, but our interest is in only the power radiated toward the receive antenna, and in only the component of that power with polarization state p, because that is the only component that will be captured by the p-polarized receive antenna. The p-polarized power reradiated by the target, denoted P_p^{rer}, is related to the power density $\mathcal{S}_q^i$ incident on the target by

$$P_p^{rer} = \sigma_{pq} \mathcal{S}_q^i, \tag{5.27a}$$

where σ_{pq} is the pq-polarized ***radar cross section*** (RCS) of the target for the specific combination of incident and scattered directions. Combining Eqs. (5.26) and (5.27a) gives

$$P_p^{rer} = \frac{P_q^t G_t}{4\pi R_t^2} \sigma_{pq} \qquad (\text{W}). \tag{5.27b}$$

The reradiated power spreads over a spherical surface, resulting in scattered power density $\mathcal{S}_p^s$ incident upon the receive antenna. At range R_r from the target

$$\mathcal{S}_p^s = \frac{P^{rer}}{4\pi R_r^2} = \frac{P_q^t G_t}{(4\pi R_t R_r)^2} \sigma_{pq} \qquad (\text{W/m}^2). \tag{5.28a}$$

With an effective area A_r and radiation efficiency ξ_r, the receive antenna intercepts and delivers (to the receiver) power P_p^r given by

$$P_p^r = \xi_r A_r \mathcal{S}_q^s = \frac{P_q^t G_t \xi_r A_r}{(4\pi R_t R_r)^2} \sigma_{pq}. \tag{5.28b}$$

By incorporating the relations $A_r = (\lambda^2/4\pi) D_r$ and $G_r = \xi_r D_r$ [Eqs. (3.24) and (3.31b)], we obtain the ***bistatic radar equation***

$$\frac{P_p^r}{P_q^t} = \frac{G_t G_r \lambda^2}{(4\pi)^3 R_t^2 R_r^2} \sigma_{pq} \qquad \textbf{(point-target bistatic radar equation)}. \tag{5.29a}$$

Under monostatic conditions, $R_t = R_r = R$, and if the radar uses the same antenna for both the transmit and receive functions (but with polarization q when transmitting and polarization p when receiving), Eq. (5.29a) simplifies to

$$\frac{P_p^r}{P_q^t} = \frac{G^2 \lambda^2}{(4\pi)^3 R^4} \sigma_{pq} \qquad \textbf{(point-target monostatic radar equation)}, \tag{5.29b}$$

where $G = G_t = G_r$.

Note that the range dependence in the radar equation varies as $1/R^4$, the product of two one-way propagation processes.

The expressions given by Eq. (5.29) pertain to a target whose physical dimensions are such that the solid angle it subtends (from where the radar is located) is much smaller than the solid angle of the radar beams [Fig. 5-4(b)]. We call such a target a ***point target***, even though it may have a complex geometry and a nonuniform scattering pattern. Its backscattering *strength* is defined by its RCS σ_{pq}, which has units of area. If we take the ratio of Eq. (5.28a) to Eq. (5.26), we obtain the result

$$\sigma_{pq} = \lim_{R_r \to \infty} \left(4\pi R_r^2 \frac{\mathcal{S}_p^s}{\mathcal{S}_q^i} \right), \tag{5.30}$$

where the limit has been added to emphasize the condition that the range R_r at which the scattered power density $\mathcal{S}_p^s$ is measured is in the far-zone region of the target. Power densities $\mathcal{S}_p^s$ and $\mathcal{S}_q^i$ are related to the electric fields of their respective waves by $\mathcal{S}_p^s = |E_p^s|^2/2\eta_0$ and $\mathcal{S}_q^i = |E_q^s|^2/2\eta_0$, where η_0 is the intrinsic impedance of air. In view of Eq. (5.15), σ_{pq} is related to the scattering amplitude S_{pq} by

$$\sigma_{pq} = 4\pi |\widetilde{S}_{pq}|^2. \tag{5.31}$$

Models for computing $\widetilde{S}_{pq}$, and by extension σ_{pq}, of simple point targets, such as spheres and cylinders, are available in Section 5-11. For complex targets, like ships and aircraft, highly sophisticated computer simulation techniques beyond the scope of this book are needed to compute σ_{pq}.

5-5 Scattering from Distributed Targets

The monostatic radar equation given by Eq. (5.29b) for a point target may be extended to the distributed target shown in Fig. 5-8 by integrating the backscattered power over the illuminated area A:

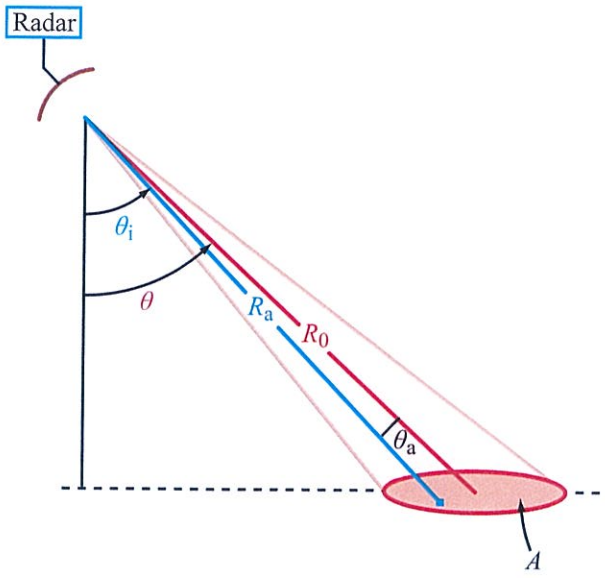

Figure 5-8: Illumination geometry for a distributed target.

$$P_p^r(\theta) = \iint_A \frac{P_q^t G^2(\theta_a, \phi_a) \lambda^2}{(4\pi)^3 R_a^4} \cdot \sigma_{pq}^0 \, dA \tag{5.32}$$

where θ is the ***incidence angle*** of the boresight direction of the antenna, relative to normal incidence, (θ_a, ϕ_a) define the direction relative to boresight of a point within A, and R_a is the range to it. The polarization indices p and q are included in the above expression to show the connection between the q-polarized transmitted power, the p-polarized received power, and the pq-polarized ***backscattering cross section per unit area*** σ_{pq}^0, which is defined as the backscattering cross section σ_{pq} of a distributed target of horizontal area A, normalized with respect to A,

$$\sigma_{pq}^0 = \sigma_{pq}/A. \tag{5.33a}$$

Often, σ^0 is referred to as the (differential) ***backscattering coefficient*** or ***radar reflectivity***.

As discussed later in Section 5-6, the power backscattered by a distributed target with *seemingly uniform* properties, such as a bare soil surface, exhibits large variations from one illuminated area to the next.

The reasons for these variations and the steps usually taken to reduce them are discussed in Sections 5-6 to 5-9. For the present, however, we should amend the definition of σ^0_{pq} given by Eq. (5.33a) to the more correct and formal definition

$$\sigma^0_{pq} = \frac{1}{A}\langle \sigma_{pq} \rangle, \tag{5.33b}$$

where $\langle\ \rangle$ denotes the ensemble-average operation over many measurements of σ_{pq}, corresponding to independent illuminated areas of the distributed target.

► That is, σ^0_{pq} is, by definition, the *average value* of the backscattering cross section of the distributed target, normalized to the illumination area of the antenna beam. ◄

Accordingly, the ensemble-average operation should apply to the left-hand side of Eq. (5.32). That is,

$$\langle P^{\mathrm{r}}_p(\theta) \rangle = \iint_A \frac{P^{\mathrm{t}}_q\, G^2(\theta_{\mathrm{a}}, \phi_{\mathrm{a}})\, \lambda^2}{(4\pi)^3 R^4_{\mathrm{a}}} \cdot \sigma^0_{pq}\, dA. \tag{5.34}$$

5-5.1 Narrow-Beam Scatterometer

If the distributed target has uniform properties across the area illuminated by the antenna beam, and if the beam is sufficiently narrow that $\sigma^0(\theta_{\mathrm{i}})$ at the local angle of incidence θ_{i} may be regarded as constant over the angular extent of the beam, then Eq. (5.34) may be simplified to

$$\langle P^{\mathrm{r}}_p(\theta) \rangle = \frac{P^{\mathrm{t}}_q \lambda^2}{(4\pi)^3}\, \sigma^0_{pq}(\theta) \iint_{A_{\mathrm{i}}} \frac{G^2(\theta_{\mathrm{a}}, \phi_{\mathrm{a}})\, dA}{R^4_{\mathrm{a}}}$$

$$= \frac{P^{\mathrm{t}}_q \lambda^2}{(4\pi)^3}\, \sigma^0_{pq}(\theta) \cdot I, \tag{5.35}$$

where

$$I = \iint_A \frac{G^2(\theta_{\mathrm{a}}, \phi_{\mathrm{a}})\, dA}{R^4_{\mathrm{a}}} \tag{5.36}$$

is called the ***illumination integral***. Often, an additional approximation is made, namely $R_{\mathrm{a}} \approx R_0$ over the solid angle of the antenna beam, in which case R_{a} can be taken outside the integral, and the antenna pattern is replaced with an equivalent pattern of gain G_0 and effective width β. These approximations lead to

$$I \approx \frac{G_0^2}{R_0^4} A$$

and

$$\langle P^{\mathrm{r}}_p(\theta) \rangle \approx \left[\frac{P^{\mathrm{t}}_q \lambda^2 G_0^2 A}{(4\pi)^3 R_0^4} \right] \cdot \sigma^0_{pq}(\theta), \tag{5.37}$$

(narrow-beam scatterometer)

where A is the area illuminated by the equivalent beam of the antenna. We should note that because the integration in Eq. (5.36) involves G^2, rather than just G, β is the effective beamwidth of the product pattern G^2. For a symmetrical Gaussian pattern $G(\theta_{\mathrm{a}})$, the effective beamwidth is approximately equal to its half-power (3 dB) beamwidth $\beta_{1/2}$. The half-power beamwidth of $G^2(\theta_{\mathrm{a}})$ is $\beta = \beta_{1/2}/\sqrt{2}$.

5-5.2 Imaging Radar

The assumptions made in deriving Eq. (5.37) are well suited to the imaging radar case because the dimensions of an illuminated ground cell are very small relative to the distance R between the radar and the cell. Figures 5-9 and 5-10 show the imaging geometries associated with real-aperture and synthetic-aperture radars when used in the side-looking mode. A real-aperture radar (Chapter 14) uses an antenna that is wide horizontally and narrow vertically. The horizontal beamwidth β_{h} is typically 1° or less, and the azimuth resolution is

$$r_{\mathrm{a}} = \beta_{\mathrm{h}} R \approx \frac{\lambda R}{l}, \tag{5.38}$$

where R is the slant range and l is the antenna length. Resolution in the range or across-track dimension is achieved by transmitting a narrow pulse of length τ.

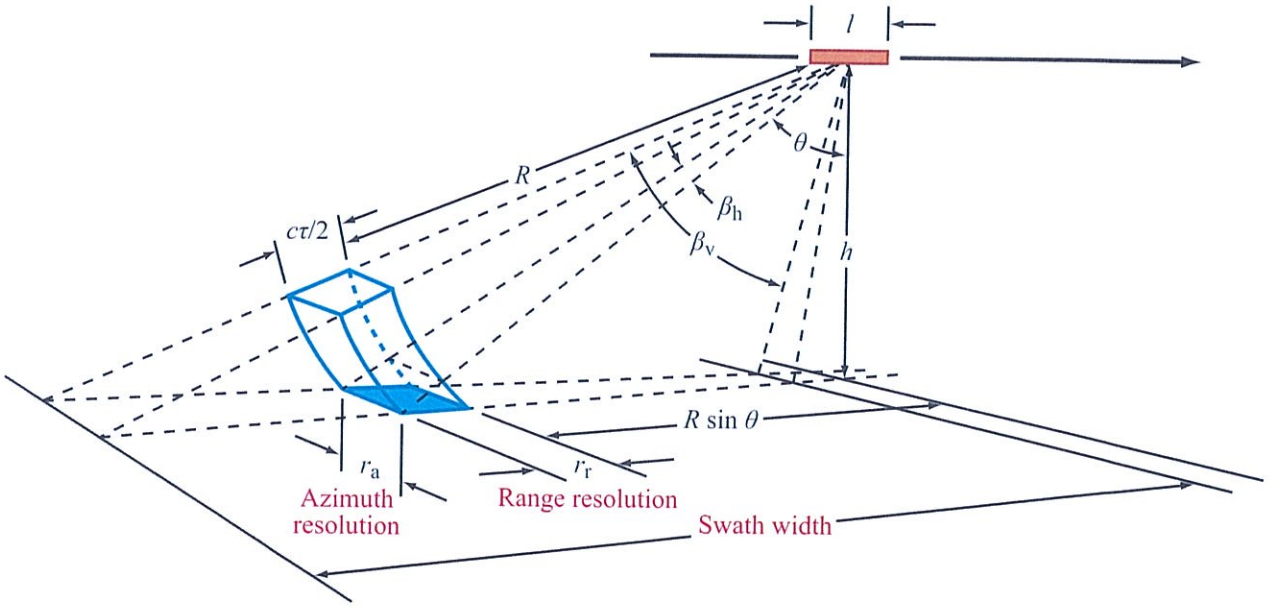

Figure 5-9: Real-aperture radar (RAR) geometry and resolved surface area.

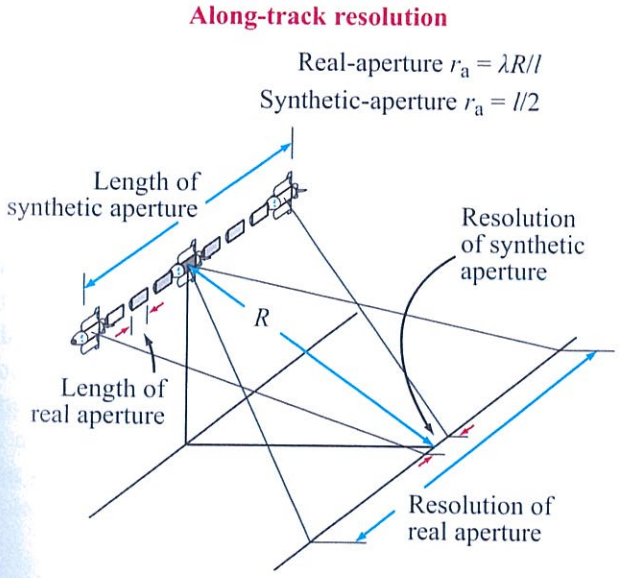

Figure 5-10: An illustration of how synthetic aperture works.

The image is produced by recording the returns from successive pulses as the aircraft moves past the area being covered. The ground-range resolution is independent of R and is given by

$$r_r = \frac{c\tau}{2\sin\theta}. \tag{5.39}$$

Inserting $A = r_a r_r$ in Eq. (5.37) leads to the following form of the radar equation for the real-aperture radar:

$$\langle P_p^r(\theta)\rangle = \left[\frac{P_q^t \lambda^3 G^2(\theta)\, c\tau}{2l(4\pi)^3 R^3 \sin\theta}\right] \cdot \sigma_{pq}^0(\theta), \tag{5.40}$$

(real-aperture radar)

where $G(\theta)$ is the antenna gain in the direction θ.

The antenna used in a synthetic-aperture radar (SAR) system is usually shorter in the along-track (azimuth) direction, but successive pulses are processed together to "focus" the azimuth beam of the antenna down to a very narrow beam corresponding to a very long synthetic

array (Chapter 14). Theoretically, the cell dimension in the along-track direction can be made independent of R and as small as

$$r_a = \frac{l}{2}, \tag{5.41}$$

where l is the along-track length of the antenna. When this is achieved, the SAR is said to be ***fully focused***. In the across-track direction, resolution is achieved in the same way as with the real-aperture radar, so Eq. (5.39) applies. For a fully focused SAR, the radar equation becomes

$$\langle P_p^r(\theta) \rangle = \left[\frac{P_q^t \lambda^2 G^2(\theta)\, lc\tau}{4(4\pi)^3 R^4 \sin\theta} \right] \cdot \sigma_{pq}^0(\theta). \tag{5.42}$$

(synthetic-aperture radar)

In summary, the power received due to backscatter from an illuminated cell that subtends a small solid angle as viewed from the radar is directly proportional to the backscattering coefficient σ^0, regardless of the specific type of radar used. Thus, the radar equations for the narrow-beam scatterometer, the real-aperture radar, and the synthetic-aperture radar can all be written in the compact form

$$\langle P_p^r(\theta) \rangle = K_{pq}\, \sigma_{pq}^0(\theta), \tag{5.43}$$

(transmit q / receive p polarization)

where K_{pq} may be regarded as a system constant representing the quantity in the square bracket in Eqs. (5.37), (5.40), or (5.42).

► In radar remote sensing, the differential scattering coefficient σ_{pq}^0 is the critical link between the radar as a sensing instrument and the intended application. ◄

By calibrating the radar to determine K_{pq}, the measured power can be used to determine the reflectivity σ_{pq}^0. Then, from models relating σ_{pq}^0 to the biophysical or geophysical properties of the terrain, we can generate estimates of those biophysical or geophysical properties. Often the process involves multiple measurements of σ_{pq}^0 corresponding to different combinations of polarizations and microwave frequencies.

5-5.3 Specific Intensities for Distributed Target

In Section 5-3.3, the vector specific intensity of the wave incident upon a point target, $\mathbf{I}^i$, and the vector specific intensity of the wave scattered by it, $\mathbf{I}^s$, are represented by Eqs. (5.23a) and (5.23b). The representations for $\mathbf{I}^i$ and $\mathbf{I}^s$ are identical in form, despite the fact that $\mathbf{I}^i$ is associated with a plane wave and $\mathbf{I}^s$ is associated with a spherical wave. The forms of $\mathbf{I}^i$ and $\mathbf{I}^s$ are identical because the target is treated as a point.

For a distributed target, the scattering coefficient is defined as the average scattering cross section per unit area for plane-wave incidence and spherical-wave scattering by the distributed target. Hence, Eq. (5.23a) continues to provide a valid representation of the vector specific intensity of the incident wave, but the representation for the vector specific intensity of the scattered wave needs to be defined in terms of the net electric field $\mathbf{E}^s$, representing the vector sum of all fields scattered from an illuminated area A subtending a solid angle $d\Omega_s$ given by

$$d\Omega_s = \frac{A\cos\theta_s}{R_r^2}, \tag{5.44}$$

where R_r is the range from the surface to the receiver and θ_s is the angle between the surface normal and the scattering direction [Fig. 5-5(a)]. Accordingly, $\mathbf{I}^i$ and $\mathbf{I}^s$ are defined as

$$\mathbf{I}^i = \begin{bmatrix} I_v^i \\ I_h^i \\ U^i \\ V^i \end{bmatrix} = \begin{bmatrix} |E_v^i|^2 \\ |E_h^i|^2 \\ 2\Re\mathrm{e}(E_v^i E_h^{i*}) \\ 2\Im\mathrm{m}(E_v^i E_h^{i*}) \end{bmatrix} \Big/ \eta, \tag{5.45a}$$

$$\mathbf{I}^s\, d\Omega_s = \begin{bmatrix} I_v^s \\ I_h^s \\ U^s \\ V^s \end{bmatrix} d\Omega_s = \begin{bmatrix} |E_v^s|^2 \\ |E_h^s|^2 \\ 2\Re\mathrm{e}(E_v^s E_h^{s*}) \\ 2\Im\mathrm{m}(E_v^s E_h^{s*}) \end{bmatrix} \Big/ \eta. \tag{5.45b}$$

Note the distinction between the Stokes parameters of $\mathbf{I}^{\mathrm{i}}$ and $\mathbf{I}^{\mathrm{s}}$. For the vertical-polarization Stokes parameters,

$$I_{\mathrm{v}}^{\mathrm{i}} = \frac{|E_{\mathrm{v}}^{\mathrm{i}}|^2}{\eta}, \tag{5.46a}$$

whereas

$$I_{\mathrm{v}}^{\mathrm{s}}\, d\Omega_{\mathrm{s}} = \frac{|E_{\mathrm{v}}^{\mathrm{s}}|^2}{\eta}. \tag{5.46b}$$

For the simple case where both the transmitting and receiving antennas are vertically polarized, the scattering coefficient is defined as

$$\begin{aligned}\sigma_{\mathrm{vv}}^0 &= \frac{4\pi R_{\mathrm{r}}^2}{A}\,\frac{\langle |E_{\mathrm{v}}^{\mathrm{s}}|^2\rangle}{|E_{\mathrm{v}}^{\mathrm{i}}|^2} \\ &= \frac{4\pi R_{\mathrm{r}}^2}{A}\,\frac{\langle I_{\mathrm{v}}^{\mathrm{s}}\rangle\, d\Omega_{\mathrm{s}}}{I_{\mathrm{v}}^{\mathrm{i}}} \\ &= \frac{4\pi R_{\mathrm{r}}^2}{A}\,\frac{\langle I_{\mathrm{v}}^{\mathrm{s}}\rangle}{I_{\mathrm{v}}^{\mathrm{i}}}\cdot\frac{A\cos\theta_{\mathrm{s}}}{R_{\mathrm{r}}^2} = 4\pi\cos\theta_{\mathrm{s}}\,\frac{\langle I_{\mathrm{v}}^{\mathrm{s}}\rangle}{I_{\mathrm{v}}^{\mathrm{i}}}.\end{aligned} \tag{5.47}$$

The modified definition of $\mathbf{I}^{\mathrm{s}}$ does not change the relationship between σ_{vv}^0 and the scattering amplitude S_{vv}. From Eq. (5.12),

$$E_{\mathrm{v}}^{\mathrm{s}} = \frac{e^{-ikR_{\mathrm{r}}}}{R_{\mathrm{r}}}\, S_{\mathrm{vv}} E_{\mathrm{v}}^{\mathrm{i}}, \tag{5.48}$$

which leads to

$$\sigma_{\mathrm{vv}}^0 = \frac{4\pi R_{\mathrm{r}}^2}{A}\,\frac{\langle |E_{\mathrm{v}}^{\mathrm{s}}|^2\rangle}{|E_{\mathrm{v}}^{\mathrm{i}}|^2} = \frac{4\pi}{A}\,\langle |S_{\mathrm{vv}}|^2\rangle. \tag{5.49}$$

If the radar is polarimetric, i.e., capable of measuring the scattering matrix $\widetilde{\mathbf{S}}$, not only can it determine σ_{pq}^0 for hh, hv, vv, and vh polarizations, but through the application of polarization synthesis (Section 5-10), it is also possible to synthesize images corresponding to the transmission and reception of any combination of polarizations, including circular and elliptical.

5-6 RCS Statistics

As noted earlier, the scattering amplitude S_{pq} of a target is dependent not only on the incident and scattered directions, but also on its shape and orientation. The question is: how sensitive is S_{pq}, or σ_{pq}, to the orientation of the target. Obviously, it depends on the shape of the target. For a sphere, its RCS is independent of its orientation, but that is not true for most targets. To illustrate with a real example, let us consider the pattern shown in Fig. 5-11. The pattern represents the backscatter cross section σ for a B-26 aircraft as a function of aspect angle. The data were obtained by mounting the aircraft on a turntable and then observing the backscattered signal measured by a 3 GHz radar as the turntable was rotated about its axis. The most striking feature of the scattering pattern is the strong sensitivity of σ to aspect angle; σ changes by an order of magnitude (10 dB) in response to a change of a fraction of a degree in aspect angle, and by two orders

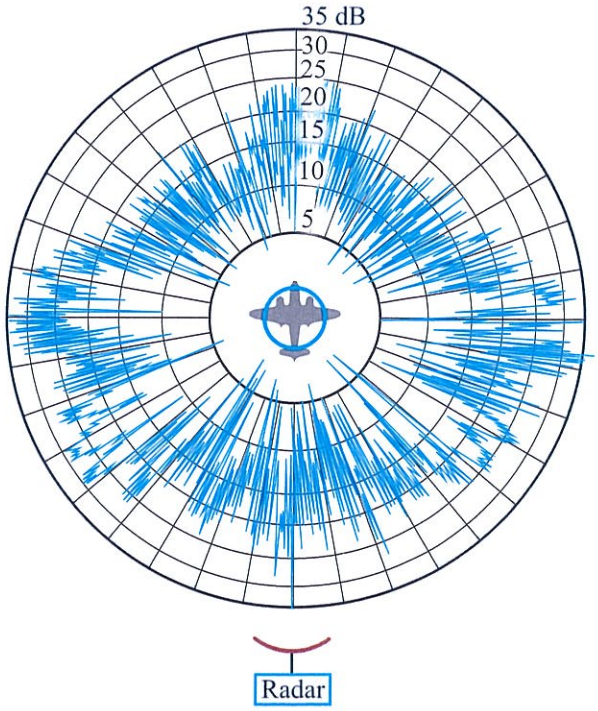

Figure 5-11: Measured azimuthal pattern of the radar backscatter from a B-26 airplane at 10 cm wavelength [from Ridenour, 1947, courtesy McGraw-Hill Book Company].

of magnitude (20 dB) in response to a change of a full degree. The full dynamic range exceeds 30 dB (1000 : 1)!

The aircraft consists of a number of scattering elements, each characterized by a scattering pattern that reflects its particular shape and orientation. The composite backscatter in a given direction is the phasor sum of the waves backscattered from the individual elements, which includes the propagation phase delay to and from each element. The peaks in the pattern shown in Fig. 5-11 are associated with constructive interference of the backscattered phasor and the nulls are associated with destructive interference.

Although an aircraft has a distinctly different geometry from that of a distributed terrain surface, the nature of the scattering process is fundamentally the same in both cases. The aircraft has a ***deterministic scattering pattern*** because it has a well-defined geometry, whereas a distributed target has a ***random scattering pattern*** (Fig. 5-12) because its scattering elements are randomly distributed. Both patterns exhibit large fluctuations. The pattern shown in Fig. 5-12(b) was generated from radar backscatter measurements made by a 35 GHz truck-mounted scatterometer as the truck was driven across an asphalt surface with the antenna beam pointing downward along the aft direction at an incidence angle of 40° relative to normal incidence [Fig. 5-12(a)]. The antennas were mounted atop a telescopic boom at a height of 10.3 m above the asphalt surface. The sampling rate was such that the footprints (on the asphalt surface) corresponding to adjacent samples were totally independent (no overlap). The vertical axis in Fig. 5-12(b) represents the ratio of the received power to the average value computed for all 1000 measurements, expressed in dB. The measured values extend over a range of 50.2 dB, or 10^5 : 1.

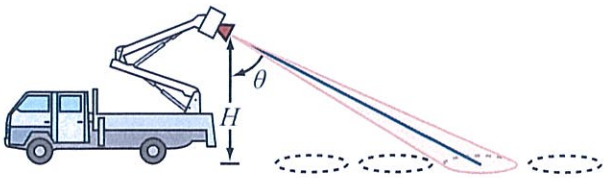

(a) Beam movement

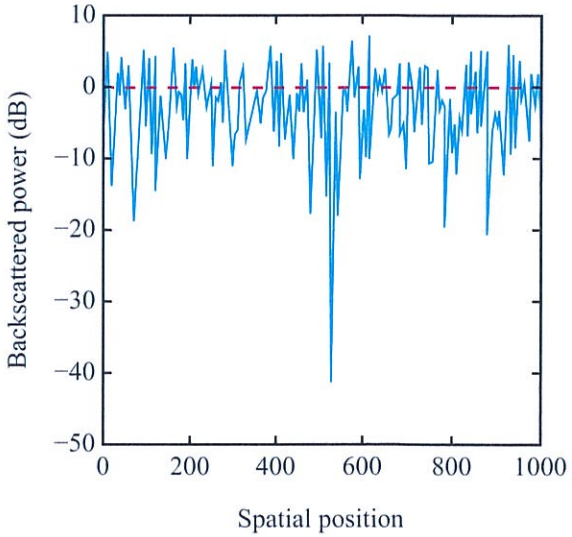

(b) Backscattering variation

Figure 5-12: The sketch in (a) shows how the measurements [shown in (b)] of the backscatter from an asphalt surface were acquired. The incidence angle was 40°, the frequency 35 GHz, the platform height 10.4 m, and the polarization vv [from Ulaby et al., 1988a].

► The implication of the results displayed in Fig. 5-12 is that the backscattered signal measured by a terrain-looking radar exhibits fluctuations from one spot to the next, "even when the terrain is the same." An image of a seemingly uniform bare soil field, for example, exhibits large pixel-to-pixel intensity variations, often referred to as ***image speckle*** (Fig. 5-13). To extract information from a radar image, it is necessary to understand the statistics of image speckle and how to reduce it. ◄

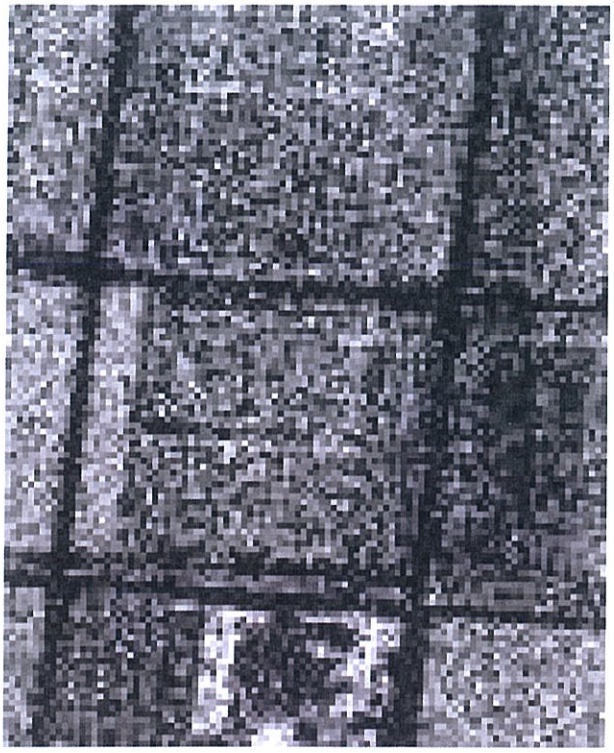

Figure 5-13: Image speckle refers to the pixel-to-pixel variation of image tone. This is a 1 m × 1 m resolution Ku-band SAR image of an agricultural area [Sandia National Lab].

5-7 Rayleigh Fading Model

The term ***radar clutter*** was introduced during World War II to denote unwanted radar echoes from extended targets such as rain, land, and water. When a downward-looking radar is used for the purpose of detecting or tracking a ***hard target***, such as a bridge or a vehicle, the terrain background represents a source of interference because the energy backscattered from the terrain *clutters* the fidelity of the desired signal. In the 1950s and 1960s, ***radar terrain clutter*** encompassed all aspects of scattering from terrain surfaces [Barton, 1975]. This included theoretical models for electromagnetic interaction with surfaces and volumes, experimental measurements of the backscattering cross section per unit area for various types of terrain, and the statistics associated with the scattering process. Research in this field was conducted primarily in support of military applications. The advent of high resolution imaging radar in the 1950s led to the development of ***radar remote sensing***, which evolved into a major scientific discipline with wide-ranging civilian, military, and environmental application. In many of these application, the terrain-scattered radar signal, which previously was regarded as a source of interference, is itself the information carrier because the information sought is derived from knowledge of how waves scatter from rough surfaces and inhomogeneous media. Because of this wider scope of the intended applications of radar scattering, in today's literature the generic term ***radar scattering from distributed targets*** has become the standard term used (instead of terrain clutter) to refer to the topics previously classified as radar clutter.

From the standpoint of detection and tracking applications, terrain scattering is viewed in statistical terms because the objective is to determine the degradation in the false alarm probability (associated

Random Variables

For any random variable x, defined over the range x_1 to x_2 and characterized by a probability density function (pdf) $p(x)$:

$$\bar{x} = \langle x \rangle = \int_{x_1}^{x_2} x\, p(x)\, dx = \text{mean value of } x$$

$$\overline{x^2} = \langle x^2 \rangle = \int_{x_1}^{x_2} x^2\, p(x)\, dx = \text{second moment of } x$$

$$s_x^2 = \langle x^2 \rangle - \langle x \rangle^2 = \text{variance of } x$$

$$s_x = \text{standard deviation of } x$$

$$\beta_x = \left(\frac{s_x}{\bar{x}}\right)^2 = \text{normalized variance of } x$$

$$P(x \le x') = \int_{x_1}^{x'} p(x)\, dx$$

$$= \text{cumulative distribution of } x \le x'$$

with detecting a target) caused by interference of the radar return from the target with that contributed by the terrain background. Consequently, the term radar clutter has evolved into the more specific term ***radar clutter statistics*** and is used in today's literature to denote the ***probability density function*** (*pdf*) associated with a statistical scattering process whose mean value is σ^0, the backscattering cross section per unit area. As we shall see later, σ^0 of terrain varies as a function of two sets of parameters: (1) the sensor parameters, namely the wavelength (or frequency), the incidence angle (defined here with respect to normal incidence), and the polarization configurations of the transmitting and receiving antennas, and (2) the terrain parameters, which include its dielectric properties and geometrical characteristics. Hence, in general the pdf is both sensor- and terrain type-specific. Actually, the pdf is also terrain condition-specific because a forest, for example, undergoes changes in both its dielectric properties and geometry as a function of time.

A distributed target usually consists of a large number of randomly distributed scatterers. When a distributed target is illuminated by a coherent electromagnetic wave, the magnitude of the backscattered signal is equal to the phasor sum of the returns from all of the scatterers illuminated by the incident beam. The backscattered signal is a random variable because the dielectric and geometrical properties of a terrain surface are random variables.

► Two ground patches with the same statistical properties may produce backscattered signals with different magnitudes because the individual scatterers in the two patches have different locational arrangements. This variability in the magnitude of the backscattered signal is referred to as ***signal fading*** or ***signal scintillation***. ◄

To characterize the fluctuation statistics associated with a terrain surface of uniform electromagnetic properties, the usual approach is to model the surface as an ensemble of independent, randomly located scatterers, all of comparable scattering strengths. Such a model leads to the result that the amplitude of the backscattered signal is ***Rayleigh-distributed***. If the return is dominated by backscatter from one or a few strong scatterers, the fading process is characterized by the ***Rice distribution*** (Raemer, 1997). Some experimental observations support the Rayleigh behavior (Bush and Ulaby, 1975; Ulaby et al., 1986b; Weinstock, 1965) whereas others, particularly those measured for complex terrain categories, are in closer agreement with the ***log-normal distribution***, the ***Weibull distribution*** (Kashihara et al., 1984; Schleher, 1976; Valenzuela and Laing, 1972), or other more complicated distributions (Jao, 1984). In this chapter we limit our treatment to the Rayleigh clutter model.

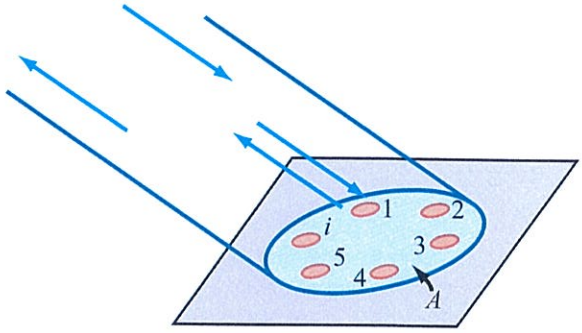

Figure 5-14: The illuminated area A contains N_s randomly distributed scatterers.

5-7.1 Underlying Assumptions

The Rayleigh clutter model used for radar scattering from an area-extended (distributed) target is essentially the same as the model used for random noise and is based on the same mathematical assumptions. A review of these assumptions will prove useful in later sections.

The sketch shown in Fig. 5-14 depicts a radar beam illuminating an area A of an area-extended target. The illuminated area contains N_s point scatterers, designated by the index $i = 1, 2, \ldots, N_s$. For simplicity, we shall confine our present discussion to the backscatter case. The electric field at the input of the receiving antenna due to backscatter by the ith scatterer may be expressed as

$$E_i(t) = K_i E_{i0} \cos(\omega t - 2kR_i + \theta_i), \qquad (5.50)$$

where E_{i0} is the scattering magnitude and θ_i is the scattering phase of the ith scatterer, R_i is the range from the antenna to the scatterer, $k = 2\pi/\lambda$ is the wavenumber, and K_i is a system constant that accounts for several radar system factors including propagation losses to and from the scatterer and antenna gain in the direction of the scatterer. The phasor-domain counterpart of Eq. (5.50) is

$$\mathbf{E}_i = K_i E_{i0} e^{j\phi_i}, \tag{5.51}$$

where ϕ_i, the phase angle of $\mathbf{E}_i$, is

$$\phi_i = \theta_i - 2kR_i. \tag{5.52}$$

Assumption 1: The scatterers are statistically independent. This assumption allows us to express the total instantaneous field due to the N_s scatterers contained in the area A as a simple sum,

$$\mathbf{E} = \sum_{i=1}^{N_s} K_i E_{i0} e^{j\phi_i}, \tag{5.53}$$

and it implies that interaction effects between adjacent scatterers may be ignored.

Assumption 2: The maximum range extent of the target $\Delta R = |R_i - R_j|_{\max}$ is much smaller than the mean range to the target area A, and the antenna gain is uniform across A. This allows us to set $K_i = K$ for all i. For convenience, we shall set $K = 1$. Hence,

$$\mathbf{E} = \sum_{i=1}^{N_s} E_{i0} e^{j\phi_i}. \tag{5.54}$$

The total field $\mathbf{E}$ is a vector sum of N_s phasors. If we express these phasors graphically (Fig. 5-15), with the first one starting at the origin and the successive ones each starting at the tip of the preceding one, the result is a vector from the origin to the tip of the last phasor. The length of this vector (which is called the ***voltage envelope***) and its phase angle are denoted E_e and ϕ, respectively. Thus,

$$\mathbf{E} = E_e e^{j\phi} = \sum_{i=1}^{N_s} E_{i0} e^{j\phi_i}. \tag{5.55}$$

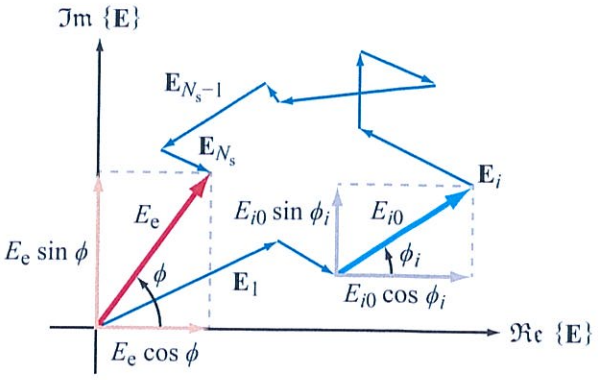

Figure 5-15: The vector $\mathbf{E} = E_e e^{j\phi}$ is the phasor sum of N_s fields.

Phasor $E_e e^{j\phi}$ has Cartesian components E_x and E_y (Fig. 5-15) given by

$$E_x = E_e \cos\phi = \sum_{i=1}^{N_s} E_{i0} \cos\phi_i, \tag{5.56a}$$

$$E_y = E_e \sin\phi = \sum_{i=1}^{N_s} E_{i0} \sin\phi_i. \tag{5.56b}$$

Assumption 3: N_s is a large number, which allows us to use the central-limit theorem, thereby treating E_x and E_y as normally distributed random variables with means

$$\overline{E}_x = \langle E_x \rangle = \sum_{i=1}^{N_s} \langle E_{i0} \cos\phi_i \rangle, \tag{5.57a}$$

$$\overline{E}_y = \langle E_y \rangle = \sum_{i=1}^{N_s} \langle E_{i0} \sin\phi_i \rangle. \tag{5.57b}$$

Through computer simulation, it can be demonstrated that N_s need not be exceedingly large to satisfy the central-limit theorem; in practice, N_s as small as 10 is sufficient (approximately).

Assumption 4: The scattering amplitude E_{i0} and phase ϕ_i are independent random variables. This condition is easily satisfied if E_{i0} is independent of the range R_i (and hence of the phase ϕ_i given by Eq. (5.52)),

which would be the case if the scatterers are randomly distributed in range because ϕ_i is dependent on the range R_i (through Eq. (5.52)), whereas E_{i0} is not.

Assumption 5: The phase ϕ_i is uniformly distributed over the range $[0, 2\pi]$. To satisfy this condition, it is not only necessary that the scatterers be randomly distributed in range, but the maximum range extent of the target ΔR must also be several wavelengths across.

Assumption 6: No one individual scatterer produces an electric field of magnitude commensurate with the resultant field from all other scatterers. In other words, the field **E** is not dominated by one (or a few) very strong scatterer(s). If this condition is not satisfied, the Rayleigh noise-like statistics do not apply and the statistics developed by Rice (Raemer, 1997) for one or more large signals contained in a background of noise should be used instead.

Based on Assumptions 3–6, Eq. (5.57a) becomes

$$\begin{aligned}\overline{E}_x &= \sum_{i=1}^{N_s} \langle E_{i0} \rangle \langle \cos \phi_i \rangle \\ &= \sum_{i=1}^{N_s} \langle E_{i0} \rangle \left[\frac{1}{2\pi} \int_0^{2\pi} \cos \phi_i \, d\phi_i \right] = 0, \end{aligned} \tag{5.58}$$

because the average value of $\cos \phi_i$ is zero. Similarly, $\overline{E}_y = 0$. Additionally, the mean value of the product $E_x E_y$ is

$$\langle E_x E_y \rangle = \sum_{i=1}^{N_s} \sum_{i=1}^{N_s} \langle E_{i0}^2 \rangle \left[\frac{1}{2\pi} \int_0^{2\pi} \cos \phi_i \sin \phi_i \, d\phi_i \right] = 0, \tag{5.59}$$

which implies that E_x and E_y are uncorrelated. For normally distributed random variables, this also implies statistical independence. Hence, their joint ***probability density function*** (pdf) is equal to the product of their individual pdfs, and also recalling that E_x and E_y have zero means, the joint pdf becomes

$$\begin{aligned} p(E_x, E_y) &= \frac{1}{\sqrt{2\pi}\, s} e^{-E_x^2/2s^2} \cdot \frac{1}{\sqrt{2\pi}\, s} e^{-E_y^2/2s^2} \\ &= \frac{1}{2\pi s^2} e^{-(E_x^2 + E_y^2)/2s^2}, \end{aligned} \tag{5.60}$$

(Gaussian pdf)

where s is the ***standard deviation*** of E_x and E_y. Our true interest is in E_e, the envelope of the total electric field, so we convert the pdf given by Eq. (5.60) into a pdf in the polar variables E_e and ϕ through the transformation

$$p(E_x, E_y)\, dE_x\, dE_y = p(E_e, \phi)\, dE_e\, d\phi. \tag{5.61}$$

Noting that

$$E_e^2 = E_x^2 + E_y^2 \tag{5.62}$$

and equating a differential area in (E_e, ϕ) space with its equivalent in (E_x, E_y) space, namely

$$E_e\, dE_e\, d\phi = dE_x\, dE_y, \tag{5.63}$$

we obtain the pdf

$$\begin{aligned} p(E_e, \phi) &= \frac{E_e}{2\pi s^2} e^{-E_e^2/2s^2}, \\ 0 \le E_e \le \infty \quad &\text{and} \quad 0 \le \phi \le 2\pi. \end{aligned} \tag{5.64}$$

The phase angle ϕ is uniformly distributed over $[0, 2\pi]$. Hence, the pdf for E_e alone is

$$\begin{aligned} p(E_e) &= \int_0^{2\pi} p(E_e, \phi)\, d\phi \\ &= \frac{E_e}{s^2} e^{-E_e^2/2s^2}, \qquad 0 \le E_e \le \infty. \end{aligned} \tag{5.65}$$

(Rayleigh pdf)

The pdf given by Eq. (5.65) is known as the ***Rayleigh distribution***.

The mean value of E_e is

$$\begin{aligned} \overline{E}_e &= \int_0^{\infty} E_e\, p(E_e)\, dE_e \\ &= \int_0^{\infty} \frac{E_e^2}{s^2} e^{-E_e^2/2s^2}\, dE_e = \sqrt{\frac{\pi}{2}}\, s. \end{aligned} \tag{5.66}$$

The variable E_e represents the magnitude of the cumulative electric field at the receiving antenna prior to detection by the receiver. Most receivers use either linear detection or square-law detection to convert the input signal to an output voltage. As we see in the following subsections, the output voltage of the linear receiver also

is characterized by a Rayleigh pdf, but that of the square-law receiver is characterized by an exponential pdf. Both cases, however, belong to the Rayleigh clutter model because the underlying pdf, $p(E_e)$, is Rayleigh.

► The terms ***Rayleigh fading*** and ***Rayleigh clutter*** refer to the model and the assumptions leading to Eq. (5.65) and should not be confused with the form of the pdf of the detected voltage. ◄

Between the input to the radar receiver, represented by the signal E_e (due to backscatter from a given pixel on the ground), and the final product in the form of a radar image, the signal undergoes two basic transformations, namely detection and image formation. Most radar receivers use either:

(a) Linear detection: the tone (digital value) of the processed image is directly proportional to E_e, in which case the image is called a voltage or ***amplitude image***. In the present treatment the image tone is represented by the symbol V.

(b) Square-law detection: the image tone is proportional to $|E_e|^2$, which is equivalent to power. The image is called an ***intensity image*** and its tone is represented by the symbol I.

The two detection options are discussed in the next two subsections.

5-7.2 Linear Detection

If the radar receiver uses a linear detector, its output voltage V is directly proportional to E_e; that is,

$$V = K_1 E_e = K_1 \overline{E}_e \frac{E_e}{\overline{E}_e} = K_1 \overline{E}_e f, \tag{5.67}$$

where K_1 is a system constant and f is a ***normalized fading random variable for voltage*** given by

$$f = \frac{E_e}{\overline{E}_e}. \tag{5.68}$$

The mean value of f is

$$\overline{f} = \frac{\overline{E}_e}{\overline{E}_e} = 1. \tag{5.69}$$

The mean field $\overline{E}_e$ is related to σ^0, the mean value of the backscattering cross section per unit area of the distributed target, by

$$\overline{E}_e = K_2 (\sigma^0)^{1/2}, \tag{5.70}$$

where K_2 is another system constant. Use of Eq. (5.70) in Eq. (5.67) gives

$$V = K_1 K_2 (\sigma^0)^{1/2} f. \tag{5.71}$$

In view of Eq. (5.69), the mean value of the linearly detected voltage measured by the radar is

$$\overline{V} = K_1 K_2 (\sigma^0)^{1/2} \overline{f} = K_1 K_2 (\sigma^0)^{1/2}, \tag{5.72}$$

where the averaging process is performed by adding many independent observations of the distributed target. For an imaging radar, this can be realized by adding together the voltages corresponding to many pixels. The value of constant $K_1 K_2$ can be established through calibration, thereby providing a direct mechanism for relating $\overline{V}$ to σ^0.

► Because the output voltage V is a product of its mean value $\overline{V} = K_1 K_2 (\sigma^0)^{1/2}$ and the random variable f, the process is sometimes referred to as a ***multiplicative noise model.*** ◄

From Eqs. (5.71) and (5.72), it follows that

$$f = \frac{V}{\overline{V}}. \tag{5.73}$$

The two relevant quantities are σ^0 and f; σ^0 represents the "strength" of the average backscatter from the distributed target and f accounts for variations among different observations (or image pixels).

The fading random variable f is linearly related to E_e through Eq. (5.68). Using the expression for $p(E_e)$ given by Eq. (5.65), in combination with the area relation

$$p(f)\, df = p(E_e)\, dE_e, \tag{5.74}$$

leads to the pdf

$$p(f) = \frac{\pi f}{2} \exp\left(-\frac{\pi}{4} f^2\right), \qquad f \geq 0. \tag{5.75}$$

(Rayleigh pdf)

The mean values of f and f^2 are

$$\overline{f} = 1, \tag{5.76a}$$

$$\overline{f^2} = \frac{4}{\pi}, \tag{5.76b}$$

and the corresponding standard deviation s_f is

$$s_f = [\overline{f^2} - \overline{f}^2]^{1/2} = \left(\frac{4}{\pi} - 1\right)^{1/2} = 0.523. \tag{5.76c}$$

The associated ***cumulative distribution*** $P(f \le f')$, where f' is some threshold level of interest, is

$$P(f \le f') = \int_0^{f'} p(f)\, df = 1 - \exp\left(-\frac{\pi}{4} f'^2\right), \qquad f' \ge 0. \tag{5.76d}$$

From Eq. (5.73) and the area relation $p(V)\, dV = p(f)\, df$, it is easy to show that the pdf $p(V)$ of the linearly detected voltage is

$$p(V) = \frac{\pi V}{2\overline{V}^2} \exp\left[-\frac{\pi}{4\overline{V}^2} V^2\right], \qquad V \ge 0. \tag{5.77a}$$

The mean value $\overline{V}$ is related to the reflectivity σ^0 by Eq. (5.72), and the ***standard-deviation-to-mean ratio*** is

$$\frac{s_V}{\overline{V}} = 0.523. \tag{5.77b}$$

5-7.3 Square-Law Detection

The voltage output of a square-law detector is directly proportional to the power of the input signal, rather than to its electric intensity E_e. Hence, within a proportionality constant, the output, represented by the symbol I (for intensity), is

$$I = K_3 E_e^2 = K_3 \overline{E_e^2} \frac{E_e^2}{\overline{E_e^2}} = K_3 K_4 \sigma^0 F, \tag{5.78}$$

where

$$F = \frac{E_e^2}{\overline{E_e^2}} = \frac{I}{\overline{I}} \tag{5.79}$$

is the ***normalized fading random variable for power***. Ignoring the constant $K_3 K_4$ and using the area relation $p(E_e)\, dE_e = p(I)\, dI = p(F)\, dF$ leads to the exponential pdf:

$$p(I) = \frac{1}{\overline{I}} e^{-I/\overline{I}}, \qquad p(F) = e^{-F}, \tag{5.80a}$$

(exponential pdf)

with

$$\overline{I} = \sigma^0, \qquad \overline{F} = 1, \tag{5.80b}$$

$$\frac{s_I}{\overline{I}} = 1, \qquad s_F = 1, \tag{5.80c}$$

and

$$P(I \le I') = 1 - e^{-I'/\overline{I}}, \qquad P(F \le F') = 1 - e^{-F'}. \tag{5.80d}$$

Note that for the exponential distribution, the ***standard-deviation-to-mean ratio*** is $s_I/\overline{I} = s_F/\overline{F} = 1$.

5-7.4 Interpretation

What do these statistics tell us? To answer this question, we start by examining Fig. 5-16(a), which shows plots of $p(f)$ and $p(F)$ for the Rayleigh and exponential distributions, respectively, and Fig. 5-16(b), which shows the corresponding cumulative distributions. We observe that the range of fading associated with the distributions is very large. That is, if we take a single sample of the signal from a Rayleigh-distributed or exponentially distributed ensemble, we have very little chance of selecting a value close to the mean. Let us illustrate this with a specific example. According to the Rayleigh distribution in Fig. 5-16(b), the value of f exceeded 5 percent of the time is 1.95 (relative to the mean) and that exceeded 95 percent of the time is 0.25. In decibels, these levels correspond to +5.8 dB and −11.9 dB, respectively. If we select a sample at random, the probability is 90 percent (95 to 5 range) that its value will be within the range extending from 11.9 dB below the true mean to 5.8 dB above the true mean. We may think of this as the ***90 percent confidence interval***

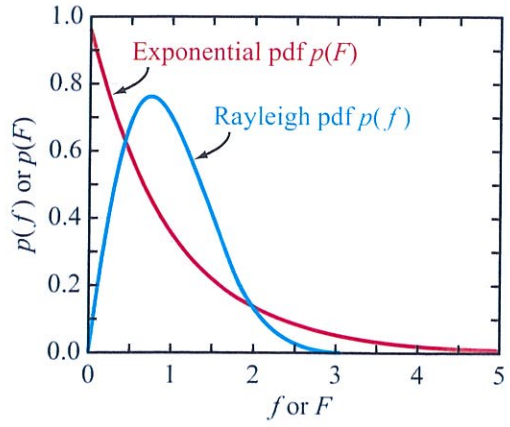

(a) Rayleigh and exponential pdfs

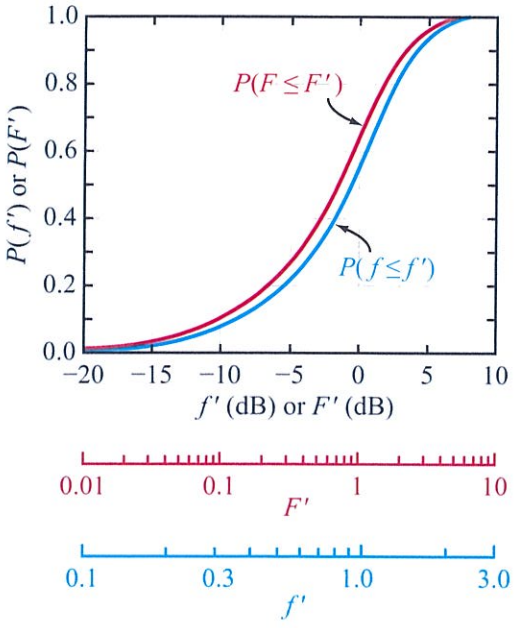

(b) Cumulative distributions

Figure 5-16: Plot of (a) probability density functions and (b) cumulative distributions for f and F.

associated with our measurement. The important point to note here is the fact that this interval (17.7 dB) is very large!

The situation is not much different when square-law detection is used: the 5 percent and 95 percent levels of the cumulative distribution for the exponential pdf are +4.8 and −12.9 dB, also totaling 17.7 dB. For the data presented earlier in Fig. 5-12, the data points that fall within the −12.9 dB to +4.8 dB range constitute 90.8 percent of the total, which is in close agreement with the 90 percent figure predicted by the exponential distribution. Furthermore, the measured pdf of F, shown in Fig. 5-17, exhibits a good fit to the exponential distribution.

5-8 Multiple Independent Samples

To reduce the uncertainty of a radar measurement of the backscatter from a terrain surface, it is necessary to average many independent samples together. Independence requires that the distribution of scatterers be statistically different between one observation and another. If a radar transmits multiple pulses, and then records the returns from the same target with identical scatterers at identical locations, the returns will not be independent. In fact, the backscattered signal is the same for all pulses. The noise generated by the receiver is likely to be random in time, so averaging multiple pulse returns improves the signal-to-noise ratio, but the returns are not statistically independent.

An easy way to increase the number of independent samples N contained in an estimate of the radar backscatter is through spatial averaging, which amounts to *trading spatial resolution for improved radiometric resolution*. The image generated by replacing N pixels with a new pixel bearing their average value is called an ***N-look image***.

5-8.1 N-Look Amplitude Image

If N randomly selected samples of a Rayleigh-distributed voltage V are averaged together, the average value V_N has the following properties:

$$V_N = \frac{1}{N}\sum_{i=1}^{N} V_i = K_1 K_2 (\sigma^0)^{1/2} \left[\frac{1}{N}\sum_{i=1}^{N} f_i\right]$$
$$= K_1 K_2 (\sigma^0)^{1/2} f_N, \qquad (5.81)$$

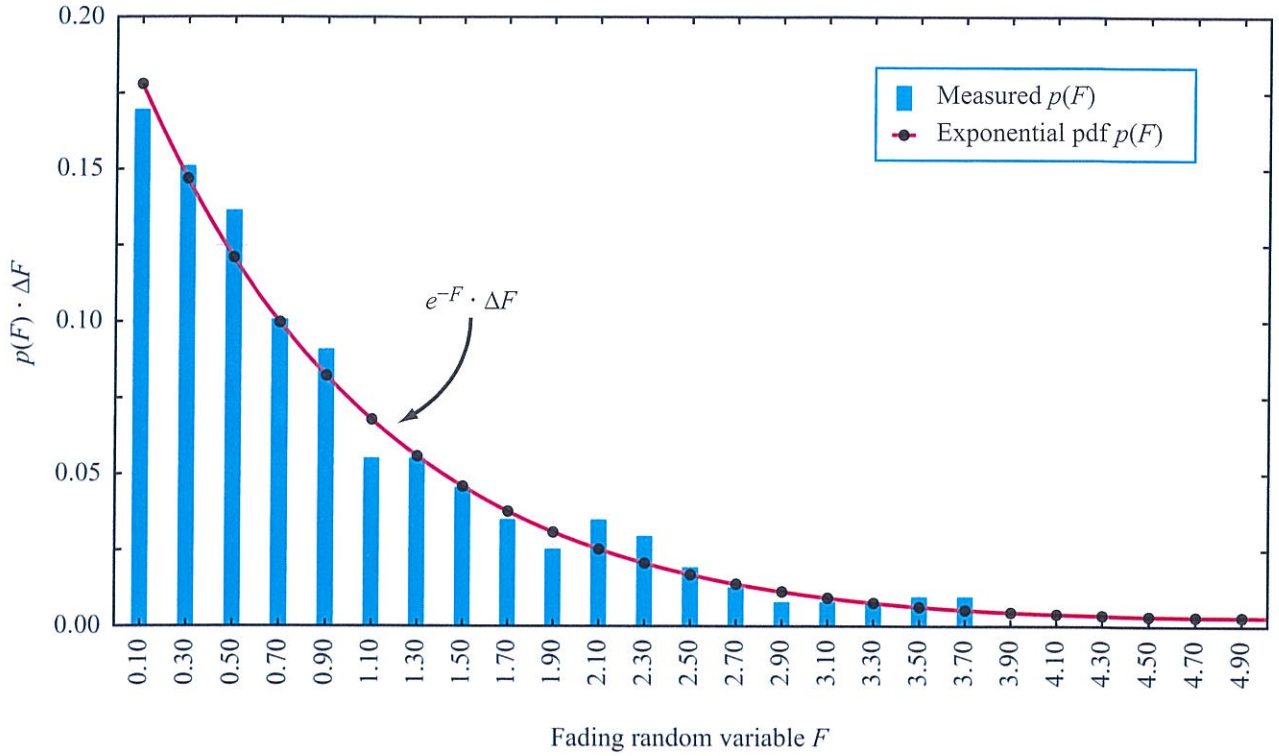

Figure 5-17: The measured pdf of the backscatter from asphalt [corresponding to the data in Fig. 5-12(b)] is found to be in good agreement with the exponential pdf based on the Rayleigh fading model.

where we define

$$f_N = \frac{1}{N}\sum_{i=1}^{N} f_i \tag{5.82}$$

as the fading random variable corresponding to the average of N independent samples. Its properties are

$$\overline{f}_N = 1, \tag{5.83a}$$

$$s_{f_N} = \frac{0.523}{\sqrt{N}}, \tag{5.83b}$$

and its pdf may be obtained by N-successive convolutions of the Rayleigh pdf given by Eq. (5.75). Plots of $p(f_N)$ are shown in Fig. 5-18(a) for several values of N. As expected, as N increases, the distribution becomes more peaked and narrow (the standard deviation decreases as $N^{-1/2}$) and eventually approaches the Gaussian pdf.

5-8.2 N-Look Intensity Image

If the receiver uses square-law detection, the average received power due to N independent samples is

$$I_N = K_3 K_4 \sigma^0 F_N \tag{5.84}$$

with

$$F_N = \frac{I_N}{\overline{I}_N} = \frac{1}{N}\sum_{i=1}^{N} F_i.$$

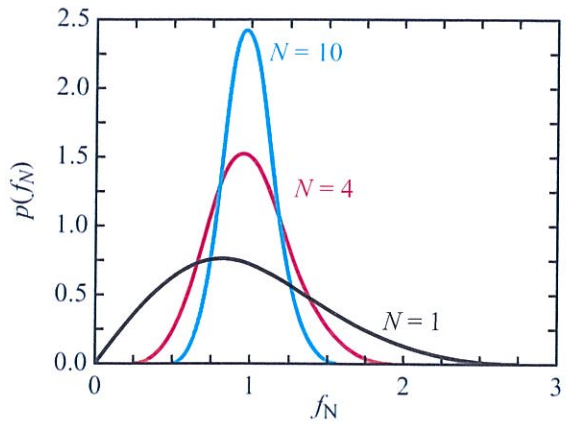

(a) pdf of f_N

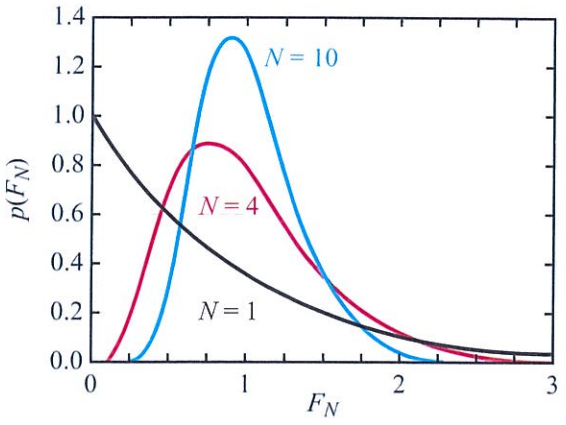

(b) pdf of F_N

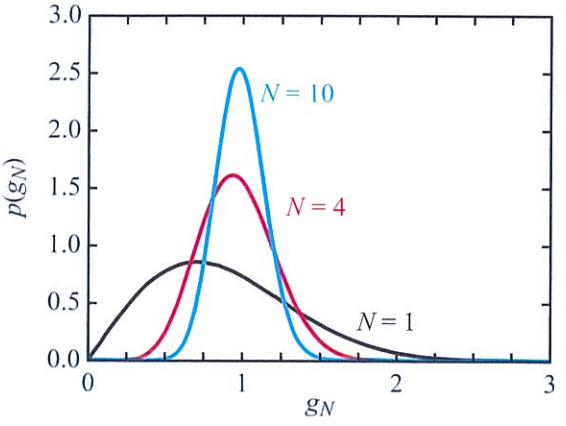

(c) pdf of g_N

Figure 5-18: Probability density function for $N = 1, 4,$ and 10 for (a) f_N (linear deduction), (b) F_N (square-law detection), and (c) g_N (square-root intensity).

Because the averaging process is linear, $\bar{I} = \bar{I}_N$. The statistical attributes of F_N are:

$$\overline{F}_N = 1, \qquad \overline{F_N^2} = 1 + \frac{1}{N}, \tag{5.85a}$$

$$s_{F_N} = \left[\overline{F_N^2} - \overline{F}_N^2\right]^{1/2} = \frac{1}{\sqrt{N}}, \tag{5.85b}$$

and its pdf is a ***χ^2 distribution with $2N$ degrees of freedom***:

$$p(F_N) = \frac{F_N^{N-1} N^N e^{-NF_N}}{(N-1)!}, \qquad F_N \geq 0. \tag{5.86}$$

The corresponding pdf for I_N is

$$p(I_N) = \frac{p(F_N)}{\bar{I}_N}. \tag{5.87}$$

Plots of $p(F_N)$ are shown in Fig. 5-18(b) for various values of N, and Fig. 5-19 shows plots of the 5% and 95% levels versus N. The 5% level is a plot of F_N' and represents the value of F_N' exceeded only 5% of the time; i.e., $P(F_N \geq F_N') = 0.05$. A similar definition applies to the 95% level.

5-8.3 *N*-Look Square-Root Intensity Image

In some radar systems, square-law detection is followed by (a) averaging N image pixels together and then (b) performing a square-root operation to compress the dynamic range. The tone (digital value) T of the resultant image is related to I by

$$T_N = \left[\frac{1}{N}\sum_{i=1}^{N} I_i\right]^{1/2}$$

$$= [I_N]^{1/2} = \left[\bar{I}_N \frac{I_N}{\bar{I}_N}\right]^{1/2} = \bar{I}_N^{1/2} F_N^{1/2} = \bar{T}_N g_N, \tag{5.88}$$

where g_N is the fading random variable for the N-look square-root intensity image,

$$g_N = F_N^{1/2}. \tag{5.89}$$

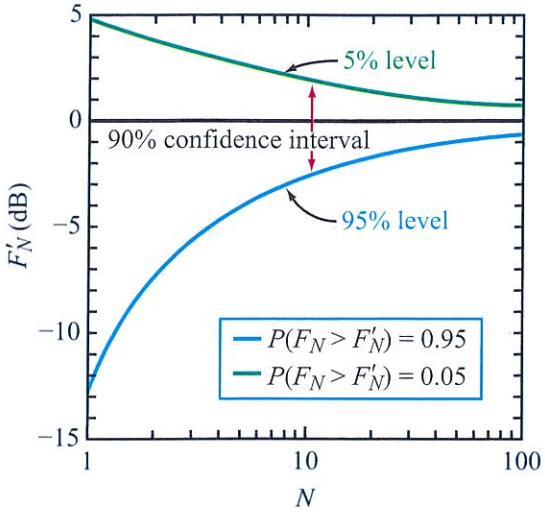

Figure 5-19: Plots of the 5% and 95% cumulative distribution levels versus N. The vertical spacing between these two curves is a measure of the "confidence interval" associated with a measurement of the radar backscatter.

The pdf of F_N is given by Eq. (5.86), so to obtain the pdf of g_N we use the density relation

$$p(g_N)\, dg_N = p(F_N)\, dF_N,$$

which leads to

$$p(g_N) = \frac{2g_N^{2N-1} N^N e^{-Ng_N^2}}{(N-1)!}, \qquad g_N \geq 0. \tag{5.90}$$

The mean values of g_N and its variance are given by

$$\bar{g}_N = \frac{\Gamma(N+1/2)}{N^{1/2}\,\Gamma(N)}, \tag{5.91a}$$

$$s_{g_N}^2 = 1 - \bar{g}_N^2, \tag{5.91b}$$

where $\Gamma(\ )$ is the Gamma function:

$$\Gamma(z) = \int_0^\infty t^{z-1} e^{-t}\, dt. \tag{5.92}$$

As $N \to \infty$, $\bar{g}_N \to 1$.

If a random variable x has a mean value $\bar{x}$ and a standard deviation s_x, and if a second random variable y is related to x by a smooth function $y = h(x)$, then the mean $\bar{y}$ and the standard deviation s_y of y may be related to $\bar{x}$ and s_x by the following approximate relations (Papoulis, 1965; pp. 151–152):

$$\bar{y} \approx y(x) + y''(x)\,\frac{s_x^2}{2}, \tag{5.93a}$$

$$s_y^2 \approx [y'(x)]^2 s_x^2, \tag{5.93b}$$

where $y' = dy/dx$ and all quantities are evaluated at $x = \bar{x}$. The application of these relations to $g_N = F_N^{1/2}$, evaluated at $F_N = \bar{F}_N = 1$, leads to

$$\bar{g}_N \approx 1 - \frac{1}{8N}, \tag{5.94a}$$

$$s_{g_N} \approx \frac{1}{2\sqrt{N}}. \tag{5.94b}$$

The relative error between the exact and approximate values of $\bar{g}_N$ and s_{g_N} is less than 1% if $N \geq 4$. Figure 5-18(c) displays plots of $p(g_N)$ as a function of g_N for $N = 1$, 4, and 10. The plots for the square-root intensity image are very similar to those for the amplitude image [Fig. 5-18(a)]. The similarity is also evident in the plots shown in Fig. 5-20, which depict the variation of the standard-deviation-to-mean ratio as a function of N for the three types of images. In all cases, significant improvement is realized by increasing N from 1 to 4 looks, followed by a more moderate rate of improvement as N is increased further.

5-8.4 Spatial Resolution vs. Radiometric Resolution

Part (a) of Fig. 5-21 depicts a synthesized single-look ($N = 1$) amplitude radar image with each pixel corresponding to a ground resolution of 1 m × 1 m. The image terrain consists of 3 square parcels of land, one covered with trees, another with grass, and the third with bare soil. Each parcel is imaged into $16 \times 16 = 256$ pixels.

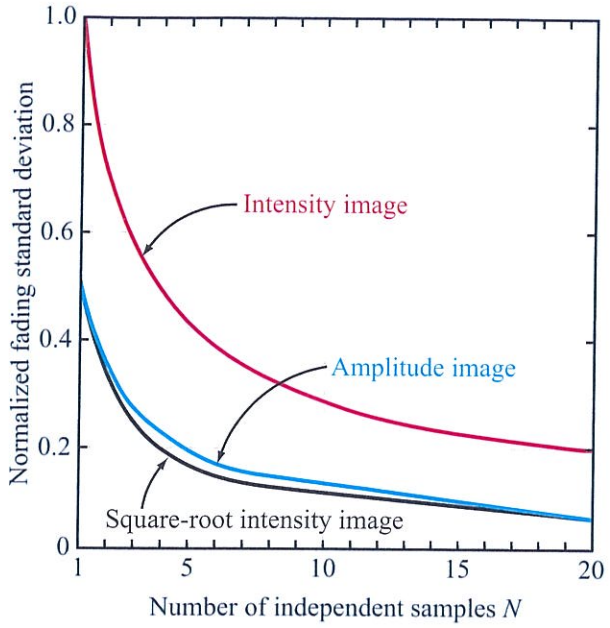

Figure 5-20: Variation of $s_{f_N}/\overline{f}_N$ (amplitude image), $s_{F_N}/\overline{F}_N$ (intensity image), and $s_{g_N}/\overline{g}_N$ (square-root intensity image) as a function of the number of looks (independent samples) N.

By averaging neighboring pixels together in groups of 4, we obtain the image in Fig. 5-21(b), which contains only $8 \times 8 = 64$ pixels with each pixel representing the backscatter from a 2 m $\times$ 2 m cell. The associated number of looks is $N = 4$. Upon repeating the process once again, we obtain the 16-look image in Fig. 5-21(c).

> ► Fundamentally, increasing N is equivalent to trading off spatial resolution for improved radiometric resolution. ◄

This statement is true when discrete measurements (corresponding to discrete resolution cells) are averaged together after detection, as well as when the averaging process is an integral part of the detection process. When generating a SAR image, steps may be taken during the image formation process to reduce image speckle. The fading or speckle pattern of the resultant image can be reduced by processing N separate segments of the total SAR bandwidth and then averaging these separate ***looks*** together. The process, which is referred to as ***mixed-integration*** or ***multiple-looking***, produces images with $N \geq 1$. This gain in the magnitude of N, however, is achieved at the expense of spatial resolution because the range resolution of the SAR image is inversely proportional to the bandwidth.

For illustration purposes, let us assume that the hypothetical image represented by Fig. 5-21 is an amplitude image with $K_1K_2 = 1$ [in Eq. (5.72)] and that the average backscatter values for the trees, grass, and soil parcels are 36, 16, and 4 m^2/m^2, respectively. For an amplitude image, the standard-deviation-to-mean ratio is given by

$$\frac{s}{\sqrt{\sigma^0}} = \frac{0.523}{\sqrt{N}},$$

where for an amplitude image, $\overline{V} = \sqrt{\sigma^0}$. Hence, for $N = 1$, the range for trees corresponding to ± 1 standard deviation (relative to the mean) extends from

$$\overline{V}_t - s_t = (1 - 0.523)\sqrt{\sigma_t^0} = 0.477 \times \sqrt{36} \approx 2.9 \text{ m}^2/\text{m}^2$$

to

$$\overline{V}_t + s_t = (1 + 0.523)\sqrt{\sigma_t^0} = 1.523 \times \sqrt{36} \approx 9.1 \text{ m}^2/\text{m}^2.$$

This range, along with corresponding ranges for grass and soil, is shown in Fig. 5-22(a). Because of the large overlap among the three ranges, if we do not know the identities of the pixels and we were to pick one at random and try to determine its identity (trees, grass, or soil) on the basis of its amplitude, the probability that we would classify it correctly is very low.

The potential for correct classification improves as we consider Fig. 5-22(b), representing an image with $N = 4$, because less overlap exists among the three vertical ranges. And for the 16-look image, there is no overlap between the three ranges, so classification accuracy should be much higher. We should note, however, that even with $N = 16$ looks, some of the pixels may be misclassified because the criterion we used is based on the ± 1 standard deviation range, which captures a significant part of the pdf, but not all of it.

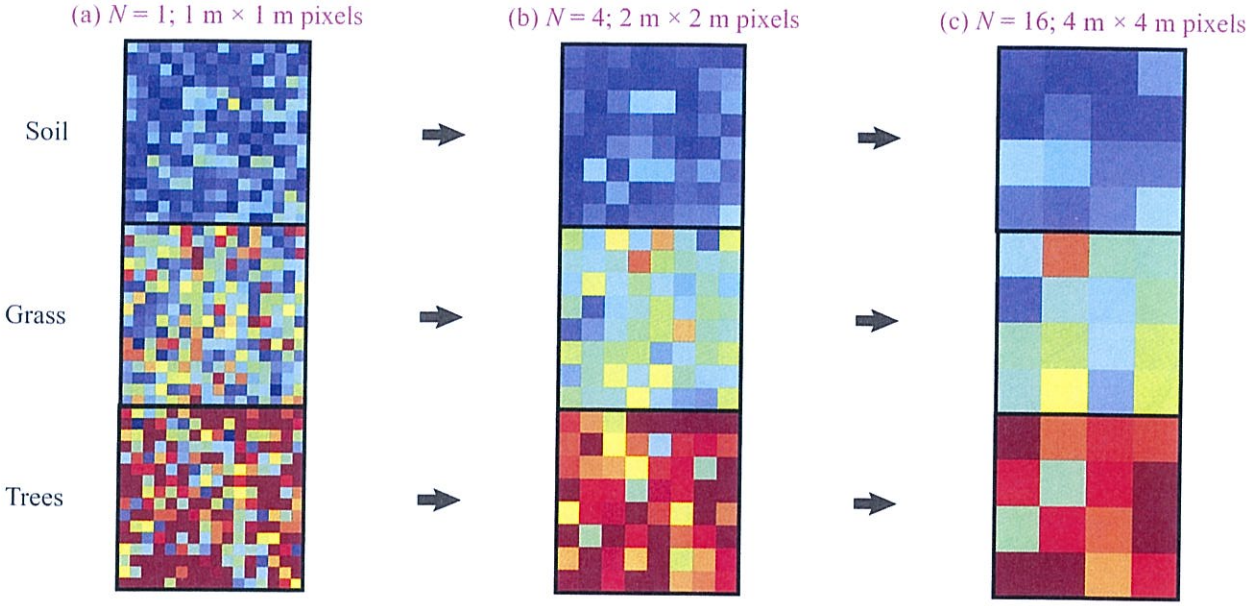

Figure 5-21: Simulated amplitude images of three distributed targets: trees with $\sigma_t^0 = 36\ m^2/m^2$, grass with $\sigma_g^0 = 16\ m^2/m^2$, and soil with $\sigma_s^0 = 4\ m^2/m^2$. Averaging multiple pixels trades off spatial resolution for improved radiometric resolution (less pixel-to-pixel variation).

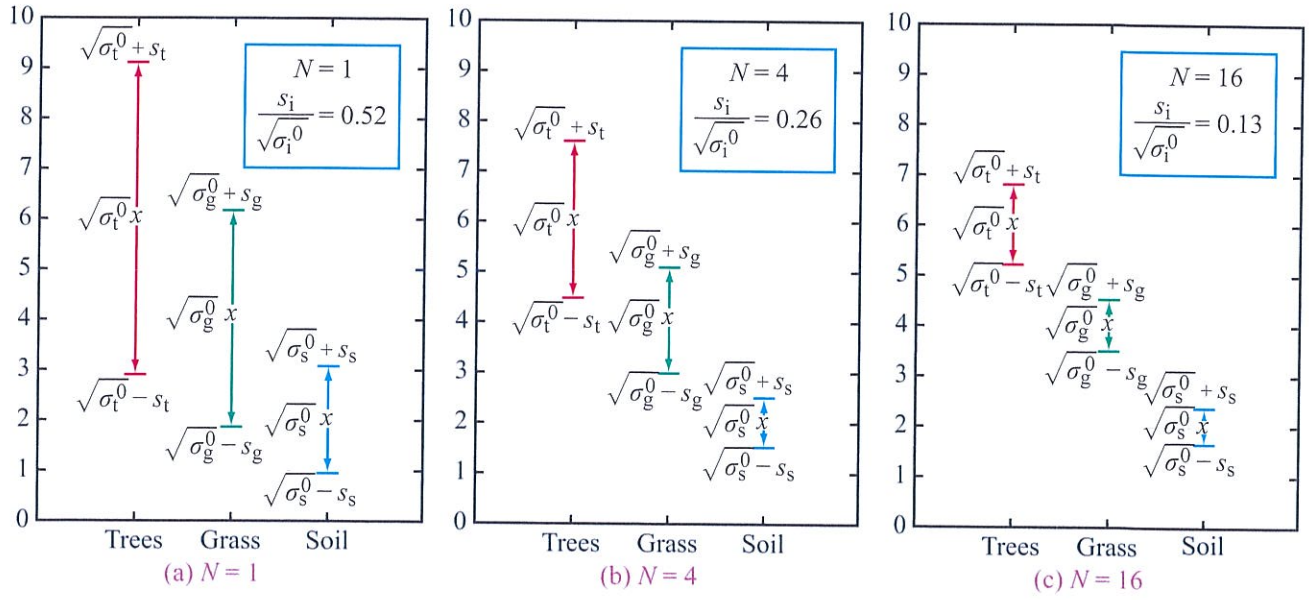

Figure 5-22: As the number of independent samples N is increased from 1 to 16, the confidence intervals around the means decrease by $1/\sqrt{N}$.

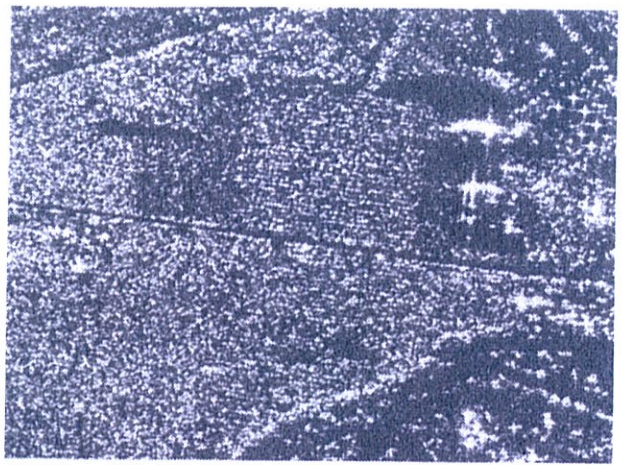

(a) 6 m × 6 m, $N = 1$

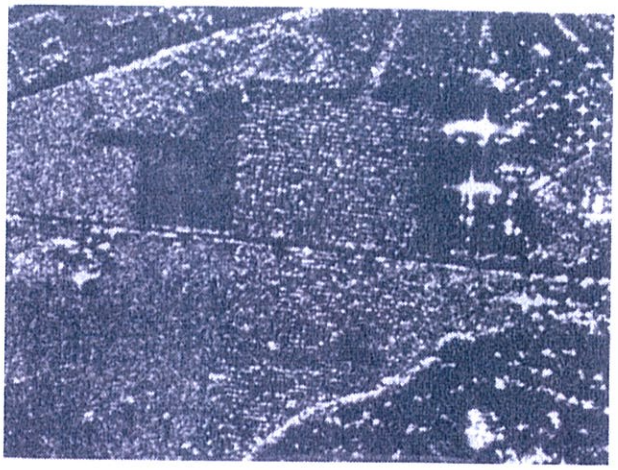

(b) 6 m × 6 m, $N = 4$

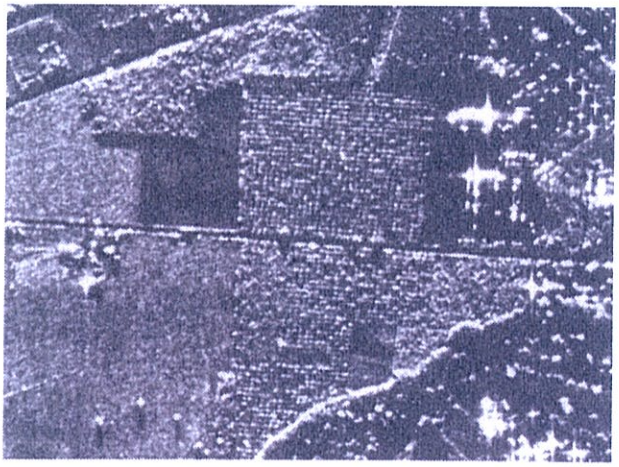

(c) 6 m × 6 m, $N = 12$

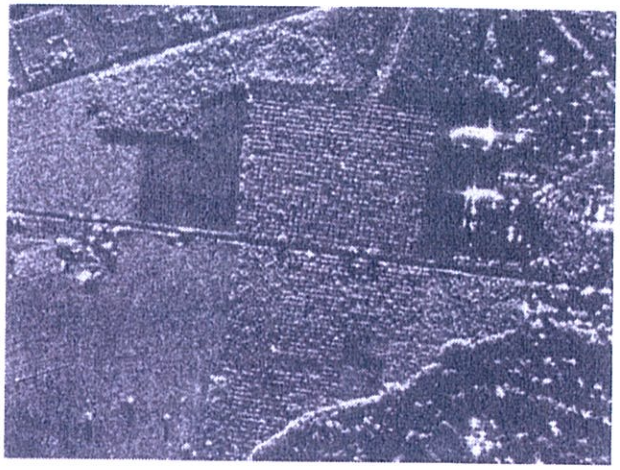

(d) 1.5 m × 2.1 m, $N = 1$

Figure 5-23: The four-image set provides a visual illustration of the relationships between image speckle, number of looks N, spatial resolution, and interpretability.

The image shown in Fig. 5-23(d), which is a fully focused SAR image with $N = 1$, has an image resolution capability corresponding to a ground resolution area approximately 1.5 m×2.1 m. From the raw data of this image, three other images were generated, all having the same ground resolution of 6 m×6 m. The image in Fig. 5-23(a) was generated by subsampling the raw data in both the azimuth and range dimensions to degrade the resolution to 6 m×6 m. Hence, no subsequent averaging was employed and N remained equal to 1. Partial and maximum possible averaging (or multilooking) was used in the generation of the images in parts (b) and (c) of Fig. 5-23 such that the spatial resolution was maintained at 6 m × 6 m.

The relationship between image speckle and the magnitude of N is quite *visible* in Fig. 5-23(a)–(c).

Despite the fact that the spatial resolution is the same for all three images, some features that are clearly distinguishable in Fig. 5-23(c) are totally indistinguishable in Fig. 5-23(a). An equally significant observation can be surmised from a comparison of the 6 m×6 m image with $N = 12$ [Fig. 5-23(c)] with the 1.5 m×2.1 m image with $N = 1$ [Fig. 5-23(d)].

► From an *interpretability* point of view, the two images offer comparable *resolving power* despite the fact that the area of the resolution cell of the high-resolution image is 12 times smaller than that of the other image. Thus, the resolution quality of an image is governed by both the spatial resolution of the ground cell represented by an image pixel and the number of independent samples (looks) N "contained" in the measurement of the power backscattered from the ground cell. ◄

5-8.5 Applicability of the Rayleigh Fading Model

Does the Rayleigh fading model provide an appropriate approach to characterize the statistics of radar backscatter from terrain? The answer is a qualified yes. If the assumptions underlying the Rayleigh fading model are reasonably satisfied, the available experimental evidence suggests that the Rayleigh model is quite applicable (Bush and Ulaby, 1975; Ulaby et al., 1986b; Ulaby et al., 1988a). Terrain targets satisfying the Rayleigh assumption include bare ground surfaces, agricultural fields, dense forest canopies, and snow-covered ground. In all cases the target must have stationary statistics, which requires that its "local-average" electromagnetic properties be uniform across the extent of the target.

Rayleigh fading is inapplicable for a sparse forest observed by a high-resolution radar because the high spatial variations in tree density at the scale of the radar resolution violate the stationarity assumption. Thus, a very important parameter governing applicability of Rayleigh statistics to backscatter from terrain is the size of the radar resolution cell relative to the spatial frequency spectrum characterizing the scattering from the terrain target under consideration.

► An urban scene is another target class or condition for which Rayleigh statistics may not apply. ◄

If the resolution cell size is such that the backscatter is likely to be dominated by the return from one or a few strong scatterers, such as a building or a corner reflector formed by two intersecting flat surfaces, the Rayleigh clutter model is no longer applicable.

These observations are borne out by the histograms shown in Fig. 5-24, which were generated from 4-look Seasat SAR data for image segments containing water, forest, and urban scenes. The image was generated by a square-root intensity process. The continuous curves are plots of the pdf $p(T_4)$ given by

$$p(T_4) = \frac{1}{\bar{I}^{1/2}}\, p(g_4),$$

where $p(g_4)$ is the pdf of the speckle random variable given by Eq. (5.90). We observe that the histogram for water is in reasonably close agreement with the theoretical pdf based on Rayleigh fading, the histogram for the forest category exhibits some departure from the theoretical pdf, and the histogram of the urban scene is markedly different from the theoretical pdf. These differences are attributable to the *textural variations* of the image, which are not accounted for in the theoretical model.

5-9 Image Texture and Despeckle Filtering

5-9.1 Image Texture

A radar image of a distributed target that obeys Rayleigh fading statistics is said to be ***textureless***; the image exhibits the usual pixel-to-pixel tonal variations characteristic of speckle, but it has no other spatial patterns.

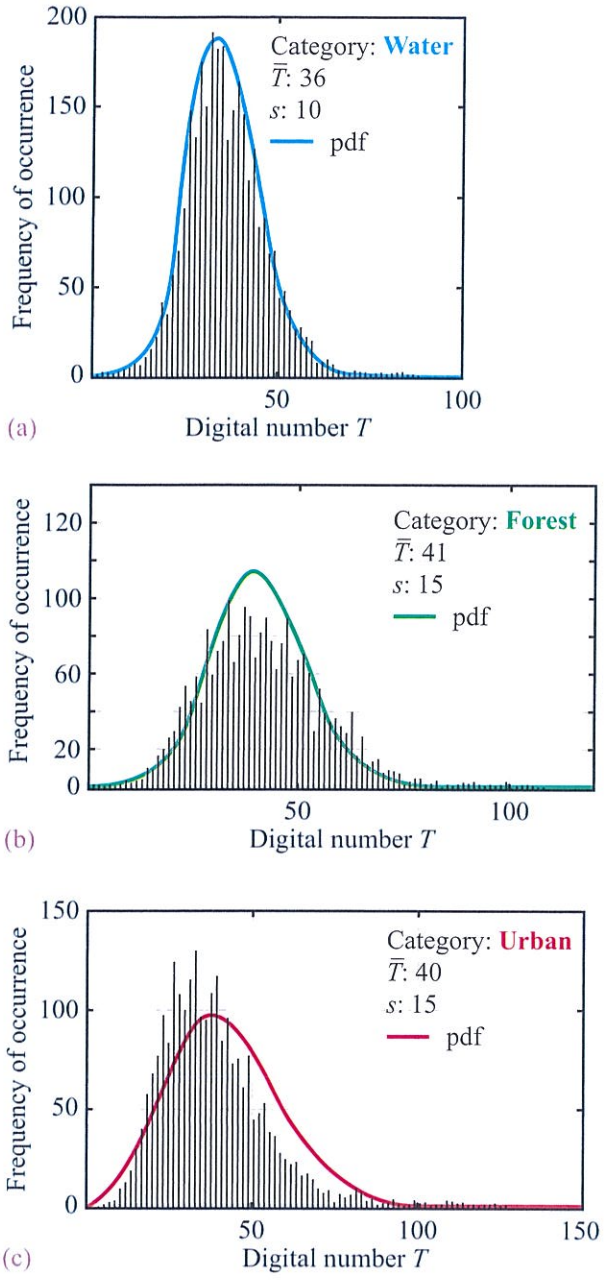

Figure 5-24: Histograms of image tone T (digital number) of square-root-intensity Seasat SAR images of three categories of distributed targets. The water category provides a good fit to the theoretical pdf given by Eq. (5.90); the forest category exhibits a significant departure due to textural variations and the urban category exhibits the greatest departure from theory. Urban scenes often have bright, dominant scatterers, which violates Assumption 6 of the Rayleigh model.

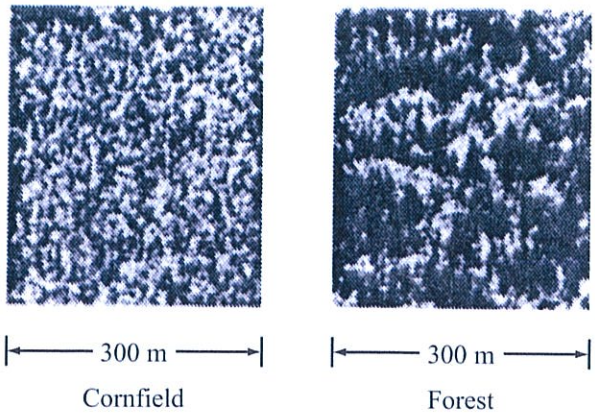

Figure 5-25: The pixel-to-pixel variation in the cornfield image is almost entirety due to Rayleigh fading (speckle), whereas the forest-parcel image includes spatial patterns (in addition to speckle) associated with the density variation of trees.

▶ ***Image texture*** refers to the intrinsic spatial variability of image tone, beyond that caused by speckle, due to corresponding spatial variabilities in the physical and/or electromagnetic properties of the distributed target. ◀

Consider the two image segments shown in Fig. 5-25, one of which belongs to an agricultural field (corn) and the other belongs to a forest parcel. A radar image of a cornfield is essentially textureless if the image pixel contains many rows of corn, whereas that of the forest parcel is highly textured, typical of a sparse forest that may have a dense canopy in some areas and mostly open spaces in others.

Image texture is a useful property that can be used in computer classification of radar images, particularly when attempting to discriminate between different classes of distributed targets with comparable average tones (reflectivities). Image textural attributes in common use include:

(a) the ***texture autocorrelation function***, which is a measure of the degree of similarity between a given pixel and its neighboring pixels.

(b) The ***texture standard deviation***, representing pixel-to-pixel variability over and above that due to speckle.

(c) Orientation or periodic textural patterns, if either exists.

In addition to the numerous useful papers available in the literature on radar image texture (Collins and Huang, 1998; Glaister et al., 2013; Collins and Allan, 2009; De Grandi et al., 2007), a highly recommended source is the authoritative book by Oliver and Quegan (2004), which not only discusses image texture in great detail, but also provides a comprehensive review of the various types of filters available for despeckling radar images.

5-9.2 Despeckling Filters

► An ideal ***despeckling filter*** is able to remove speckle from a radar image while preserving texture, and to do so without sacrificing spatial resolution. No such filter exists, but several of the available filters provide products that are far superior to the original speckled images. ◄

In their book on *Understanding SAR Images* (2004), Oliver and Quegan describe despeckle filters as "RCS reconstruction filters," meaning that a despeckle filter should generate an image of σ^0, the radar cross section per unit area of the imaged scene, without the speckle pattern.

Figure 5-26(a) displays a 2-look airborne SAR image with a spatial resolution of 3 m × 3 m. Given that N is only 2, the image exhibits the standard speckle appearance. The remaining six images are images filtered using a variety of different image processing algorithms. They include:

(a) Multilook Filter [Fig. 5-26(b)]: The image intensity I of a given pixel in an N-look image is assigned a value equal to μ_I, where μ_I is the average intensity of M^2 pixels contained in an $M \times M$ window centered at the given pixel. The image in Fig. 5-26(b) was generated by applying multilook averaging over an 11×11 window. With this type of primitive filter, the averaging process removes the speckle, but the image has a blurry appearance. Even though the number of pixels in the image has not changed, the averaging process, in effect, degrades the spatial resolution of the image. In practice this type of filter is of limited utility.

(b) Minimum Mean-Square Error (MMSE) Filter [Fig. 5-26(c)]: Instead of replacing the intensity I of a given pixel with μ_I (the average intensity over the $M \times M$ window), it is replaced with an intensity I' that incorporates information about the local statistics within the $M \times M$ window. Intensity I' is related to I and μ_I by

$$I' = \mu_I + \alpha(I - \mu_I), \tag{5.95}$$

where α is a parameter that gauges the degree of uniformity within the $M \times M$ window (Oliver and Quegan, 2004). For a window containing uniform terrain with constant σ, α is set to 0, in which case $I' = \mu_I$. On the other extreme, if the window contains multiple classes of targets with very different σ values, α is assigned a value of 1; consequently, $I' = I$, which means that the pixel intensity remains unchanged. To estimate the appropriate value of α for each pixel, a minimum-mean-square-error criterion is applied to the ***multiplicative intensity model*** given by Eq. (5.84), namely

$$I = \sigma F, \tag{5.96}$$

where I is the N-look intensity of the pixel, σ is its true reflectivity, and F is the fading random variable for an N-look intensity image (for the sake of simplicity, the system constant has been set to 1 and the subscript N has been suppressed).

If the window contains a uniform target with a constant σ, it follows that the ***normalized variance*** β_I of I is equal to the normalized variance β_F of F:

$$\beta_I = \left(\frac{s_I}{\mu_I}\right)^2 = \left(\frac{s_F}{\mu_F}\right)^2 = \frac{1}{N} \qquad \textbf{(uniform } \sigma\textbf{)}, \tag{5.97}$$

where in the last step we used Eq. (5.85). The values of the mean intensity μ_I and standard deviation s_I are estimated using the M^2 intensity values of the pixels in the window centered at the pixel under consideration.

However, if the window contains more than one class of targets, σ is no longer uniform across it, which means that it should be treated as a random variable with

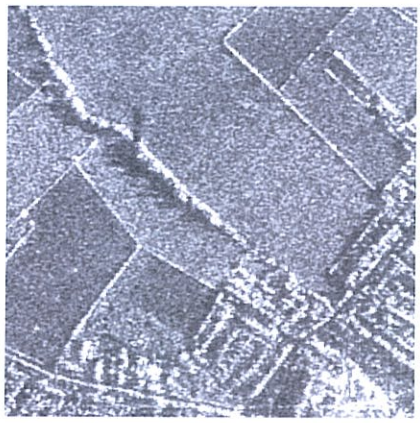

Unfiltered image

(a) DRA X-band airborne SAR image of a rural scene: 3 m resolution, 2-look

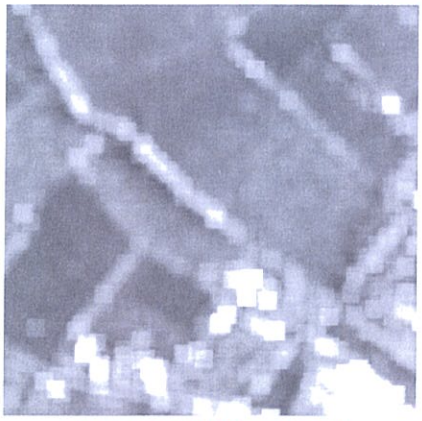

(b) Despeckled: multilook

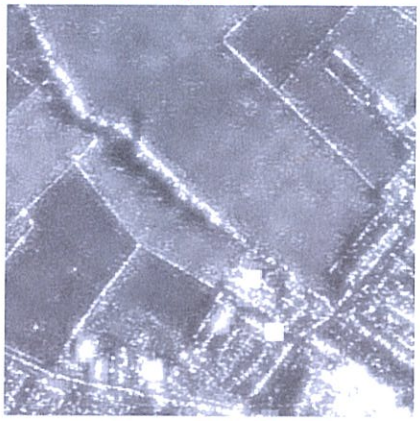

(c) Despeckled: MMSE

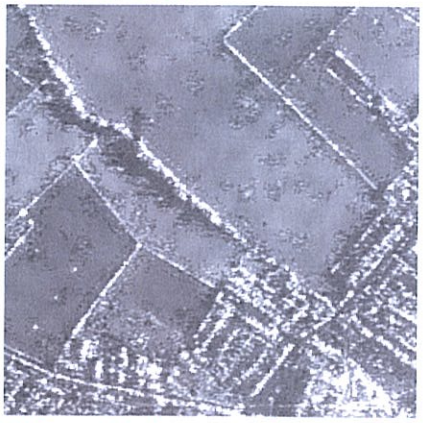

(d) Despeckled: structural gamma MAP

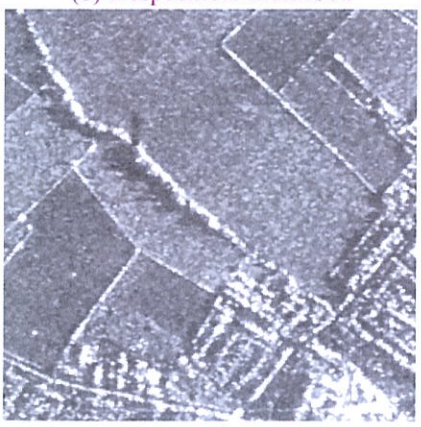

(e) Despeckled: CML

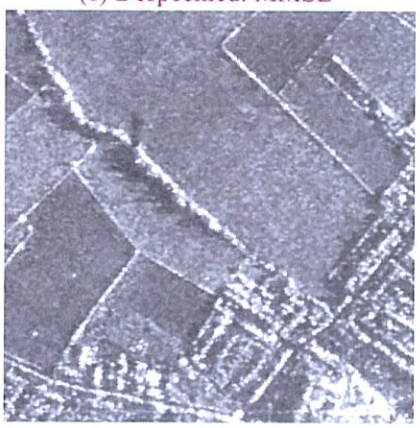

(f) Despeckled: CMAP

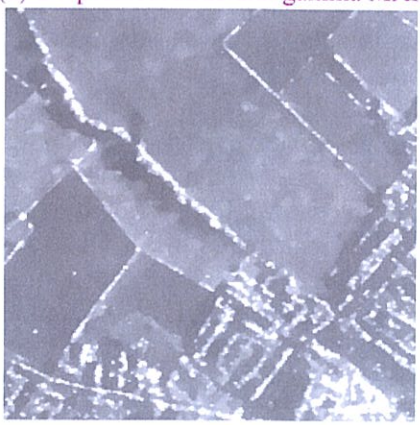

(g) Despeckled: Crimmins

Figure 5-26: The 3 m × 3 m resolution 2-look image in (a) was subjected to six different despeckling filters [courtesy of Oliver and Quegan].

mean μ_σ and standard deviation s_σ. Statistically, σ and F_N are independent random variables. Hence,

$$\mu_I = \mu_\sigma \mu_F, \tag{5.98a}$$

$$\mu_{I^2} = \mu_{\sigma^2} \mu_{F^2}, \tag{5.98b}$$

and the normalized variance of I is

$$\beta_I = \left(\frac{s_I}{\mu_I}\right)^2 = \frac{\mu_{I^2} - \mu_I^2}{\mu_I^2} = \frac{\mu_{\sigma^2}\mu_{F^2} - \mu_\sigma^2 \mu_F^2}{\mu_\sigma^2 \mu_F^2}. \tag{5.99}$$

In view of the moments $\mu_F = 1$ and $\mu_{F^2} = 1 + 1/N$, Eq. (5.99) becomes

$$\beta_I = \left(\frac{\mu_{\sigma^2}}{\mu_\sigma^2}\right)\left(1 + \frac{1}{N}\right) - 1. \tag{5.100}$$

The normalized variance of σ is

$$\beta_\sigma = \left(\frac{s_\sigma}{\mu_\sigma}\right)^2 = \frac{\mu_{\sigma^2} - \mu_\sigma^2}{\mu_\sigma^2} = \left(\frac{\mu_{\sigma^2}}{\mu_\sigma^2}\right) - 1. \tag{5.101}$$

The parameter α is defined as the ratio of the reflectivity variance β_σ to the intensity variance β_I,

$$\alpha = \frac{\beta_\sigma}{\beta_I} = \frac{\beta_I - 1/N}{\beta_I\left(1 + \frac{1}{N}\right)} \qquad \textbf{(any } \sigma \textbf{ variation)}. \tag{5.102}$$

The expression given by Eq. (5.102) is obtained by combining the expressions in Eqs. (5.100) and (5.101) to eliminate the ratio $(\mu_{\sigma^2}/\mu_\sigma^2)$. The intensity variance β_I is calculated using the M^2 intensity values. For an image window of a textureless distributed target (σ = constant), β_I should be close to $1/N$, in which case $\alpha \approx 0$. In contrast, for a textured window, $\beta_I > 1/N$.

Application of the MMSE filter to the original image shown in Fig. 5-26(a) leads to the image in Fig. 5-26(c). The filter is successful in suppressing speckle while preserving image features such as roads and boundaries.

(c)–(e) Bayesian Filters [Fig. 5-26(d) to (f)]: The filters used in generating the despeckled images shown in Fig. 5-26(d) to (f) all are based on Bayesian statistics, which uses conditional probabilities in combination with assumed pdf models for the reflectivity σ. For more details, the reader is referred to the book by Oliver and Quegan (2004) and its comprehensive list of references.

5-10 Coherent and Noncoherent Scattering

5-10.1 Surface Roughness

Consider the ground surface shown in Fig. 5-27(a). Let us assume that the surface height $z(x,y)$ varies randomly and isotropically with x and y, which means that $z(x,y)$ has the same statistical properties across any straight line segment of the ground surface. An example of a one-dimensional height profile for such a random surface is shown in Fig. 5-27(b). We label it $z(x)$. Upon digitizing the profile and arranging its values into "height bins" relative to the mean surface $\langle z \rangle = 0$, we obtain the ***height probability density function*** $p(z)$ displayed in Fig. 5-27(c). The measured pdf looks approximately Gaussian in shape, which is true for most random surfaces. That is,

$$p(z) = \frac{1}{\sqrt{2\pi s^2}} e^{-z^2/2s^2}, \tag{5.103}$$

where s^2 is the variance of surface heights (and since $\langle z \rangle = 0$, s is the standard deviation).

Given $p(z)$, we can calculate several statistical attributes of the random surface, including:

(a) The height standard deviation s given by

$$s = \langle z^2 \rangle^{1/2} = \left[\int_{-\infty}^{\infty} z^2\, p(z)\, dz\right]^{1/2}, \tag{5.104}$$

which also is called the ***rms height***, and

(b) the ***surface correlation function*** defined by

$$\rho(\xi) = \frac{\langle z(x,y)\, z(x',y')\rangle}{s^2}, \tag{5.105}$$

where $u = x - x'$, $v = y - y'$, and $\xi = \sqrt{u^2 + v^2}$ is the lateral separation between the two locations, (x,y) and (x',y') on the surface. The correlation function $\rho(\xi)$ is a measure of the degree of correlation between the surface at location (x,y) and the surface at location (x',y').

The correlation function for the random surface under consideration is shown in Fig. 5-27(d). As expected, the correlation function decreases with ξ, so that if the spacing between two locations is greater than a

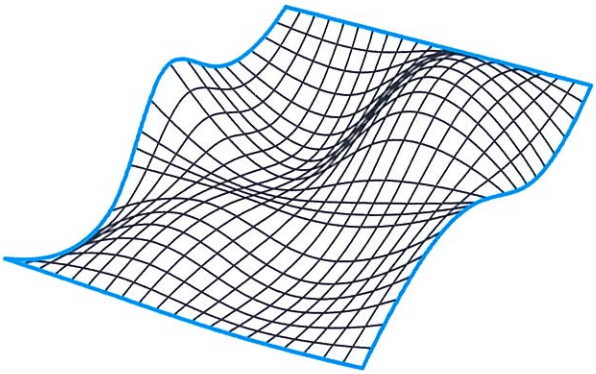

(a) Random surface

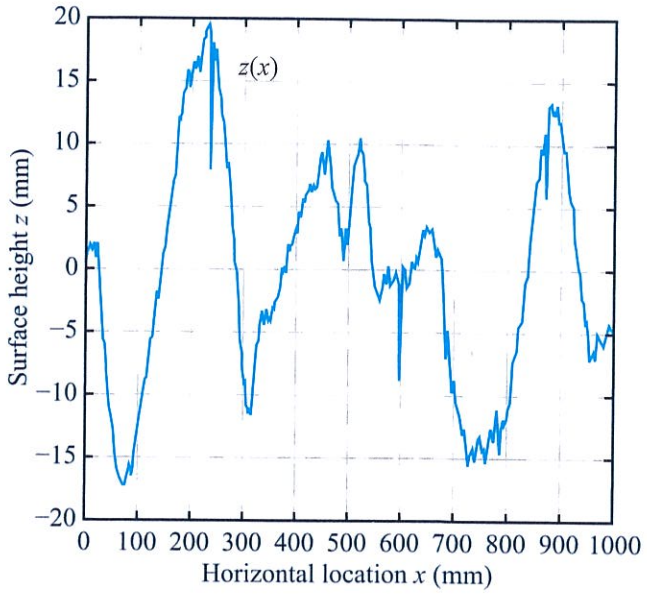

(b) Height profile

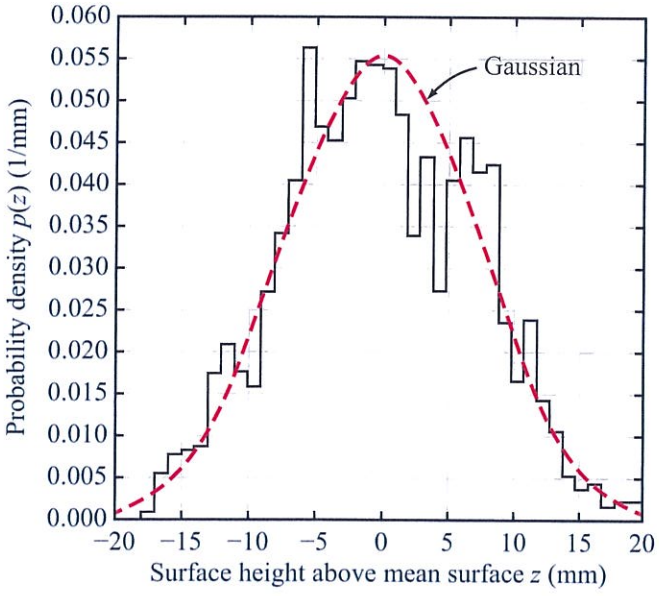

(c) Histogram

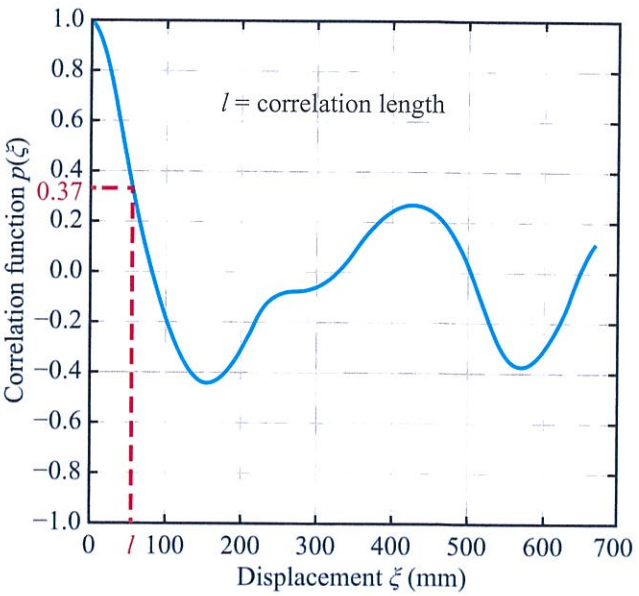

(d) Correlation function

Figure 5-27: Random, isotropic surface $z(x,y)$: (a) pictorial view, (b) measured height profile $z(x)$, (c) pdf of digitized height profile, and (d) autocorrelation function $\rho(\xi)$, where ξ is the displacement between two points on the surface.

certain distance called the ***correlation length*** l, then the heights at the two locations are considered statistically uncorrelated. The correlation length l is defined as the separation $\xi = l$ for which

$$\rho(\xi) = e^{-1} \qquad (\text{at } \xi = l). \tag{5.106}$$

For the correlation function displayed in Fig. 5-27(d), $l = 52.5$ mm. Because the measurement precision of $z(x,y)$ is limited by the tool (such as a laser profiler) used to profile the surface height, the correlation function $\rho(\xi)$ exhibits noise-like oscillations beyond about $\xi = 100$ mm. Negative values of $\rho(\xi)$ are an artifact of the measurement process.

As discussed later in Chapter 10, models for electromagnetic scattering by random rough surfaces involve the use of assumed functional forms for the correlation function $\rho(\xi)$. The two most common forms are the ***exponential correlation function*** $\rho_e(\xi)$ and the ***Gaussian correlation function*** $\rho_G(\xi)$, defined as:

$$\rho_e(\xi) = e^{-|\xi|/l} \qquad \textbf{(exponential)}, \tag{5.107a}$$

$$\rho_G(\xi) = e^{-\xi^2/l^2} \qquad \textbf{(Gaussian)}, \tag{5.107b}$$

where l is the correlation length of the surface. Plots of both functions are shown in Fig. 5-28 as a function of the normalized displacement ξ/l. Experimental measurements of $\rho(\xi)$ for random soil surfaces tend to favor the applicability of the exponential correlation function (Nashashibi and Ulaby, 2007).

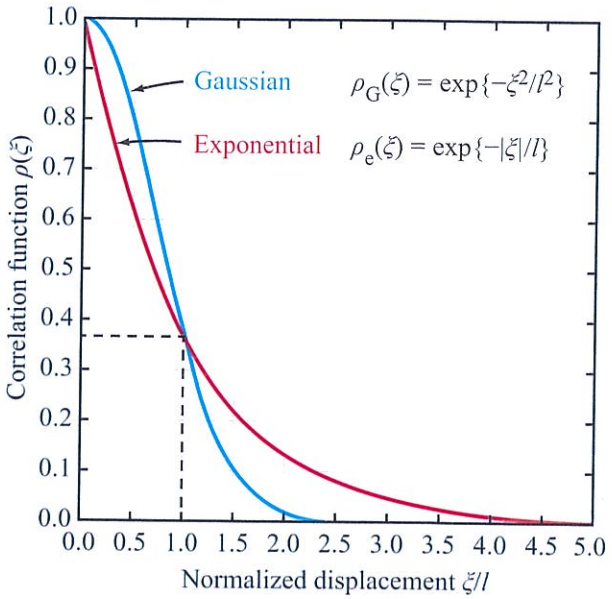

Figure 5-28: Exponential and Gaussian correlation functions.

5-10.2 Bistatic Scattering

Electromagnetically, the roughness of a surface is measured relative to the EM wavelength λ. For a surface with rms height s, its ***electromagnetic roughness*** ks is

$$ks = \frac{2\pi}{\lambda} s \qquad \textbf{(EM roughness)}. \tag{5.108}$$

In the general case, bistatic scattering involves four angles: incidence and scattering angles θ_i and θ_s and azimuth angles ϕ_i and ϕ_s (Fig. 5-29), but for a random isotropic surface, the x and y axes are arbitrary, so only one azimuth angle is sufficient, namely $\phi = \phi_s - \phi_i$. In terms of θ_i, θ_s, and ϕ, we define the following terms:

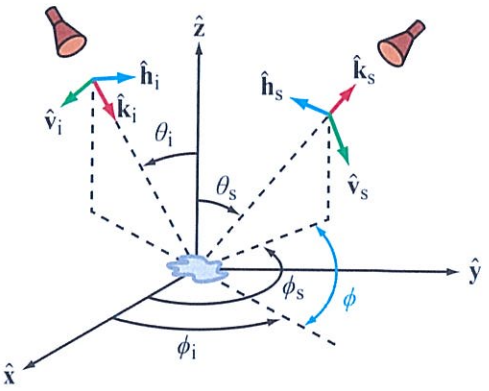

Figure 5-29: Bistatic-scattering coordinate system.

(a) Specular direction: $\theta_i = \theta_s$ and $\phi = 0$,

(b) Plane of incidence: $\phi = 0$,

(c) Out of the plane of incidence: $\phi \neq 0$,

(d) Backscattering direction: $\theta_i = \theta_s$ and $\phi = 180°$.

For a perfectly smooth surface with rms height $s = 0$, an incident EM wave with polarization p (where $p =$ h or v) is reflected along the specular direction and the reflected power P_p^{r} is related to the incident power P_p^{i} by Eq. (2.108), namely

$$P_p^{\mathrm{r}} = \Gamma^p P_p^{\mathrm{i}} \qquad (p = \text{v or h polarization}), \qquad (5.109a)$$

(specular surface)

where Γ^p is the p-polarized Fresnel reflectivity of a perfectly flat surface. Figure 5-30 depicts the scattering patterns for three surfaces with varying degrees of electromagnetic roughness. The pattern for the perfectly smooth surface is essentially a delta function, as shown in Fig. 5-30(a). The component of the scattering pattern along the specular direction is called the ***coherent component*** because the reflected wave has a uniform phase front. The scattering pattern of the perfectly smooth surface consists of only a coherent component.

If the surface is slightly rough with ks on the order of 0.1, the scattering pattern continues to be dominated by the coherent component along the specular direction, as shown in Fig. 5-30(b), but the pattern also includes a ***noncoherent component*** along all other directions. In that case, the power reflected along the specular direction is related to the incident power by

$$P_p^{\mathrm{r}} = \Gamma_{\mathrm{coh}}^p P_p^{\mathrm{i}}, \qquad (5.109b)$$

(nonspecular surface)

where Γ_{coh}^p is the ***coherent reflectivity***. The relationship between Γ_{coh}^p and Γ^p is introduced shortly.

Furthermore, the incoherent component contains not only waves with the same polarization as that of the incident wave, but also waves with the orthogonal polarization. That is, if the incident wave is h polarized, the scattering noncoherent component consists of both h-polarized (***co-pol***) and v-polarized (***cross-pol***) components. If the surface roughness is increased to $ks > 2$, the coherent component becomes negligibly small and the noncoherent component becomes dominant along all directions, including the specular direction [Fig. 5-30(c)].

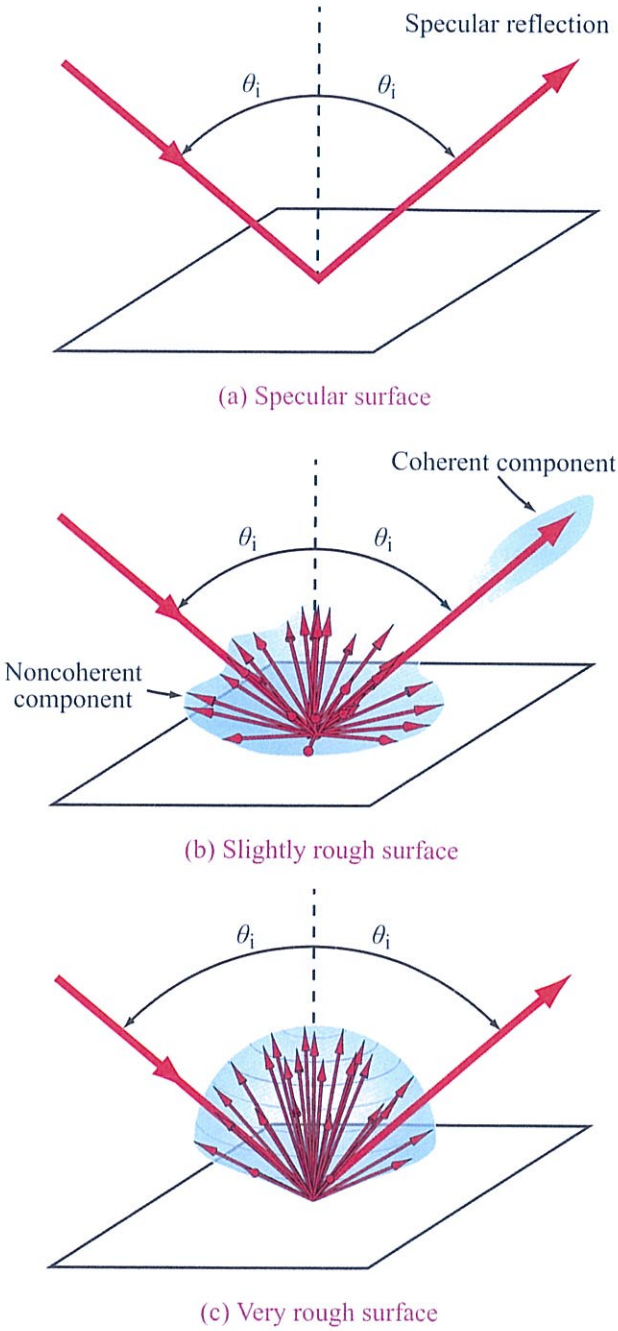

Figure 5-30: The bistatic-scattering pattern consists of a coherent component along the specular direction and a noncoherent component along all directions. For a perfectly smooth surface, only the coherent component exists, and at the opposite extreme, for a very rough surface the coherent component becomes negligibly small in comparison with the noncoherent component.

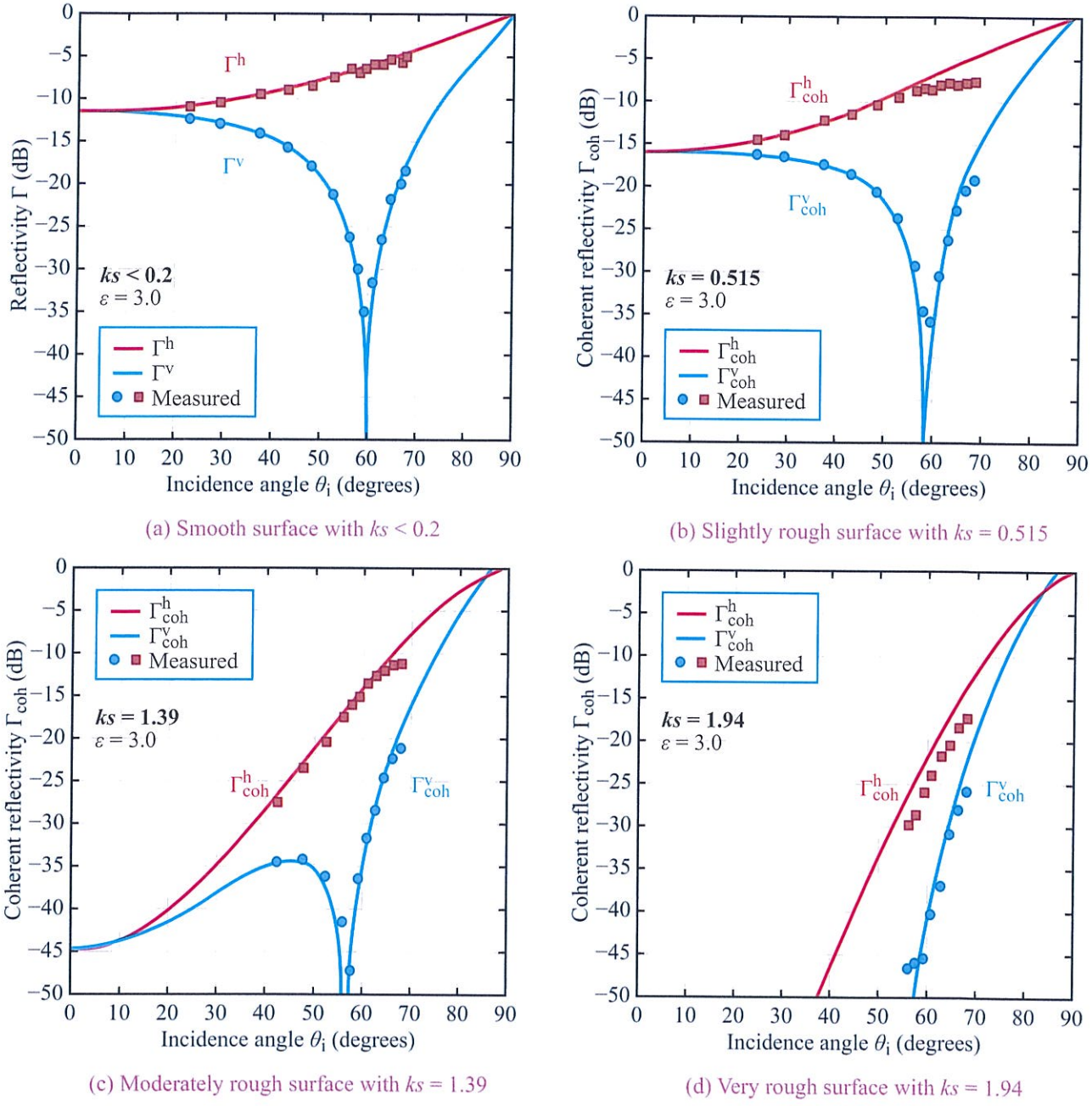

(a) Smooth surface with $ks < 0.2$

(b) Slightly rough surface with $ks = 0.515$

(c) Moderately rough surface with $ks = 1.39$

(d) Very rough surface with $ks = 1.94$

Figure 5-31: Measured and calculated reflectivities for h and v polarizations for four surfaces with different EM roughnesses [De Roo and Ulaby, 1994].

5-10.3 Specular Reflectivity

Using an X-band bistatic radar facility, De Roo and Ulaby (1994) measured the bistatic-scattering pattern for several sand surfaces with varying roughnesses. The smoothest surface they measured had an electromagnetic roughness $ks < 0.2$, and the electromagnetic roughness of the roughest random surface was $ks = 1.94$, which is about an order of magnitude greater than that of the smoothest surface. Figure 5-31(a) displays the measured specular reflectivities Γ^{v} and Γ^{h} of the smoothest surface as a function of the incidence angle θ_{i}. Also shown are plots calculated on the basis of the Fresnel reflection coefficient equation given by Eqs. (2.101) and (2.102a) for a specular surface and the relations $\Gamma^{\mathrm{v}} = |\rho_{\mathrm{v}}|^2$ and $\Gamma^{\mathrm{h}} = |\rho_{\mathrm{h}}|^2$. The sand dielectric permittivity used in the calculation is $\varepsilon = 3$. We observe that the measured data are in very close agreement with the calculated plots, implying that a surface may be considered perfectly flat if its electromagnetic roughness $ks < 0.2$.

The three remaining figures in Fig. 5-31 pertain to much rougher surfaces. The calculated plots, which are in close agreement with the measured reflectivities, are based on the relationship

$$\Gamma^p_{\mathrm{coh}} = \Gamma^p \, e^{-4\psi^2} \qquad (p = \mathrm{v \text{ or } h}), \tag{5.110}$$

where

$$\psi = ks\cos\theta_{\mathrm{i}} = \frac{2\pi}{\lambda} s\cos\theta_{\mathrm{i}}, \tag{5.111}$$

and Γ^p is the Fresnel reflectivity for polarization p given by the expressions in Table 2-5. To appreciate the sensitivity of Γ^p_{coh} to ks, let us consider two roughness cases, both at $\theta_{\mathrm{i}} = 45°$:

(a) Relatively smooth surface with $ks = 0.2$:

$$\Gamma^p_{\mathrm{coh}} = 0.92\,\Gamma^p.$$

(b) Very rough surface with $ks = 2$:

$$\Gamma^p_{\mathrm{coh}} = 3.35 \times 10^{-4}\Gamma^p.$$

► Increasing the EM roughness from 0.2 to 2 causes the reflectivity to decrease by more than three orders of magnitude. ◄

The variation of $\Gamma^p_{\mathrm{coh}}/\Gamma^p$ with $\psi = ks\cos\theta_{\mathrm{i}}$ is shown in Fig. 5-32(a), and angular plots of $\Gamma^{\mathrm{v}}_{\mathrm{coh}}$ are shown in Fig. 5-32(b) for multiple values of the electromagnetic roughness parameter ks. Note that the vertical axis is in dB, so the observed reduction in level as a function of increasing roughness is very significant, and much more so at angles below the Brewster angle than above it.

The expression given by Eq. (5.110) is called the zeroth-order physical-optics solution for reflection by a rough surface (De Roo and Ulaby, 1994). Whereas the model provides very good agreement to experimental observations, it does not predict a rather subtle shift in the location of the Brewster angle (Saillard and Maystre, 1990; Greffet, 1992). De Roo and Ulaby (1994) demonstrated that the location of the Brewster angle can be predicted with excellent accuracy by using a second-order physical-optics model, which also is predicted by the I^{2}EM model presented in Section 10-3.

5-10.4 Bistatic-Scattering Coefficient

In the preceding subsection, we examined the dependence of the coherent reflectivity Γ_{coh} of a continuous two-dimensional surface on surface roughness. Now, we extend the discussion to the bistatic-scattering coefficient of the surface, σ^0. The two quantities are related, but distinct.

The q-polarized coherent reflectivity $\Gamma^q_{\mathrm{coh}}(\theta_{\mathrm{i}})$ is an idealized quantity defined for a continuous, infinite, two-dimensional surface; its definition relies on plane-wave incidence and plane-wave reflection. For an area A of the surface, $\Gamma^q_{\mathrm{coh}}(\theta_{\mathrm{i}})$ is given by Eq. (5.109a) as

$$\Gamma^q_{\mathrm{coh}}(\theta_{\mathrm{i}}) = \frac{P^{\mathrm{r}}_q}{P^{\mathrm{i}}_q} = \frac{\mathcal{S}^{\mathrm{r}}_q A\cos\theta_{\mathrm{i}}}{\mathcal{S}^{\mathrm{i}}_q A\cos\theta_{\mathrm{i}}} = \frac{\mathcal{S}^{\mathrm{r}}_q}{\mathcal{S}^{\mathrm{i}}_q} \qquad (q = \mathrm{v \text{ or } h}), \tag{5.112}$$

where $\mathcal{S}^{\mathrm{i}}_q$ and $\mathcal{S}^{\mathrm{r}}_q$ are the q-polarized power densities of the incident and reflected plane waves. In contrast, the bistatic-scattering cross section σ_{pq} is defined by Eq. (5.27a) as

$$\sigma_{pq} = \frac{P^{\mathrm{rer}}_p}{\mathcal{S}^{\mathrm{i}}_q}, \tag{5.113}$$

where P^{rer}_p is the p-polarized power reradiated by the target. For a distributed surface of area A, its scattering

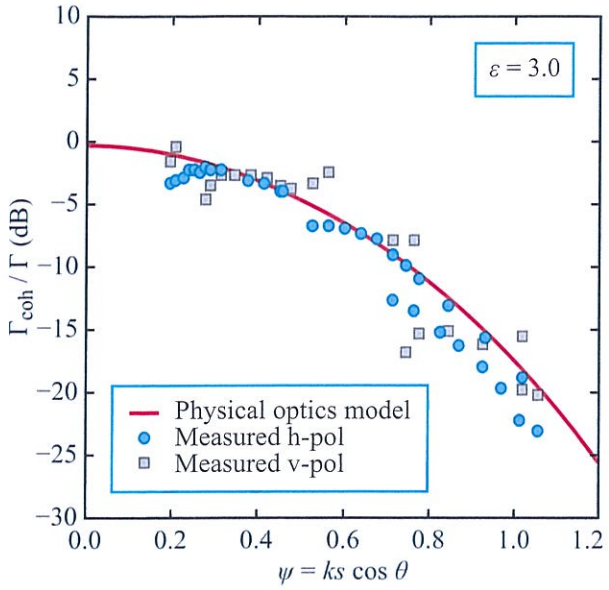

(a) $\Gamma_{\rm coh}$ / Γ vs. roughness parameter

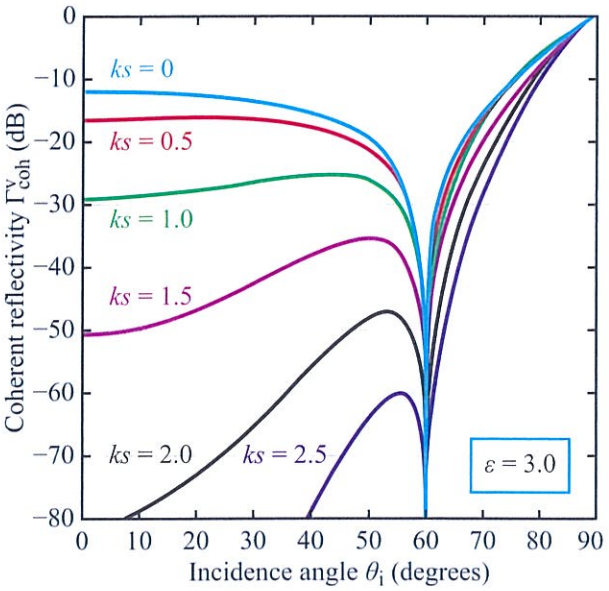

(b) $\Gamma^{\rm v}_{\rm coh}(\theta)$ at various surface roughnesses

Figure 5-32: Variation of (a) $\Gamma_{\rm coh}/\Gamma$ with $\psi = ks\cos\theta$ and (b) $\Gamma^{\rm v}_{\rm coh}$ with $\theta_{\rm i}$ for various values of ks [De Roo and Ulaby, 1994].

coefficient is $\sigma^0 = \sigma/A$. Also, the reradiated power spreads spherically, so at a range $R_{\rm r}$ from the surface, the power density of the scattered wave is $\mathcal{S}^{\rm s}_p = P^{\rm rer}/(4\pi R_{\rm r}^2)$. Hence,

$$\sigma^0_{pq} = \frac{1}{A}\frac{P^{\rm rer}_p}{\mathcal{S}^{\rm i}_q} = \left(\frac{4\pi R_{\rm r}^2}{A}\right)\frac{\mathcal{S}^{\rm s}_p}{\mathcal{S}^{\rm i}_q}. \tag{5.114}$$

Coherent component

In general, the *total* co-polarized bistatic-scattering coefficient σ^0_{pp} consists of a ***coherent component*** $\sigma^0_{pp_{\rm coh}}$ and an ***incoherent component*** $\sigma^0_{pp_{\rm inc}}$:

$$\sigma^0_{pp}(\theta_{\rm i},\phi_{\rm i};\theta_{\rm s},\phi_{\rm s}) = \sigma^0_{pp_{\rm coh}}(\theta_{\rm i}) + \sigma^0_{pp_{\rm inc}}(\theta_{\rm i},\phi_{\rm i};\theta_{\rm s},\phi_{\rm s}), \quad p = \text{h or v}, \tag{5.115}$$

where $(\theta_{\rm i},\phi_{\rm i})$ and $(\theta_{\rm s},\phi_{\rm s})$ define the incident and scattering directions as shown in Fig. 5-29.

▶ The cross-polarized component does not have a coherent component. ◀

The coherent component, which exists only along a narrow angular range around the specular direction, is given by

$$\sigma^0_{pp_{\rm coh}}(\theta_{\rm i}) = 4\pi\cos\theta_{\rm i}\,\Gamma^p(\theta_{\rm i})\,e^{-4\psi^2} \cdot \delta(\cos\theta_{\rm i} - \cos\theta_{\rm s})\,\delta(\phi_{\rm i} - \phi_{\rm s}), \tag{5.116}$$

where ψ is the roughness parameter defined by Eq. (5.111). The presence of the delta functions in Eq. (5.116) asserts that $\sigma^0_{pp_{\rm coh}}$ is nonzero only when $\theta_{\rm i} = \theta_{\rm s}$ and $\phi_{\rm i} = \phi_{\rm s}$. The factor $4\pi\cos\theta_{\rm i}$ is associated with the definition of σ^0. To demonstrate the validity of Eq. (5.116), consider the case of a flat surface with no roughness. For $s = 0$, $\psi = 0$ and so the incoherent component is zero, in which case σ^0_{pp} reduces to $\sigma^0_{pp_{\rm coh}}$,

$$\sigma^0_{pp}(\theta_{\rm i}) = \sigma^0_{pp_{\rm coh}}(\theta_{\rm i}) = 4\pi\cos\theta_{\rm i}\,\Gamma^p(\theta_{\rm i}) \cdot \delta(\cos\theta_{\rm i} - \cos\theta_{\rm s})\,\delta(\phi_{\rm i} - \phi_{\rm s}). \tag{5.117}$$

At a distance R_r from the flat surface, the total p-polarized scattered (reflected) power is related to the scattered power density $\mathcal{S}_p^s$ by

$$P_p^s = \iint_{\text{upper hemisphere}} \mathcal{S}_p^s R_r^2 \, d\Omega_s. \tag{5.118}$$

Using Eq. (5.114), with $p = q$, and Eq. (5.117) in Eq. (5.118) leads to

$$\begin{aligned} P_p^s &= \iint \frac{\mathcal{S}_p^i A}{4\pi R_r^2} \sigma_{pp}^0 R_r^2 \, d\Omega_s \\ &= \iint \frac{\mathcal{S}_p^i A}{4\pi} (4\pi \cos\theta_i) \, \Gamma^p(\theta_i) \\ &\quad \cdot \delta(\cos\theta_i - \cos\theta_s) \, \delta(\phi_i - \phi_s) \, d\Omega_s \\ &= P_p^i \, \Gamma^p(\theta_i), \end{aligned} \tag{5.119}$$

where we used the relation $P_p^i = \mathcal{S}_p^i A \cos\theta_i$ for the p-polarized power incident upon the surface. The result given by Eq. (5.119) is equivalent to Eq. (5.109a), the basic equation that defines the Fresnel reflectivity Γ^p as the ratio of the power reflected from a perfectly flat surface to the incident power.

Incoherent component

► Increasing the roughness of a surface causes a transfer of energy from the coherent component to the incoherent component, as well as to increased depolarization. ◄

The redistribution of energy across the upper hemisphere depends on the geometrical, dielectric, and statistical properties of the surface, as discussed in more detail in Chapter 10.

Figure 5-33 displays a 3-D bistatic-scattering pattern of the scattering coefficient σ_{hh}^0 for a sand surface whose rms height s is estimated to be smaller than 0.1 cm. The measurements were made by a 35 GHz bistatic radar, so the corresponding electromagnetic roughness is $ks = (2\pi s/\lambda) = 0.73$, which makes the surface slightly rough electromagnetically. The incidence angle

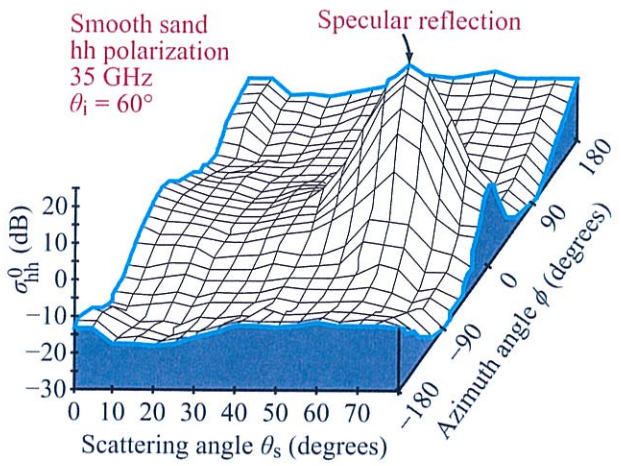

Figure 5-33: Measured bistatic-scattering pattern for a sand surface with $ks = 0.73$ at 35 GHz [Ulaby et al., 1988d].

is 60° and both the transmit and receive antennas are horizontally polarized. We observe that the pattern has a peak along the direction $\theta_s = \theta_i = 60°$ and $\phi = 0$, corresponding to the specular direction. This peak is the coherent bistatic-scattering component $\sigma_{hh_{coh}}^0$. Another example, shown in Fig. 5-34 for a rough surface with $ks = 3.28$, includes 3-D patterns for the vv-polarized scattering coefficient σ_{vv}^0 and the ***depolarized ratio*** defined as

$$\chi = \frac{\sigma_{hv}^0 + \sigma_{vh}^0}{\sigma_{hh}^0 + \sigma_{vv}^0}. \tag{5.120}$$

We note that maximum depolarization occurs in the plane $\phi = 90°$, which is orthogonal to the plane of incidence.

5-10.5 Backscattering Response of a Smooth Surface

In the backscattering direction, the total co-polarized backscattering coefficient at incidence angle θ_i consists of a coherent component $\sigma_{pp_{coh}}^0(\theta_i)$, which is important only at or near normal incidence, and an incoherent

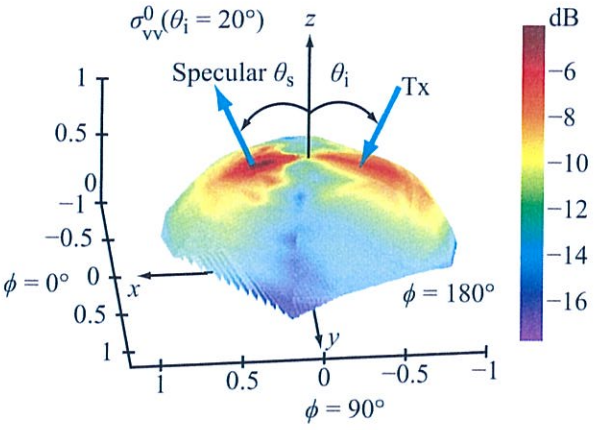

(a) σ^0_{vv}

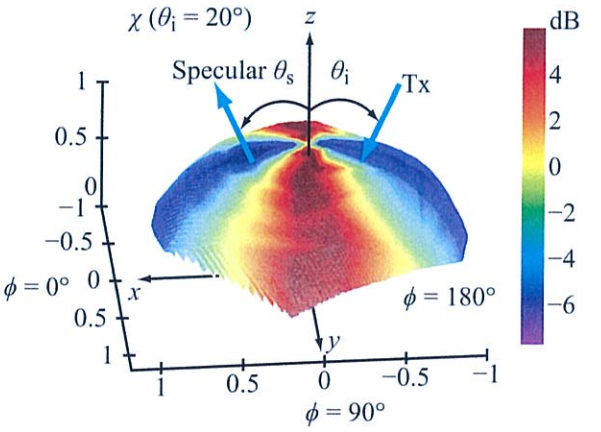

(b) Depolarization ratio χ

Figure 5-34: Measured bistatic-scattering patterns for a rough surface: (a) σ^0_{vv} and (b) χ [Nashashibi and Ulaby, 2007].

component $\sigma^0_{pp_{inc}}(\theta_i)$, which is important at all angles:

$$\sigma^0_{pp}(\theta_i) = \sigma^0_{pp_{coh}}(\theta_i) + \sigma^0_{pp_{inc}}(\theta_i). \tag{5.121}$$

For a p-polarized antenna pointed along a direction θ_i relative to normal incidence, the coherent backscattering coefficient is given by Eq. (5.116), which treats the coherent component as a pure delta function. In reality, $\sigma^0_{pp_{coh}}$ has a finite beamwidth surrounding the specular direction, so we use the approximate expression (Ulaby et al., 1983)

$$\sigma^0_{pp_{coh}} = \frac{\Gamma^p(\theta_i)}{\beta_c^2} \exp(-4k^2s^2) \exp\left(\frac{-\theta_i^2}{\beta_c^2}\right), \tag{5.122}$$

where $\Gamma^p(\theta_i)$ is the p-polarized Fresnel reflectivity, $k = 2\pi/\lambda$, s is the surface rms height, and β_c is an effective width of the angular extent of $\sigma^0_{pp_{coh}}$. Both θ_i and β_c are in radians, and in the derivation leading to Eq. (5.122), it was assumed that the range is sufficiently large to satisfy the far-field criterion for the antenna and θ_i is sufficiently small to permit making the approximations $\sin\theta_i \approx \theta_i$ and $\cos\theta_i \approx 1$. The factor $\exp(-4k^2s^2)$ accounts for the reduction of the Fresnel reflectivity due to surface roughness, consistent with Eqs. (5.110) and (5.111).

For a specular surface with $s = 0$, the expression given by Eq. (5.122) leads to the same result for the power received from a specular surface at normal incidence as does the application of the image method to the Friis transmission formula given by Eq. (3.39). In the image method, the transmit antenna "sees" its image in the reflection and hence may be modeled as two communication antennas with the same gain G_0, separated by a distance $2h$, where h is the height of the antenna above the surface. The received power in this image case, when modified by the surface nadir reflectivity Γ_0, is given by

$$P^r = \frac{P^t G_0^2 \lambda^2 \Gamma_0}{(4\pi)^2 (2h)^2} \qquad \textbf{(Friis transmission formula)}. \tag{5.123}$$

For a distributed target with only a coherent scattering coefficient $\sigma^0_{pp_{coh}}$, the radar equation given by Eq. (5.32) becomes

$$P^r = \frac{P^t \lambda^2}{(4\pi)^3} \iint \frac{G^2(\theta_i, \phi_i)}{R^4} \sigma^0_{pp_{coh}}\, dA. \tag{5.124}$$

For a specular surface with $s = 0$, $\sigma^0_{pp_{coh}}(\theta_i)$ is given by

$$\sigma^0_{pp_{coh}}(\theta_i) = \frac{\Gamma^p(\theta_i)}{\beta_c^2} \exp\left(\frac{-\theta_i^2}{\beta_c^2}\right). \tag{5.125}$$

The magnitude of β_c is on the order of 1° or smaller. Hence, the contribution to the integral of Eq. (5.124) is

insignificant for θ_i beyond a few degrees, in which case the quantity dA/R^4 may be approximated as follows:

$$\frac{dA}{R^4} = \frac{(R\,d\theta_i)(R\sin\theta_i\,d\phi_i)}{R^4} \approx \frac{\theta_i\,d\theta_i\,d\phi_i}{h^2}, \qquad (5.126)$$

where we set $R \approx h$ and $\sin\theta_i \approx \theta_i$. With $G(\theta_i, \phi_i) \approx G_0$ over the effective region of the integration in Eq. (5.124), inserting Eqs. (5.125) and (5.126) in Eq. (5.124) gives

$$P^r = \frac{P^t G_0^2 \lambda^2}{(4\pi)^3 h^2} \int_{\phi_i=0}^{2\pi} \int_{\theta_i=0}^{\pi/2} \Gamma^p(\theta_i)\, \frac{e^{-\theta_i^2/\beta_c^2}}{\beta_c^2}\, \theta_i\, d\theta_i\, d\phi_i. \qquad (5.127)$$

Since β_c is on the order of 1°, $\Gamma^p(\theta_i) \approx \Gamma^p(0) = \Gamma_0$, and the integration of the Gaussian-like function leads to

$$P^r = \frac{P^t G_0^2 \lambda^2}{(4\pi)^2 (2h)^2}\, \Gamma_0, \qquad (5.128)$$

which is identical to Eq. (5.123).

Having established that the model for $\sigma^0_{pp_{coh}}(\theta_i)$ given by Eq. (5.122) provides a reasonable mathematical representation for the coherent component of the backscattering coefficient, we now show in Fig. 5-35 plots of $\sigma_{pp_{coh}}(\theta_i)$, $\sigma_{pp_{inc}}(\theta_i)$, and their sum. The angular plot of $\sigma^0_{pp_{coh}}(\theta_i)$, which has an effective beamwidth $\beta_c = 0.51°$, was obtained from the measured values of $\sigma^0_{pp}(\theta_i)$ and the radar antenna pattern $G(\theta_i, \phi_i)$ by performing a deconvolution process. The roughness of the observed surface is $ks = 0.3$, which defines it as a relatively smooth surface. We note that at nadir, $\sigma^0_{pp_{coh}}$ is about 6 dB higher than that of the incoherent component $\sigma^0_{pp_{inc}}$, but beyond a few degrees from nadir, $\sigma^0_{pp_{coh}}$ becomes negligibly small. Since most imaging radars operate at incidence angles far away from nadir, the coherent component usually is inconsequential. The only situation of concern is when the nadir return through an antenna sidelobe interferes with the intended signal from the scene illuminated by the mainbeam of the antenna.

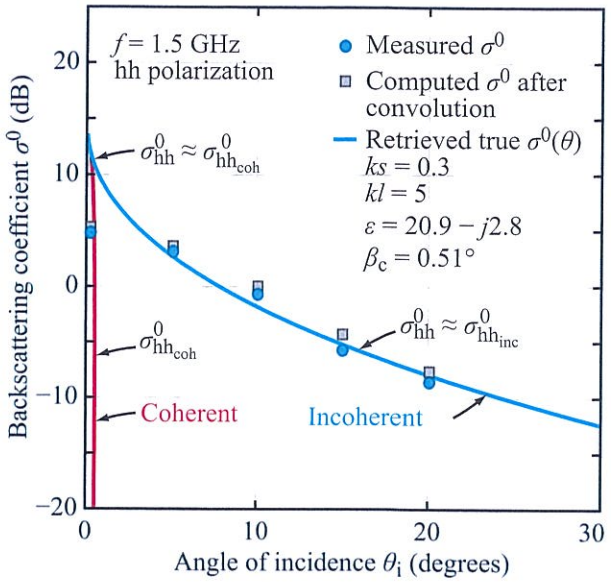

Figure 5-35: Measured and retrieved backscattering angular pattern for a surface with $ks = 0.3$ at 1.5 GHz [Ulaby et al., 1983].

5-11 Polarization Synthesis

In Section 5-3 we defined the scattering matrix of a target in the backscattering alignment (BSA) convention as

$$\mathbf{S} = \begin{bmatrix} S_{vv} & S_{vh} \\ S_{hv} & S_{hh} \end{bmatrix}, \qquad (5.129)$$

and we explained how the four elements of $\mathbf{S}$ can be measured by a radar with polarization agility. Element S_{hv}, for example, corresponds to transmitting with a v-polarized antenna and receiving with a h-polarized antenna. The typical implementation of a radar polarimeter involves transmitting a wave of one polarization and receiving echoes in two orthogonal polarizations simultaneously. This is followed by transmitting a wave with a second polarization, and again receiving echoes with both polarizations simultaneously as shown in Fig. 5-36.

Before these measurements of the scattering matrix elements are useful for further quantitative analysis and comparison to models, the measured values must be calibrated so that the final results can be converted to normalized radar cross sections. Polarimetric radar measurements require additional corrections; not only the amplitudes, but also the relative phases between

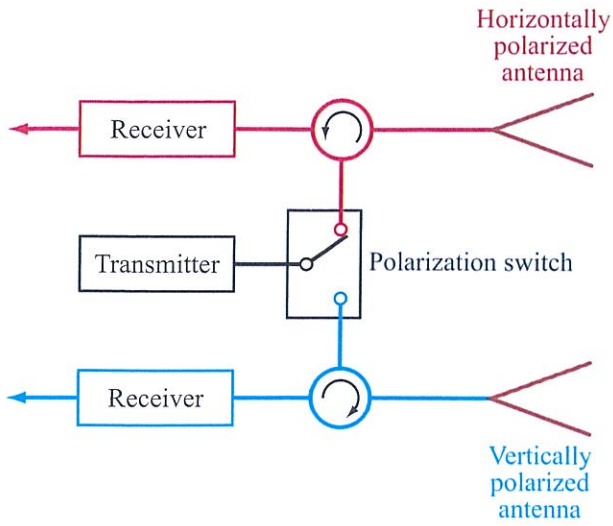

(a) Block diagram

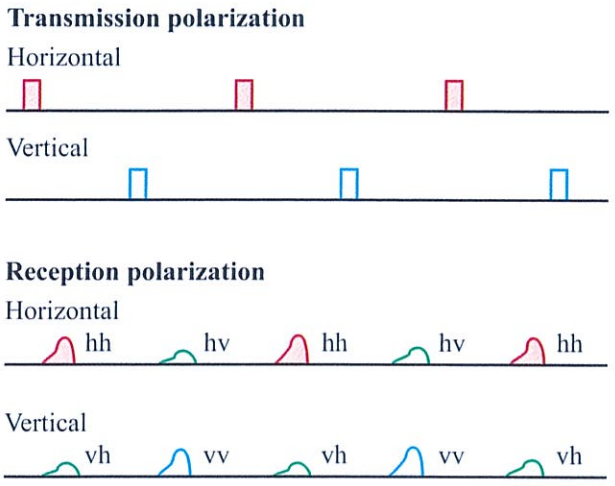

(b) Timing diagram

Figure 5-36: Calibration of polarimetric radar. A polarimetric radar is implemented by alternately transmitting signals out of horizontally and vertically polarized antennas and receiving at both polarizations simultaneously. Two pulses are needed to measure all the elements in the scattering matrix [van Zyl and Kim, 2011].

channels must be calibrated. Polarimetric radar calibration is the subject of Section 13-14.

For a target with scattering matrix $\mathbf{S}$, its pq-polarized radar cross section (RCS) is given by

$$\sigma_{pq} = 4\pi |S_{pq}|^2 \qquad (p, q = \text{h or v}). \tag{5.130}$$

(point target)

▶ The scattering matrix representation is applicable not only to point targets, but to distributed targets as well. A ***polarimetric*** imaging radar with polarization agility can generate four images, one for each of the four elements of the scattering matrix. ◀

Since S_{pq} is a complex quantity, each pixel in each of the four images is represented by a magnitude and associated phase angle. The RCS of a given ground resolution cell is related to S_{pq} by Eq. (5.130), and if the distributed target consists of a large number of resolution cells N_c, its reflectivity σ^0_{pq} is obtained from

$$\sigma^0_{pq} = \frac{4\pi}{AN_c} \sum_{i=1}^{N_c} |S^i_{pq}|^2$$

$$= \frac{4\pi}{A} \langle |\mathbf{S}_{pq}|^2 \rangle \qquad (p, q = \text{h or v}), \tag{5.131}$$

(distributed target)

where S^i_{pq} is the pq-polarized scattering amplitude of the ith pixel and A is the area of the corresponding resolution cell. Since, according to Eq. (5.22b), $S_{vh} = S_{hv}$, it follows that $\sigma^0_{vh} = \sigma^0_{hv}$, which means that a polarimetric imaging radar generates three distinct complex images, not four.

At this juncture, we stop to pose the following questions:

Q_1: Do hh, vv, and hv images of terrain contain the same or different information about the terrain?

A_1: As we will learn in a later section, the backscatter from a terrain surface or volume (such as vegetation) depends on two sets of parameters, the physical (and hence dielectric) properties of the

terrain surface or volume and the sensor parameters, namely the wavelength, incidence angle, and transmit/receive polarization mode. Consequently, two terrain classes that may appear almost indistinguishable in an hh-polarized image may exhibit markedly different tones in an hv-polarized image. So the simple answer is: yes, different polarization modes carry different information and the combination of images at multiple polarizations offers distinct advantages in many applications.

Q2: A polarimetric radar measures images of S_{pq}, which is a complex quantity. If the images are converted into σ^0_{pq} images, what happens to the phase of S_{pq}? Does the phase carry useful information?

A2: In converting an S_{vv} image into a σ^0_{vv} image, only the magnitude of S_{vv} is used, so the phase is unnecessary. The absolute phase of S_{vv} is not important, but the phase of S_{vv} relative to the phases of S_{hh} and S_{hv} is very important. The relative phases, particularly the co-pol phase ϕ_c, carry information about the target.

Q3: What is polarization synthesis?

A3: Given the matrix $\mathbf{S}$ for a point or distributed target, it is possible to generate the response that the radar would measure for any specified combination of linear, circular, or elliptical polarizations. If a certain application calls for measuring the RCS of a target (or the reflectivity of terrain) using a v-polarized antenna for transmission and a right-hand circularly polarized antenna for reception, polarization synthesis provides the analytical tools for computing that RCS from the scattering matrix $\mathbf{S}$ without having to actually build a radar with that specific transmit/receive antenna polarization configuration.

5-11.1 RCS Polarization Response

Using the matrix notation given by Eq. (5.3), the electric field of a propagating EM wave is given by

$$\mathbf{E} = \begin{bmatrix} E_v \\ E_h \end{bmatrix} = \begin{bmatrix} a_v \\ a_h e^{j\delta} \end{bmatrix}. \tag{5.132}$$

Because the polarization state of the wave depends on the phase of E_h relative to that of E_v—rather than on the absolute values of the two phases—we set $\delta_v = 0$ and define δ as the phase difference between E_h and E_v. Furthermore, the magnitudes are defined such that $a_h \geq 0$ and $a_v \geq 0$, and their ratio is related to the auxiliary angle α by

$$\tan\alpha = \frac{a_h}{a_v}. \tag{5.133}$$

Per Eq. (5.5), each pair of values of angles (α, δ) defines a polarization ellipse with polarization angles (ψ, χ) given by

$$\tan 2\psi = (\tan 2\alpha)\cos\delta \qquad (-\pi/2 \leq \psi \leq \pi/2), \tag{5.134a}$$

$$\sin 2\chi = (\sin 2\alpha)\sin\delta \qquad (-\pi/4 \leq \chi \leq \pi/4), \tag{5.134b}$$

with the additional constraint that $\psi > 0$ if $\cos\delta > 0$ and $\psi < 0$ if $\cos\delta < 0$.

Conversely, angles (α, δ) are derived from (ψ, χ) through

$$\cos 2\alpha = (\cos 2\chi)(\cos 2\psi), \tag{5.135a}$$

$$\tan\delta = \frac{\tan 2\chi}{\sin 2\psi}. \tag{5.135b}$$

A transmit antenna radiating a wave with a polarization state defined by angles (α_t, δ_t), or equivalently, polarization angles (ψ_t, χ_t), is said to have an ***antenna polarization vector*** $\mathbf{p}^t$ given by

$$\mathbf{p}^t = \frac{\mathbf{E}_t}{|\mathbf{E}_t|} = \frac{1}{\sqrt{a_{v_t}^2 + a_{h_t}^2}} \begin{bmatrix} a_{v_t} \\ a_{h_t} e^{j\delta_t} \end{bmatrix} = \begin{bmatrix} \cos\alpha_t \\ \sin\alpha_t\, e^{j\delta_t} \end{bmatrix}. \tag{5.136}$$

Similarly, in the BSA convention, for a receive antenna configured to intercept waves with polarization states defined by (α_r, δ_r), or equivalently by polarization angles (ψ_r, χ_r), its antenna polarization vector is

$$\mathbf{p}^r = \begin{bmatrix} \cos\alpha_r \\ \sin\alpha_r\, e^{j\delta_r} \end{bmatrix}. \tag{5.137}$$

If a radar with transmit and receive antenna polarization vectors $\mathbf{p}^t$ and $\mathbf{p}^r$—both defined in the BSA

convention—is used to observe a target with scattering matrix $\mathbf{S}$, the radar would measure a radar cross section σ_{rt} given by (Kennaugh, 1951)

$$\sigma_{rt}(\psi_r, \chi_r; \psi_t, \chi_t) = 4\pi |\mathbf{p}^r \cdot \mathbf{S}\, \mathbf{p}^t|^2. \quad (5.138)$$

(point target)

This is known as the ***polarization synthesis equation***. It allows us to compute the RCS σ of a point target, or σ/A of a distributed target with resolution cell area A, for any specified combination of transmit/receive antenna polarizations. As an example, let us consider a large metal sphere with radius $a \gg \lambda$. Its scattering matrix in the BSA convention is given by

$$\mathbf{S} = \frac{a}{2}\begin{pmatrix} 1 & 0 \\ 0 & 1 \end{pmatrix} \quad \textbf{(metal sphere)}. \quad (5.139)$$

In view of its symmetry, the sphere does not generate cross-polarized components ($S_{hv} = S_{vh} = 0$) and it has the same scattering amplitudes for hh and vv polarizations. From among the infinite number of combinations of transmit/receive polarizations that can be synthesized using Eq. (5.138), two subsets of specific interest are:

(a) The ***co-polarized response***: which encompasses the full range of (ψ_t, χ_t) such that the antenna polarizations are always the same: $\mathbf{p}^t = \mathbf{p}^r$, $\psi_t = \psi_r$, and $\chi_t = \chi_r$. The normalized plot of σ as a function of ψ_t and χ_t is called the co-pol response. The co-pol response for the metal sphere is shown in Fig. 5-37(a).

(b) The ***cross-polarized response***: receive antenna polarization is always orthogonal to the transmit antenna polarization. If the transmit antenna is v-polarized ($\mathbf{p}^t = \hat{\mathbf{v}}$), the receive antenna is h-polarized ($\mathbf{p}^r = \hat{\mathbf{h}}$); if $\mathbf{p}^t$ represents a RHC-polarization state, then $\mathbf{p}^r$ represents a LHC-polarization state, and so on. The cross-pol response of the metal sphere is displayed in Fig. 5-37(a) also.

Parts (b) through (f) of Fig. 5-37 display the co-polarized and cross-polarized responses for the following point targets:

(1) Dihedral metal reflector aligned with respect to the radar for maximum return. Its scattering matrix is given by Jasik (1961) as

$$\mathbf{S} = \frac{k_0 ab}{\pi}\begin{pmatrix} -1 & 0 \\ 0 & 1 \end{pmatrix}. \quad (5.140)$$

where $k_0 = 2\pi/\lambda$ is the wavenumber in free space.

(2) Trihedral metal reflector aligned with respect to the radar for maximum return (radar beam points towards the trihedral's vortex). Its scattering matrix is given (Ruck et al., 1970) as

$$\mathbf{S} = \frac{k_0 l^2}{\sqrt{2}\,\pi}\begin{pmatrix} 1 & 0 \\ 0 & 1 \end{pmatrix}. \quad (5.141)$$

Since the form of $\mathbf{S}$ of the trihedral reflector is the same as that of the sphere, the polarization responses of the two point targets look identical.

(3) Thin conducting cylinder of length l (with $l \ll \lambda$) and radius a (with $a \ll \lambda$), oriented at an angle μ (measured in the clockwise direction) relative to the unit vector $\hat{\mathbf{h}}_t$ of the transmit antenna. Its scattering matrix is given by Ruck et al. (1970) as

$$\mathbf{S} = \frac{k_0^2 l^3}{3[\ln(4l/a) - 1]}\begin{pmatrix} \sin^2\mu & -\sin\mu\cos\mu \\ -\sin\mu\cos\mu & \cos^2\mu \end{pmatrix}. \quad (5.142)$$

The responses shown in Fig. 5-37(d), (e), and (f) correspond to $\mu = 0$ (horizontal wire), $\mu = 45°$, and $\mu = 90°$ (vertical wire), respectively.

5-11.2 Distributed Targets

Polarization synthesis also can be applied to radar images. A terrain-imaging polarimetric radar generates *complex* images of S_{vv}, S_{hh}, and S_{hv} (or S_{vh} since $S_{hv} = S_{vh}$). For a distributed target occupying N_c cells each of area A, its polarization synthesis equation is given by

$$\sigma^0_{rt}(\psi_r, \chi_r; \psi_t, \chi_t) = \frac{4\pi}{AN_c}\sum_{i=1}^{N_c} |\mathbf{p}^r \cdot \mathbf{S}_i \mathbf{p}^t|^2 = \frac{4\pi}{A}\left\langle |\mathbf{P}^r \cdot \mathbf{S}\mathbf{p}^t|^2 \right\rangle, \quad (5.143)$$

(distributed target)

[†] **Computer Code 5.1.**

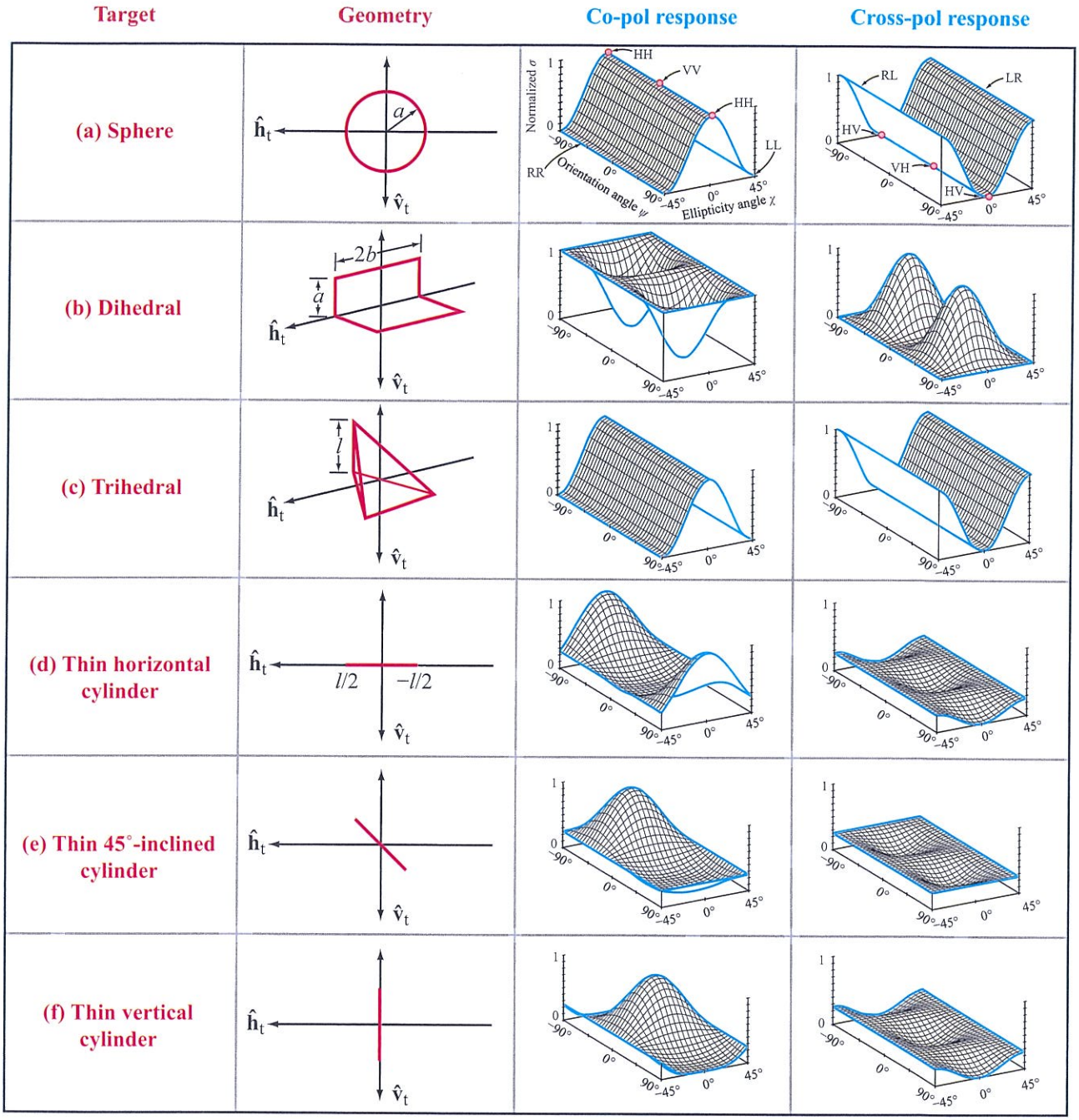

Figure 5-37: Co-pol and cross-pol responses of 6 point targets. LR stands for a left-hand (receive)/right-hand (transmit) polarization configuration.

where $\mathbf{S}_i$ is the scattering matrix of the ith cell. Of course, N_c should be a large number in order for the computation to yield an accurate estimate of the true value of σ^0_{rt}.

5-11.3 Mueller Matrix Approach

Instead of synthesizing the measured backscatter N_c times and then averaging the sum to obtain σ^0, as outlined by Eq. (5.143), it is possible to use a computationally more efficient approach based on the modified Mueller matrix representation of the polarized scattering by a target, instead of the scattering matrix $\mathbf{S}$. To show the procedure, we start by reintroducing the ***modified Stokes vector*** given by Eq. (5.23a) and then defining its elements in terms of the polarization angles given by Eqs. (5.5) and (5.6). For the transmit Stokes vector, the process leads to (Ulaby and van Zyl, Ch. 1, in Ulaby and Elachi, 1990):

$$\begin{aligned}\mathbf{I}^t(\psi,\chi) &= \begin{bmatrix} |E^t_v|^2 \\ |E^t_h|^2 \\ 2\Re e(E^t_v E^{t*}_h) \\ 2\Im m(E^t_v E^{t*}_h)\end{bmatrix} \Big/ \eta \\ &= \begin{bmatrix} {a^t_v}^2 \\ {a^t_h}^2 \\ 2a^t_v a^t_h \cos\delta_t \\ 2a^t_v a^t_h \sin\delta_t\end{bmatrix} \Big/ \eta \\ &= \begin{bmatrix} \frac{1}{2}(1+\cos 2\psi_t \cos 2\chi_t) \\ \frac{1}{2}(1-\cos 2\psi_t \cos 2\chi_t) \\ \sin 2\psi_t \cos 2\chi_t \\ \sin 2\chi_t\end{bmatrix} I^t_0, \end{aligned} \tag{5.144}$$

where the ***total intensity*** $I^t_0 = ({a^t_v}^2 + {a^t_h}^2)/\eta$. The four elements of the vector $\mathbf{I}^t$ are defined in terms of the same quantities that define $\mathbf{E}$ in Eq. (5.132), namely a_v, a_h, and δ.

> ► Whereas the elements of $\mathbf{E}$ are electric field components and one of them may be either real or complex, the elements of $\mathbf{I}^t$ represent power and all are real quantities. ◄

Similarly, the modified Stokes vector of the received wave is related to polarization angles (ψ_r, χ_r) by

$$\mathbf{I}^r = \begin{bmatrix} \frac{1}{2}(1+\cos 2\psi_r \cos 2\chi_r) \\ \frac{1}{2}(1-\cos 2\psi_r \cos 2\chi_r) \\ \sin 2\psi_r \cos 2\chi_r \\ \sin 2\chi_r\end{bmatrix} I^r_0. \tag{5.145}$$

The modified Stokes vectors of the transmitted and received waves are related through Eq. (5.25a), namely

$$\mathbf{I}^r = \frac{1}{R_r^2}\,\mathbf{M}\,\mathbf{I}^t, \tag{5.146}$$

where R_r is the range between the target and the radar antenna, and $\mathbf{M}$ is the modified Mueller matrix of the target, defined in the BSA coordinate system. From Eq. (5.25c),

$$\mathbf{M} = \begin{bmatrix} |S_{vv}|^2 & |S_{vh}|^2 & \cdots \\ |S_{hv}|^2 & |S_{hh}|^2 & \\ 2\Re e(S_{vv}S^*_{hv}) & 2\Re e(S_{vh}S^*_{hh}) & \\ 2\Im m(S_{vv}S^*_{hv}) & 2\Im m(S_{vh}S^*_{hh}) & \end{bmatrix}$$
$$\begin{bmatrix} \Re e(S_{vv}S^*_{vh}) & -\Im m(S_{vv}S^*_{vh}) \\ \Re e(S_{hv}S^*_{hh}) & -\Im m(S_{hv}S^*_{hh}) \\ \Re e(S_{vv}S^*_{hh}+S_{vh}S^*_{hv}) & -\Im m(S_{vv}S^*_{hh}-S_{vh}S^*_{hv}) \\ \Im m(S_{vv}S^*_{hh}+S_{vh}S^*_{hv}) & \Re e(S_{vv}S^*_{hh}-S_{vh}S^*_{hv}) \end{bmatrix}. \tag{5.147}$$

The 16 elements of $\mathbf{M}$ are real quantities related to various combinations of the elements of $\mathbf{S}$.

For a point target, the following polarization synthesis equation is applicable (Kennaugh, 1951; van Zyl et al., 1987a):

$$\sigma_{rt}(\psi_r,\chi_r;\,\psi_t,\chi_t) = 4\pi \mathbf{I}^r_n \cdot \mathbf{Q}\,\mathbf{M}\,\mathbf{I}^t_n, \tag{5.148}$$

(point target)

where $\mathbf{I}^r_n = \mathbf{I}^r/I^r_0$ and $\mathbf{I}^t_n = \mathbf{I}^t/I^t_0$, and

$$\mathbf{Q} = \begin{bmatrix} 1 & 0 & 0 & 0 \\ 0 & 1 & 0 & 0 \\ 0 & 0 & 1/2 & 0 \\ 0 & 0 & 0 & -1/2 \end{bmatrix}. \tag{5.149}$$

In the case of a distributed target for which N_c measurements of $\mathbf{M}$ are available, the reflectivity σ^0 can be synthesized for any transmit and receive antenna polarizations from†

$$\sigma^0_{rt}(\psi_r, \chi_r; \psi_t, \chi_t) = \frac{4\pi}{A} \mathbf{I}^r_n \cdot \mathbf{Q} \langle \mathbf{M} \rangle \mathbf{I}^t_n, \qquad (5.150)$$

(distributed target)

where

$$\langle \mathbf{M} \rangle = \frac{1}{N_c} \sum_{i=1}^{N} \mathbf{M}_i. \qquad (5.151)$$

Because the averaging over the index i is performed prior to applying Eq. (5.150), this approach has been found to be computationally superior to the direct synthesis approach presented in Section 5-11.2.

Figure 5-38 shows a number of synthesized images for the San Francisco Bay area in California. The data were acquired with the NASA/JPL AIRSAR system at L-band. The radar look direction for these images is from left to right. The Golden Gate Bridge is the linear feature at the top middle of the image. The Golden Gate Park is the large rectangle about 1/3 from the bottom of the image. Note the strong pixel-to-pixel variation in the relative return from the urban areas in the image (top left). These are related to the orientation of the buildings and the streets relative to the radar look direction (Zebker et al., 1987). When the streets are oriented nearly orthogonal to the radar look direction, the dominant scattering mechanism is that of a dihedral corner reflector formed by a street as the horizontal surface, and the front face of a building as the vertical surface. Double reflections tend to result in strong signals as evidenced by the bright areas in the city. Also note that the contrast between the urban areas and the vegetated areas, such as Golden Gate Park, is maximized using the 45-degree linear polarization for transmit, and 135-degree linear polarization for receive, as shown by the image on the right in the middle row. This is the polarization that generally maximizes the contrast between areas that exhibit double-reflection scattering and those that exhibit either odd numbers of reflections, or diffuse scattering (see Chapter 7 of Ulaby and Elachi (1990) for a more detailed discussion).

In a second example, we show in Fig. 5-39 a similar set of synthesized images for a portion of the Florida coastline, acquired at L-band with the NASA/JPL UAVSAR system. The large body of water is part of Choctawhatchee Bay, and the urban areas to the left of the bay in the image are the cities of Valparaiso and Niceville. The bright line near the top right of the image is where the Mid Bay Bridge Road crosses Choctawhatchee Bay. This set of images shows that for natural vegetation, there is generally less variation in radar backscatter with changing polarization than with urban areas. The exception is the case where there is standing water under vegetation, where, at long wavelengths, double reflections from the water surface to the tree trunks and back to the radar tend to dominate the scattered signals. In this image, the bright area near the top left of the hh image (top left image in the series) is such an area. Note how there is more contrast between the vegetation with standing water and the surrounding vegetation in the hh image than in the vv image (center image top row). Double reflections from dielectric surfaces tend to be stronger at hh than at vv, because the Fresnel reflection coefficient is stronger for horizontal polarization than for vertical polarization. Natural vegetation with nearly uniform orientation shows little difference between hh and vv scattering. In fact, if the vegetation is uniformly randomly oriented, hh and vv scattering would be equal. The HV image (rightmost image in top row) does not show much contrast between the areas with standing water under the vegetation and the surrounding vegetation. This indicates that the cross-polarized return is mostly due to the randomly oriented parts of the vegetation canopy. Note, however, how the contrast between the vegetated and nonvegetated areas is the best in the hv image when comparing across the top row. This is expected because the cross-polarized return is mostly due to the randomly oriented parts of the vegetation canopy. Also note that the hv image shows subtle differences in the vegetated areas on the left edge of the image, where areas that were previously cleared and have since experienced regrowth are visible

† **Computer Code 5.1.**

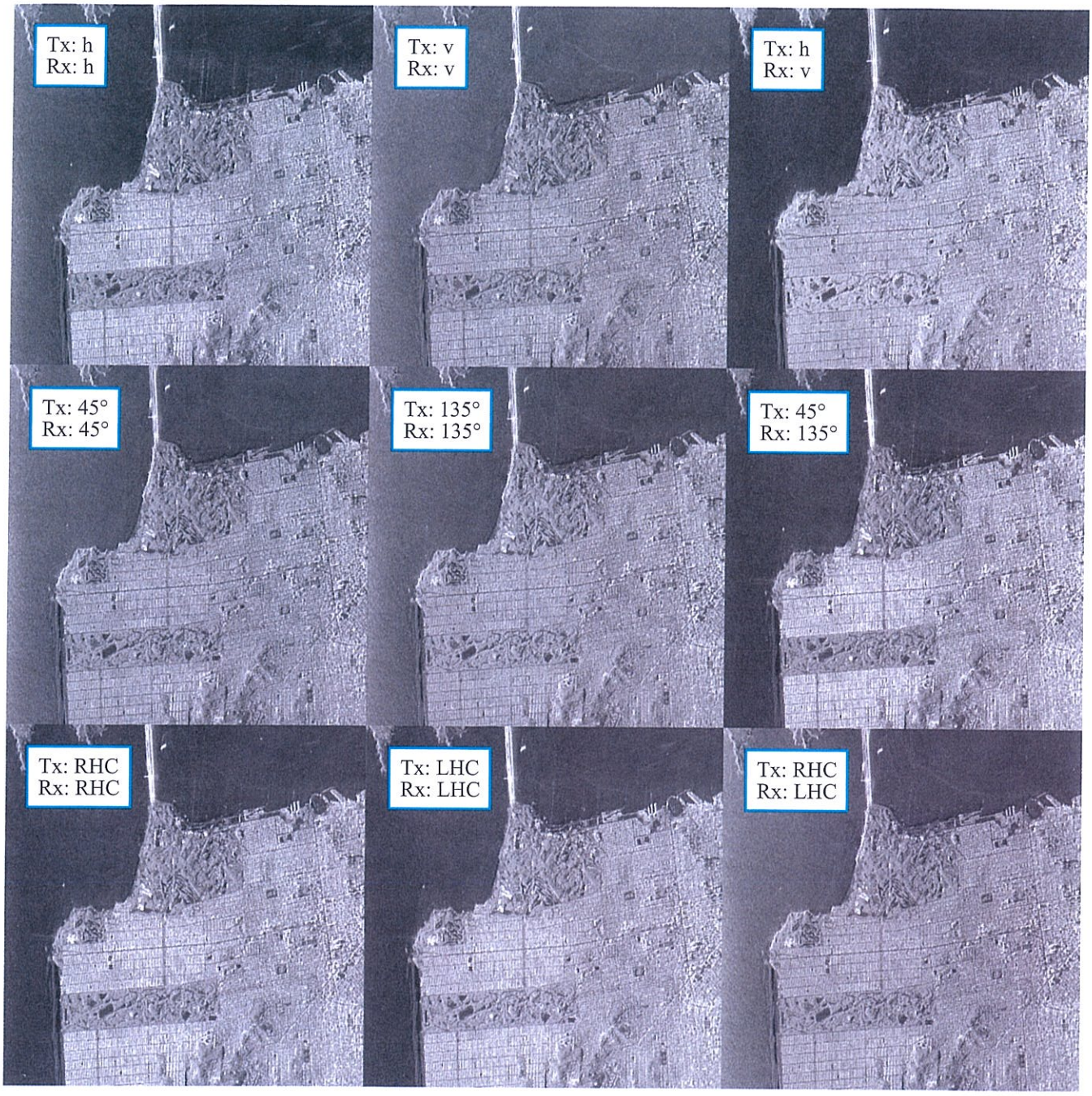

Figure 5-38: This series of L-band images of San Francisco were synthesized from a single polarimetric image acquired by the NASA/JPL AIRSAR system. The nine images include various combinations of co-polarized (transmit and receive polarizations are the same) and cross-polarized (transmit and receive polarizations are orthogonal) images. Note the relative change in brightness between the city of San Francisco, the ocean, and the Golden Gate Park, which is the large rectangle about 1/3 from the bottom of the images. The radar illumination is from the left.

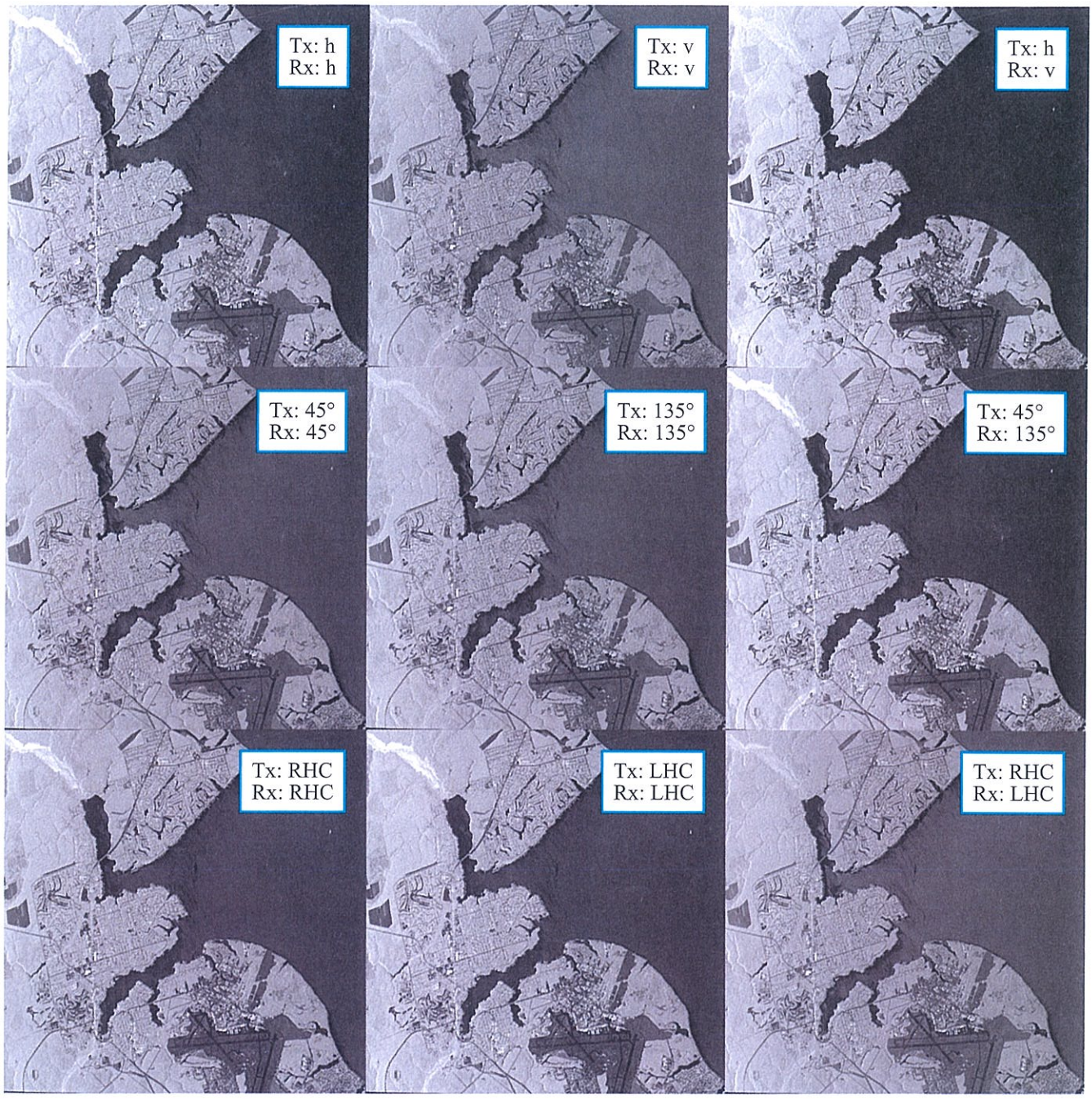

Figure 5-39: This series of L-band images of the Florida Coast were synthesized from a single polarimetric image acquired by the NASA/JPL UAVSAR system. Radar illumination is from the left. The large body of water is part of Choctawhatchee Bay. See the text for additional description of the area.

near the top on the left of the hv image. As in the case of the San Francisco image, the best contrast between the areas with standing water under the canopy and the surrounding vegetation is found when using the 45/135-degree cross-polarized linear polarizations, as can be seen in the center image of the right-hand column. Finally, the co-polarized circularly polarized images combine the characteristics of the hv image in that they show reasonable contrast between vegetated and nonvegetated areas, and like the 45/135-degree linear cross-polarized image, show good contrast between the areas with standing water under the vegetation and the surrounding areas.

5-12 Polarimetric Scattering Statistics

Consider a textureless distributed target (such as a random soil surface) imaged by a polarimetric radar. The target extent encompasses a large number of independent resolution cells N_c. Each cell is represented by a 1-look scattering matrix $\mathbf{S}$ from which we can generate hh-, vv-, and hv-polarized images by applying Eq. (5.131). As noted previously, $S_{hv} = S_{vh}$ in the backscatter mode.

If the radar uses linear detection, the tone of the hh-polarized amplitude image is proportional to $|S_{hh}|$ and the pdf of $|S_{hh}|$ (for the N_c image pixels) is given by the Rayleigh distribution of Eq. (5.75) with $f = |S_{hh}|/\langle|S_{hh}|\rangle$. The same statistics apply to the vv-polarized and hv-polarized images. Similarly, square-law detection generates an hh image whose tone is proportional to $|S_{hh}|^2$ and whose associated pdf is the exponential function given by Eq. (5.80a) with $F = |S_{hh}|^2/\langle|S_{hh}|^2\rangle$. *Our goal in this section is to examine the phase statistics of* $\mathbf{S}$.

In the backscatter mode, the scattering matrix of an image pixel,

$$\mathbf{S} = \begin{pmatrix} S_{vv} & S_{vh} \\ S_{hv} & S_{hh} \end{pmatrix} \tag{5.152}$$

consists of

$$S_{vv} = |S_{vv}|e^{j\phi_{vv}} = X_{vv} + jY_{vv}, \tag{5.153a}$$

$$S_{hh} = |S_{hh}|e^{j\phi_{hh}} = X_{hh} + jY_{hh}, \tag{5.153b}$$

$$S_{hv} = |S_{hv}|e^{j\phi_{hv}} = X_{hv} + jY_{hv}. \tag{5.153c}$$

In total, $\mathbf{S}$ consists of six real quantities, namely the three magnitudes ($|S_{vv}|$, $|S_{hh}|$, and $|S_{hh}|$) and three phase angles (ϕ_{vv}, ϕ_{hh}, ϕ_{hv}), or equivalently, of the three real parts (X_{vv}, X_{hh}, and X_{hv}) and three imaginary parts (Y_{vv}, Y_{hh}, and Y_{hv}) of the scattering amplitudes. In Section 5-7.1, we stated that for a textureless distributed target, the real and imaginary parts of the backscattered electric field—E_x and E_y defined by Eq. (5.56)—are both Gaussian-distributed. Within a calibration constant, $E_x = X_{vv}$ and $E_y = Y_{vv}$ (for vv polarization), so X_{vv} and Y_{vv} should be Gaussian-distributed also. The plots in Fig. 5-40 are pdfs of X_{vv} and Y_{vv} generated from 1000 radar measurements acquired by a track-mounted polarimetric scatterometer at 4.75 GHz. The target is a random soil surface. The two pdfs are indeed zero-mean Gaussian, and they have the same standard deviation (within measurement error). Similar results were observed for the hh- and hv-polarized data.

Individually, the phase angles ϕ_{vv}, ϕ_{hh}, and ϕ_{hv} are uniformly distributed over $[-\pi, \pi]$, and therefore they contain no information about the geometrical and dielectric properties of the distributed targets. However, their differences

$$\phi_c = \phi_{hh} - \phi_{vv} \qquad \textbf{(co-pol phase)}, \tag{5.154a}$$

and

$$\phi_x = \phi_{hv} - \phi_{vv} \qquad \textbf{(cross-pol phase)}, \tag{5.154b}$$

may or may not be uniformly distributed and may in fact be related to the target's properties. For most distributed targets, S_{vv} and S_{hh} are dominated by ***first-order scattering*** (direct backscatter with no multiple reflections), whereas S_{hv} and S_{vh} are due to second- and higher-order scattering (two or more reflections involving two or more scatterers). Consequently, S_{hv} and S_{vv} are uncorrelated random variables, and the phase difference ϕ_x is indeed uniformly distributed, as shown in Fig. 5-41(a). That is,

$$\langle S_{hv}S_{hh}^*\rangle = \langle S_{hv}S_{vv}^*\rangle = 0 \tag{5.154c}$$

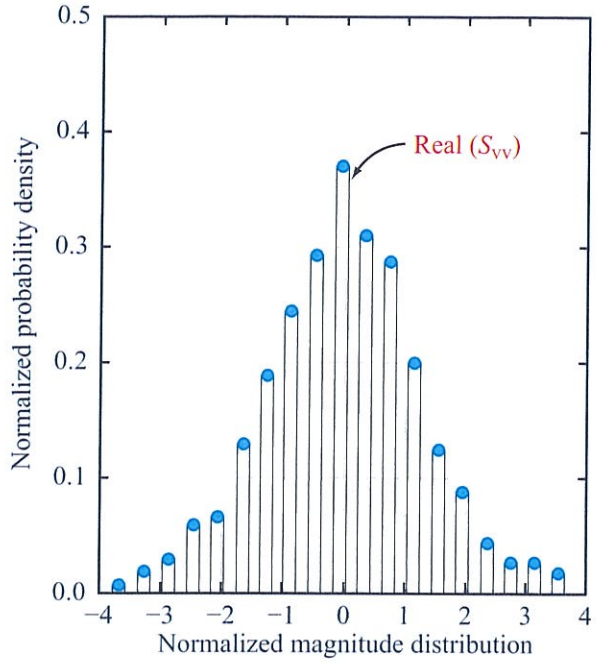

(a) $\mathrm{Re}(S_{vv}) = X_{vv}$

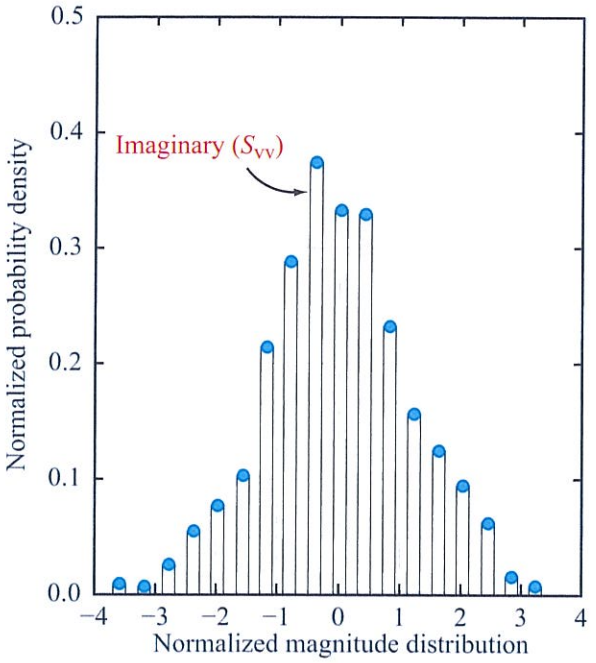

(b) $\mathrm{Im}(S_{vv}) = Y_{vv}$

Figure 5-40: Measured histograms of the real and imaginary parts of S_{vv} for a soil surface observed by a 4.75 GHz radar scatterometer [Sarabandi, 1992].

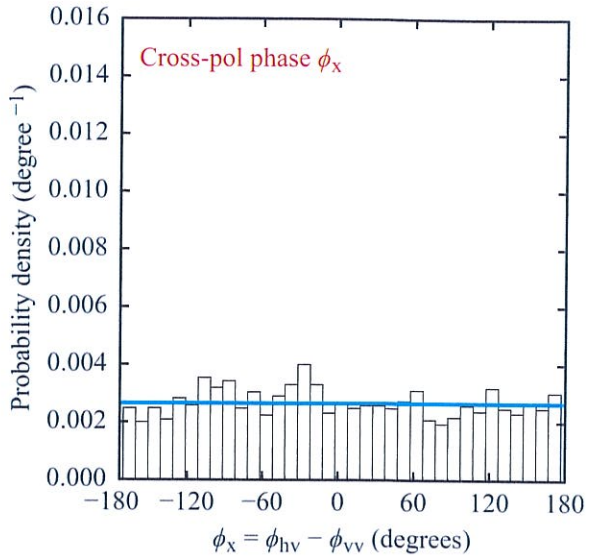

(a) Cross-pol phase

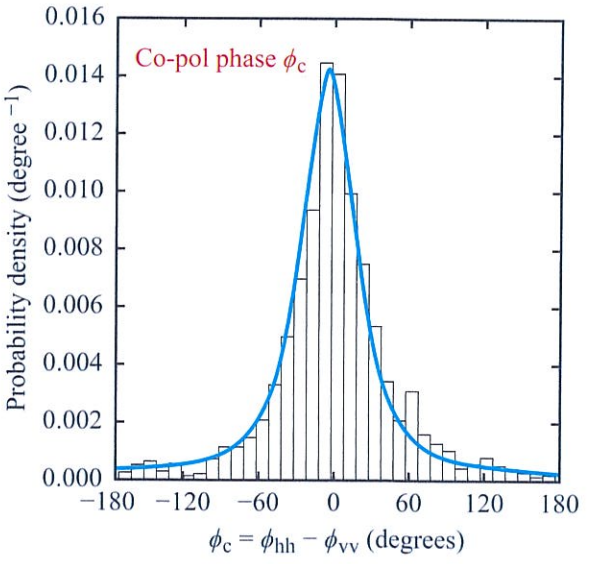

(b) Co-pol phase

Figure 5-41: Measured histograms of the cross-pol phase difference ϕ_x and the co-pol phase difference ϕ_c of a slightly rough soil surface [Sarabandi, 1992].

and

$$p(\phi_x) = \frac{1}{2\pi}, \qquad -\pi \le \phi \le \pi. \tag{5.154d}$$

In contrast, $p(\phi_c)$, the pdf of the co-pol phase difference ϕ_c, is approximately Gaussian, as shown in Fig. 5-41(b). Furthermore, as we show shortly, the mean value and variance of ϕ_c are directly related to the elements of the average Mueller matrix of the distributed target, $\langle \mathbf{M} \rangle$.

Based on the assumption that the co-polarized and cross-polarized scattering amplitudes are statistically uncorrelated, it follows that 8 of the 16 elements of the Mueller matrix given by Eq. (5.147) have zero average values. Hence,

$$\langle \mathbf{M} \rangle = \begin{bmatrix} M_{11} & M_{12} & 0 & 0 \\ M_{21} & M_{22} & 0 & 0 \\ 0 & 0 & M_{33} & M_{34} \\ 0 & 0 & M_{43} & M_{44} \end{bmatrix}, \tag{5.155}$$

with

$$M_{11} = \langle |S_{vv}|^2 \rangle, \qquad M_{22} = \langle |S_{hh}|^2 \rangle, \tag{5.156a}$$

$$M_{12} = M_{21} = \langle |S_{hv}|^2 \rangle, \tag{5.156b}$$

$$M_{33} = \langle |S_{vv}||S_{hh}| \cos\phi_c \rangle + M_{12}, \tag{5.156c}$$

$$M_{43} = -M_{34} = \langle |S_{vv}||S_{hh}| \sin\phi_c \rangle, \tag{5.156d}$$

$$M_{44} = \langle |S_{vv}||S_{hh}| \cos\phi_c \rangle - M_{12}. \tag{5.156e}$$

Using Rayleigh fading statistics, it can be shown that the pdf of the co-pol phase difference ϕ_c is given by (Sarabandi, 1992; Ulaby et al., 1992):

$$p(\phi_c) = \frac{a}{2\pi b}\left\{1 + c\left[\frac{\pi}{2} + \tan^{-1} c\right]\right\}, \tag{5.157}$$

where

$$a = 1 - \beta^2 \tag{5.158a}$$

$$b = 1 - \beta^2 \cos^2(\phi_c - \phi_0), \tag{5.158b}$$

$$c = \frac{\beta}{\sqrt{b}} \cos(\phi_c - \phi_0), \tag{5.158c}$$

$$\beta = \frac{1}{2}\left[\frac{(M_{33} + M_{44})^2 + (M_{34} - M_{43})^2}{M_{11} M_{22}}\right]^{1/2}, \quad 0 \le \beta \le 1, \tag{5.158d}$$

$$\phi_0 = \tan^{-1}\left(\frac{M_{34} - M_{43}}{M_{33} + M_{44}}\right), \qquad -\pi \le \phi_0 \le \pi. \tag{5.158e}$$

The parameter ϕ_0 is the value of ϕ_c at which $p(\phi_c)$ is a maximum, so it is called the ***highest likelihood co-pol phase difference***, and the parameter β is called the ***degree of co-pol correlation*** and it controls the width of the pdf. Figure 5-42 displays plots of $p(\phi_c)$ for various combinations of ϕ_0 and β, and Fig. 5-43 compares a histogram of measured values with the pdf based on Eq. (5.157) for a grassy area observed by a 1.2 GHz polarimetric SAR in April 1990.

Whereas a bare soil surface or a grassy field usually exhibits a pdf $p(\phi_c)$ with a mean value $\langle \phi_0 \rangle \approx 0$, $\langle \phi_0 \rangle$ may be much larger for vegetation canopies composed of plants with vertical stalks or trees with vertical trunks, particularly when imaged at large incidence angles. In Fig. 5-44, plots of $p(\phi_c)$ are shown for two fields of mature corn, one observed by a 1.2 GHz polarimetric SAR at an incidence angle of 19° and the other at 50°. Their pdfs have significantly different peak values, widths, and mean values.

In summary, a lot of evidence exists to suggest that the co-pol phase difference ϕ_c contains information about the physical and dielectric properties of a distributed target, but insufficient progress has been made to date to utilize such information in support of specific applications.

5-13 Polarimetric Analysis Tools

Even though the foundational principles of radar polarimetry were established well before 1980 (Kennaugh, 1951; Huynen, 1970; Boerner, 1981; Kostinski and Boerner, 1986), the implementation of the polarimetric radar concept in an imaging mode was not realized until 1985. In that year, the Jet Propulsion Laboratory successfully designed, constructed, and demonstrated the capabilities of the first polarimetric SAR to fly on an aircraft (van Zyl, 1985). Since then, the field of

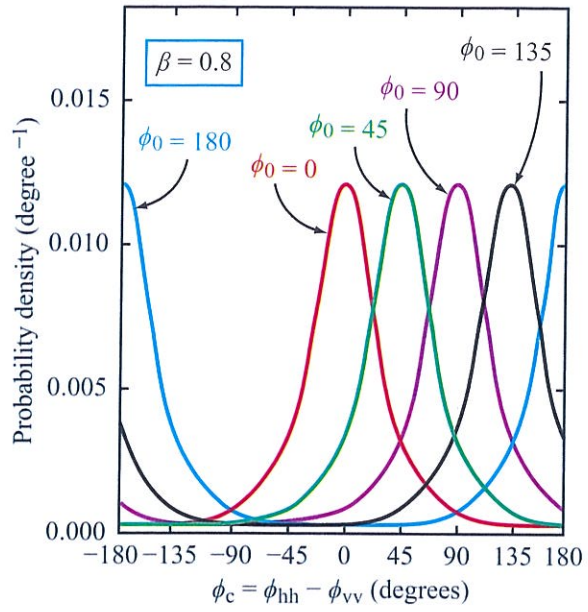

(a) $p(\phi_c)$ for various values of ϕ_0

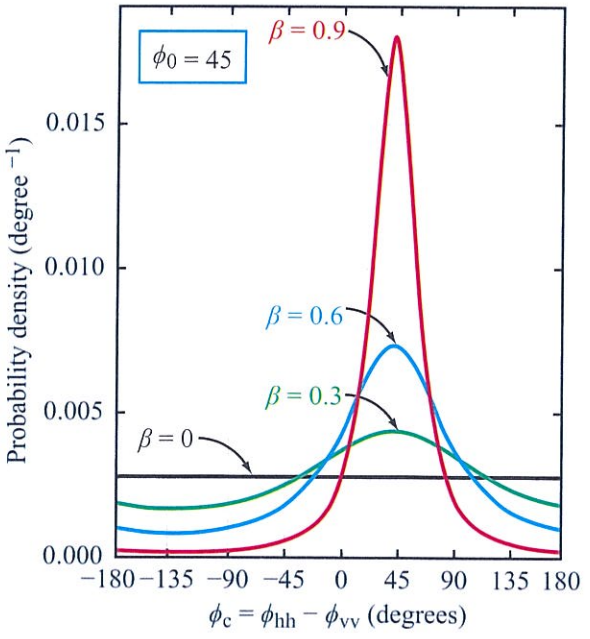

(b) $p(\phi_c)$ for various values of β

Figure 5-42: Plots of the pdf $p(\phi_c)$ of the co-pol phase difference ϕ_c for various combinations of ϕ_0 and β.

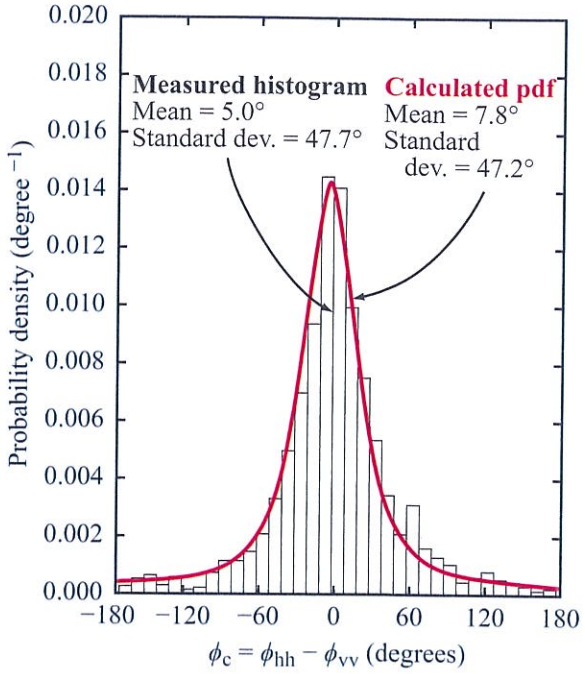

Figure 5-43: Comparison of the measured histogram of ϕ_c extracted from a 1.2 GHz SAR image with $p(\phi_c)$ given by Eq. (5.157).

radar polarimetry has expanded exponentially; several polarimetric SAR systems have been flown in space, numerous articles and books have been published on the subject (Ulaby and Elachi, 1990; Mott, 2007; Lee and Pottier, 2009; van Zyl and Kim, 2011), and numerous techniques and analysis tools have been developed to enhance target detection (Ioannidis and Hammers, 1979; Swartz et al., 1988) or extract information about an imaged scene from its polarimetric radar observations. In this section, we highlight some of these analysis tools and illustrate them with examples.

5-13.1 Scattering Covariance Matrix

Each pixel in a polarimetric radar image of a given scene is represented by a scattering matrix of the form given by

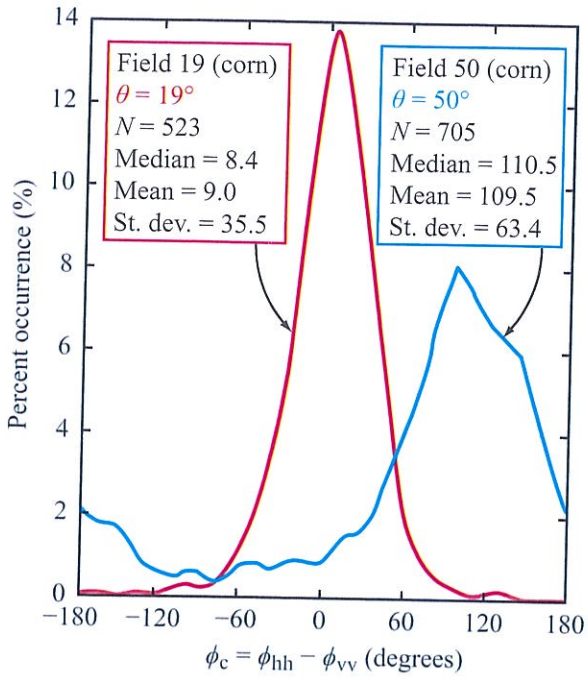

Figure 5-44: Measured histograms of ϕ_c for two cornfields, extracted from a 1.2 GHz SAR image.

Eq. (5.152), namely

$$\mathbf{S} = \begin{pmatrix} S_{vv} & S_{vh} \\ S_{hv} & S_{hh} \end{pmatrix}. \tag{5.159}$$

In Section 5-11, we demonstrated that it is possible to synthesize an image for any specified combination of transmit and receive polarizations. The polarization synthesis capability allows us to generate images that better discriminate between certain terrain types or better accentuate the appearance of certain terrain features such as boundaries. However, given that the number of possible polarization combinations is limitless, the process of identifying the *best* combination for a given application and a given imaged scene becomes a laborious search process. Fortunately, it is possible to mathematically solve for the optimum polarization combination that maximizes the backscatter from a certain type of target, or for the combination that maximizes the contrast between two types of targets. The details are available in the book by van Zyl and Kim (2011).

In the present section, we examine certain polarimetric attributes that have been found to provide useful information about polarimetrically imaged terrain. These attributes include:

(a) The ***target entropy*** (Cloude, 1992a; Cloude and Pottier, 1995), which describes the degree of randomness exhibited by the polarized return among the different pixels of a target type (such as a bare surface, a forest, or an urban area).

(b) The ***polarimetric pedestal*** (Durden et al., 1990), which is a measure of the degree of depolarization generated by a target.

(c) The ***radar vegetation index*** (RVI) introduced by Kim and van Zyl (2001) as a parameter with which to characterize the sizes of scattering cylinders (such as branches and needles in a vegetation canopy) relative to the wavelength λ.

Computing these or other polarimetric attributes is a multistep process that starts by computing the ***average covariance matrix*** $\langle \mathbf{C} \rangle$. For an image segment composed of N_c pixels of a distributed scene, with scattering matrices $\mathbf{S}_i$ where $i = 1, 2, \ldots, N_c$, the scattering coefficient is given by Eq. (5.143) as

$$\sigma^0_{rt}(\psi_r, \chi_r; \psi_t, \chi_t) = \frac{4\pi}{AN_c} \sum_{i=1}^{N_c} |\mathbf{p}^r \cdot \mathbf{S}_i \mathbf{p}^t|^2 = \frac{4\pi}{A} \langle |\mathbf{P}^r \cdot \mathbf{S}\mathbf{p}^t|^2 \rangle, \tag{5.160}$$

where $\mathbf{p}^t$ and $\mathbf{p}^r$ are the antenna polarization vectors defined by Eqs. (5.136) and (5.137):

$$\mathbf{p}^t = \begin{bmatrix} p^t_v \\ p^t_h \end{bmatrix} = \begin{bmatrix} \cos\alpha_t \\ \sin\alpha_t \, e^{j\delta_t} \end{bmatrix}, \tag{5.161a}$$

$$\mathbf{p}^r = \begin{bmatrix} p^r_v \\ p^r_h \end{bmatrix} = \begin{bmatrix} \cos\alpha_r \\ \sin\alpha_r \, e^{j\delta_r} \end{bmatrix}. \tag{5.161b}$$

The polarization states of the transmit and receive antennas are specified by the values of α_t, α_r, δ_t, δ_r, as described in Section 5-11.1. These four parameters specify, in turn, the polarization angles ψ_r, χ_r, ψ_t, and χ_t.

Covariance matrix in bistatic mode

By expanding the expression inside the magnitude sign in Eq. (5.160), it can be shown that

$$\mathbf{p}^{\mathrm{r}} \cdot \mathbf{S}_i \mathbf{p}^{\mathrm{t}} = \begin{bmatrix} p_{\mathrm{v}}^{\mathrm{r}} p_{\mathrm{v}}^{\mathrm{t}} \\ p_{\mathrm{v}}^{\mathrm{r}} p_{\mathrm{h}}^{\mathrm{t}} \\ p_{\mathrm{h}}^{\mathrm{r}} p_{\mathrm{v}}^{\mathrm{t}} \\ p_{\mathrm{h}}^{\mathrm{r}} p_{\mathrm{h}}^{\mathrm{t}} \end{bmatrix} \cdot \begin{bmatrix} S_{\mathrm{vv}} \\ S_{\mathrm{vh}} \\ S_{\mathrm{hv}} \\ S_{\mathrm{hh}} \end{bmatrix} = \mathbf{A} \cdot \mathbf{T}, \tag{5.162}$$

where

$$\mathbf{A} = \begin{bmatrix} p_{\mathrm{v}}^{\mathrm{r}} p_{\mathrm{v}}^{\mathrm{t}} \\ p_{\mathrm{v}}^{\mathrm{r}} p_{\mathrm{h}}^{\mathrm{t}} \\ p_{\mathrm{h}}^{\mathrm{r}} p_{\mathrm{v}}^{\mathrm{t}} \\ p_{\mathrm{h}}^{\mathrm{r}} p_{\mathrm{h}}^{\mathrm{t}} \end{bmatrix} \tag{5.163a}$$

and

$$\mathbf{T} = \begin{bmatrix} S_{\mathrm{vv}} \\ S_{\mathrm{vh}} \\ S_{\mathrm{hv}} \\ S_{\mathrm{hh}} \end{bmatrix}. \tag{5.163b}$$

It then follows that

$$|\mathbf{p}^{\mathrm{r}} \cdot \mathbf{S}_i \mathbf{p}^{\mathrm{t}}|^2 = (\mathbf{A} \cdot \mathbf{T})(\mathbf{T} \cdot \mathbf{A}) = \mathbf{A} \cdot \mathbf{T}\mathbf{T}^{\dagger}\mathbf{A}^* = \mathbf{A} \cdot \mathbf{C}\mathbf{A}^*, \tag{5.164}$$

where the symbol † denotes transpose complex conjugate, and the matrix

$$\mathbf{C} = \mathbf{T}\mathbf{T}^{\dagger} = \begin{bmatrix} S_{\mathrm{vv}}S_{\mathrm{vv}}^* & S_{\mathrm{vv}}S_{\mathrm{vh}}^* & S_{\mathrm{vv}}S_{\mathrm{hv}}^* & S_{\mathrm{vv}}S_{\mathrm{hh}}^* \\ S_{\mathrm{vh}}S_{\mathrm{vv}}^* & S_{\mathrm{vh}}S_{\mathrm{vh}}^* & S_{\mathrm{vh}}S_{\mathrm{hv}}^* & S_{\mathrm{vh}}S_{\mathrm{hh}}^* \\ S_{\mathrm{hv}}S_{\mathrm{vv}}^* & S_{\mathrm{hv}}S_{\mathrm{vh}}^* & S_{\mathrm{hv}}S_{\mathrm{hv}}^* & S_{\mathrm{hv}}S_{\mathrm{hh}}^* \\ S_{\mathrm{hh}}S_{\mathrm{vv}}^* & S_{\mathrm{hh}}S_{\mathrm{vh}}^* & S_{\mathrm{hh}}S_{\mathrm{hv}}^* & S_{\mathrm{hh}}S_{\mathrm{hh}}^* \end{bmatrix} \tag{5.165}$$

is called the ***covariance matrix*** of the scattering object or surface.

Covariance matrix in backscatter mode

In the general bistatic-scattering case, S_{vh} may be different from S_{hv}, but in the monostatic backscatter case, the reciprocity theorem dictates that $S_{\mathrm{vh}} = S_{\mathrm{hv}}$ [see Eq. (5.22b)]. Accordingly, vectors $\mathbf{A}$ and $\mathbf{T}$ can be reduced to 3×1 and the matrix $\mathbf{C}$ can be reduced to 3×3. These new versions are given by

$$\mathbf{A} = \begin{bmatrix} p_{\mathrm{v}}^{\mathrm{r}} p_{\mathrm{v}}^{\mathrm{t}} \\ \frac{1}{\sqrt{2}} (p_{\mathrm{v}}^{\mathrm{r}} p_{\mathrm{h}}^{\mathrm{t}} + p_{\mathrm{h}}^{\mathrm{r}} p_{\mathrm{v}}^{\mathrm{t}}) \\ p_{\mathrm{h}}^{\mathrm{r}} p_{\mathrm{h}}^{\mathrm{t}} \end{bmatrix}, \tag{5.166a}$$

$$\mathbf{T} = \begin{bmatrix} S_{\mathrm{vv}} \\ \sqrt{2}\, S_{\mathrm{vh}} \\ S_{\mathrm{hh}} \end{bmatrix}, \tag{5.166b}$$

and

$$\mathbf{C} = \begin{bmatrix} S_{\mathrm{vv}}S_{\mathrm{vv}}^* & \sqrt{2}\, S_{\mathrm{vv}}S_{\mathrm{vh}}^* & S_{\mathrm{vv}}S_{\mathrm{hh}}^* \\ \sqrt{2}\, S_{\mathrm{vh}}S_{\mathrm{vv}}^* & 2S_{\mathrm{vh}}S_{\mathrm{vh}}^* & \sqrt{2}\, S_{\mathrm{vh}}S_{\mathrm{hh}}^* \\ S_{\mathrm{hh}}S_{\mathrm{vv}}^* & \sqrt{2}\, S_{\mathrm{hh}}S_{\mathrm{vh}}^* & S_{\mathrm{hh}}S_{\mathrm{hh}}^* \end{bmatrix}. \tag{5.166c}$$

In view of Eqs. (5.160) and (5.164), the backscattering coefficient can be expressed in terms of the ***average scatterer covariance matrix*** $\langle \mathbf{C} \rangle$ as follows:

$$\begin{aligned} \sigma_{\mathrm{rt}}^0(\psi_{\mathrm{r}}, \chi_{\mathrm{r}};\ \psi_{\mathrm{t}}, \chi_{\mathrm{t}}) &= \frac{4\pi}{AN_{\mathrm{c}}} \sum_{i=1}^{N_{\mathrm{c}}} \mathbf{A} \cdot \mathbf{C}_i \mathbf{A}^* \\ &= \frac{4\pi}{AN_{\mathrm{c}}} \mathbf{A} \cdot \left(\sum_{i=1}^{N_{\mathrm{c}}} \mathbf{C}_i \right) \mathbf{A}^* \\ &= \frac{4\pi}{A} \mathbf{A} \cdot \langle \mathbf{C} \rangle \mathbf{A}. \end{aligned} \tag{5.167}$$

Given a segment of a polarimetric radar image with N_{c} pixels (representing a quasi-uniform distributed target such as a forest canopy), the measured scattering matrix of pixel i, $\mathbf{S}_i$, is used in Eq. (5.166c) to compute the corresponding covariance matrix $\mathbf{C}_i$. Upon averaging all of the $\mathbf{C}_i$ matrices, we obtain $\langle \mathbf{C} \rangle$. If N_{c} is sufficiently large, the off-diagonal terms of $\langle \mathbf{C} \rangle$ should be negligibly small and can be set equal to zero. This is because for a distributed target the co-pol and cross-pol components of $\mathbf{S}$ are uncorrelated, as was shown earlier in Section 5-12. Thus,

$$\langle \mathbf{C} \rangle = \begin{bmatrix} \langle S_{\mathrm{vv}}S_{\mathrm{vv}}^* \rangle & 0 & \langle S_{\mathrm{vv}}S_{\mathrm{hh}}^* \rangle \\ 0 & 2\langle S_{\mathrm{vh}}S_{\mathrm{vh}}^* \rangle & 0 \\ \langle S_{\mathrm{hh}}S_{\mathrm{vv}}^* \rangle & 0 & \langle S_{\mathrm{hh}}S_{\mathrm{hh}}^* \rangle \end{bmatrix}. \tag{5.168}$$

This is called the covariance matrix of a distributed target with ***reflection symmetry***.

The covariance matrix given by Eq. (5.168) is ***Hermitian*** and positive semidefinite, which means that none of its ***eigenvalues*** are negative. This follows from the way in which we constructed the covariance matrix.

▶ Hermitian matrices have the property that all their ***eigenvalues*** are real numbers and their ***eigenvectors*** form an orthonormal set. ◀

Cloude (1992b) was the first to use the orthonormality of the eigenvectors of the covariance matrix (in the context of radar polarimetry) to propose the ***decomposition*** of the covariance matrix in terms of its eigenvalues and eigenvectors, namely that $\langle \mathbf{C} \rangle$ can be expressed as

$$\langle \mathbf{C} \rangle = \sum_{j=1}^{3} \lambda_j \hat{\mathbf{e}}_j \hat{\mathbf{e}}_j^{\dagger}, \tag{5.169}$$

where λ_1 to λ_3 are the eigenvalues and $\hat{\mathbf{e}}_1$ to $\hat{\mathbf{e}}_3$ are the eigenvectors.

5-13.2 Eigenvector Decomposition

The decomposition expressed by Eq. (5.169) is unique. That is, since the eigenvectors of the covariance matrix are orthogonal, they form a natural basis in which to express the scattering. Note that in this decomposition, the eigenvector contains the information about the scattering mechanism, while the eigenvalue contains the information about the relative strength of that scattering mechanism compared to the others. Solution of the determinant of the matrix equation $\langle \mathbf{C} \rangle - \lambda \mathbf{I} = 0$, where $\mathbf{I}$ is the identity matrix, leads to

$$\lambda_1 = \frac{1}{2}\left\{ \langle S_{hh} S_{hh}^* \rangle + \langle S_{vv} S_{vv}^* \rangle + \sqrt{\left(\langle S_{hh} S_{hh}^* \rangle - \langle S_{vv} S_{vv}^* \rangle \right)^2 + 4 \left| \langle S_{hh} S_{vv}^* \rangle \right|^2} \right\}, \tag{5.170a}$$

$$\lambda_2 = \frac{1}{2}\left\{ \langle S_{hh} S_{hh}^* \rangle + \langle S_{vv} S_{vv}^* \rangle - \sqrt{\left(\langle S_{hh} S_{hh}^* \rangle - \langle S_{vv} S_{vv}^* \rangle \right)^2 + 4 \left| \langle S_{hh} S_{vv}^* \rangle \right|^2} \right\}, \tag{5.170b}$$

$$\lambda_3 = 2 \langle S_{hv} S_{hv}^* \rangle . \tag{5.170c}$$

All of these are real numbers, as expected for a Hermitian matrix.

The corresponding three eigenvectors are

$$\hat{\mathbf{e}}_1 = \frac{1}{\sqrt{\left[\langle S_{vv} S_{vv}^* \rangle - \langle S_{hh} S_{hh}^* \rangle + \sqrt{\Delta} \right]^2 + 4 \left| \langle S_{hh} S_{vv}^* \rangle \right|^2}} \cdot \begin{pmatrix} 2 \langle S_{hh} S_{vv}^* \rangle \\ 0 \\ \langle S_{vv} S_{vv}^* \rangle - \langle S_{hh} S_{hh}^* \rangle + \sqrt{\Delta} \end{pmatrix}, \tag{5.171a}$$

$$\hat{\mathbf{e}}_2 = \frac{1}{\sqrt{\left[\langle S_{vv} S_{vv}^* \rangle - \langle S_{hh} S_{hh}^* \rangle - \sqrt{\Delta} \right]^2 + 4 \left| \langle S_{hh} S_{vv}^* \rangle \right|^2}} \cdot \begin{pmatrix} 2 \langle S_{hh} S_{vv}^* \rangle \\ 0 \\ \langle S_{vv} S_{vv}^* \rangle - \langle S_{hh} S_{hh}^* \rangle - \sqrt{\Delta} \end{pmatrix}, \tag{5.171b}$$

$$\hat{\mathbf{e}}_3 = \begin{pmatrix} 0 \\ 1 \\ 0 \end{pmatrix}. \tag{5.171c}$$

In these expressions, we used the shorthand notation

$$\Delta = \left(\langle S_{vv} S_{vv}^* \rangle - \langle S_{hh} S_{hh}^* \rangle \right)^2 + 4 \left| \langle S_{hh} S_{vv}^* \rangle \right|^2 . \tag{5.172}$$

There are a couple of interesting properties to point out about the eigenvalues and eigenvectors in this case. First, eigenvalue λ_3 and its associated eigenvector $\hat{\mathbf{e}}_3$ depend on the cross-polarized return only, and the other two are purely made up of the co-polarized returns. This has led to the interpretation that the third eigenvector and its associated eigenvalue indicate the amount of diffuse scattering. The second point is that the first two eigenvectors show that the co-polarized phase of these two eigenvectors are 180 degrees different. Furthermore, their co-polarized amplitude ratios are the inverse of each other. It is easily shown from the expressions given by Eq. (5.171) that (van Zyl and Kim, 2011)

$$\frac{2 \langle S_{hh} S_{vv}^* \rangle}{\langle S_{vv} S_{vv}^* \rangle - \langle S_{hh} S_{hh}^* \rangle + \sqrt{\Delta}} = \frac{\langle S_{vv} S_{vv}^* \rangle - \langle S_{hh} S_{hh}^* \rangle - \sqrt{\Delta}}{2 \langle S_{hh} S_{vv}^* \rangle^*} . \tag{5.173}$$

This means that the first two eigenvectors represent scattering matrices that are related to odd and even numbers of reflections. Without looking explicitly at the eigenvectors, however, it is not obvious as to which eigenvalue to associate with which scattering mechanism. Also, we should point out that these eigenvectors do not necessarily represent pure single or double reflections. The phase relationship between the two eigenvectors means that if one eigenvector is more similar to single (odd) reflections, i.e., its phase is closer to zero than to 180 degrees, then the other eigenvalue is associated with double (even) reflections.

5-13.3 Useful Polarimetric Parameters

Target entropy

There are several ways by which we can estimate the amount of randomness exhibited in the state of the polarization of the wave scattered by the various resolution cells of the distributed target. Cloude (1992b), for example, defined ***target entropy*** as

$$H_T = -\sum_{i=1}^{3} P_i \log_3 P_i, \tag{5.174}$$

where

$$P_i = \frac{\lambda_i}{\lambda_1 + \lambda_2 + \lambda_3}. \tag{5.175}$$

As pointed out by Cloude, the target entropy H_T is a measure of target disorder, with $H_T = 1$ for highly random targets with equal eigenvalues, and $H_T = 0$ for simple, single, nonrandom targets.

Polarimetric pedestal

Figure 5-45 displays co-pol responses for a point target, namely a sphere, and three distributed targets representing an ocean surface, an urban area, and a city park. For the point target, the co-pol response is computed by applying the polarization synthesis equation given by Eq. (5.138) for all possible polarizations (such that the transmit and receive polarizations are always the same). A similar process

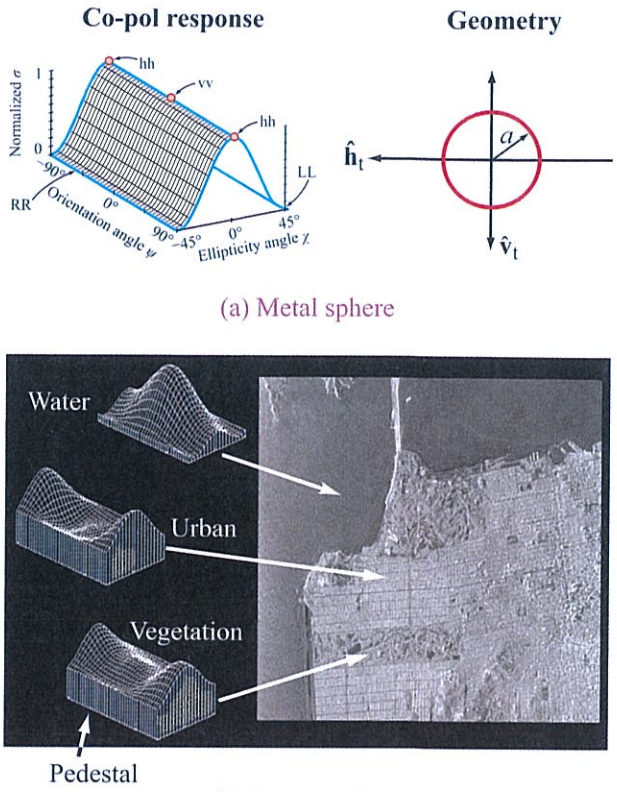

(a) Metal sphere

(b) San Francisco

Figure 5-45: Co-pol responses for (a) a metal sphere and (b) three areas in the San Francisco image.

applies to each of the three different distributed targets, except that for each polarization the process is repeated for all pixels of the distributed target and then averaged according to Eq. (5.143). Note that the minimum response for the point target is zero. It occurs when the receive/transmit polarization combination is RR or LL, where R and L stand for right-hand circular and left-hand circular. The co-pol response in Fig. 5-45(a) has no "pedestal," whereas the co-pol responses of the distributed targets do. The pedestal is small for the ocean surface and large for the urban and the city park. Distributed targets that generate significant multiple scattering have significant pedestal heights.

Durden et al. (1990) showed that measuring the pedestal height is equivalent to measuring the ratio of

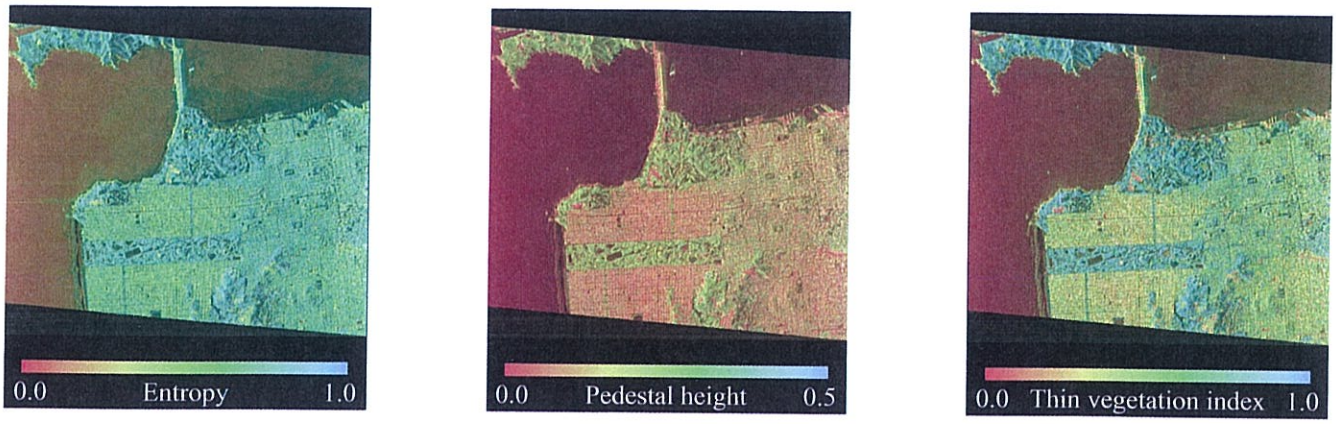

(a) Entropy (b) Pedestal (c) RVI

Figure 5-46: Radar images of San Francisco showing the three measures of scattering randomness: (a) entropy scaled from 0 (black) to 1 (white); (b) pedestal height scaled from 0 (black) to 0.5 (white); and (c) the radar vegetation index scaled from 0 (black) to 1 (white).

the minimum eigenvalue to the maximum eigenvalue:

$$P_{\mathrm{H}} = \frac{\min(\lambda_1, \lambda_2, \lambda_3)}{\max(\lambda_1, \lambda_2, \lambda_3)} . \tag{5.176}$$

Radar vegetation index

Kim and van Zyl (2001) introduced a parameter for volume scattering media, such as vegetation canopies, and they named it the ***radar vegetation index*** (RVI). The RVI is defined as

$$\mathrm{RVI} = \frac{4\min(\lambda_1, \lambda_2, \lambda_3)}{\lambda_1 + \lambda_2 + \lambda_3} . \tag{5.177}$$

By modeling a vegetation canopy as a collection of randomly oriented cylinders of length l and diameter d, Kim and van Zyl (2001) evaluated the RVI as a function of d/λ, where λ is the EM wavelength. Their results indicate that RVI approaches 1 when $d/\lambda \ll 1$ and approaches 0 when d approaches l (that is, when the cylinder becomes like a disc). Hence, the RVI provides information about the canopy architecture (at the needle and small branch scale) that may prove useful in distinguishing between different types of canopies.

5-13.4 Image Examples

The three polarimetric parameters introduced in the preceding subsection are different measures of ***polarization randomness*** of a distributed target. The similarities between the three polarization randomness parameters are illustrated in Fig. 5-46 using the image of San Francisco introduced earlier. From the polarization responses displayed in Fig. 5-45, we expect a small amount of randomness for the ocean but a more significant amount for the vegetation-dominated area in the Golden Gate Park. As noted earlier, the height of the pedestal of the polarization response is a measure of polarization randomness. Except for scaling differences, the three images in Fig. 5-46 convey similar information about the imaged scene. The entropy image shows less color variation than the other two, and the pedestal height image shows the greatest dynamic range. The choice among the three parameters as terrain type discriminators is somewhat arbitrary.

Next, we investigate the RVI at three different frequencies over a portion of the Black Forest in

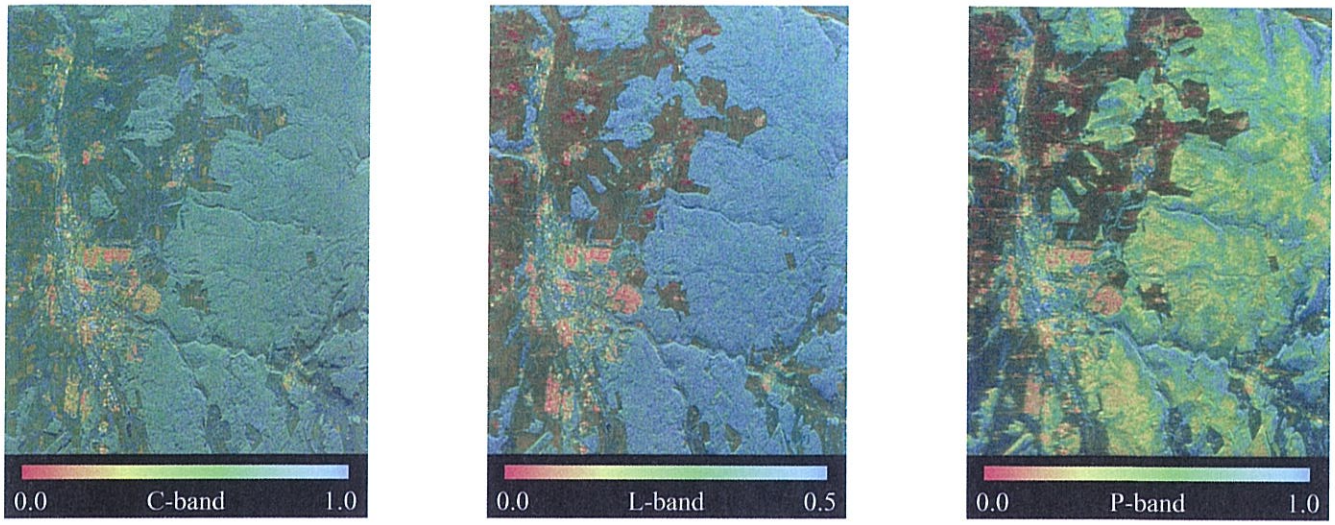

(a) C-band (b) L-band (c) P-band

Figure 5-48: RVI images of the area shown in Fig. 5-47 at three different frequencies. The RVI is scaled from 0 (black) to 1 (white). Note that the L-band RVI in the forested area is higher than the C-band RVI, while the C-band RVI is higher than the others in the agricultural areas..

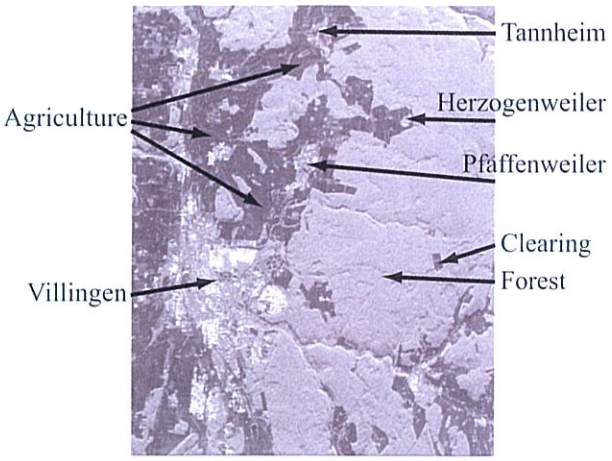

Figure 5-47: L-band total-power image of a portion of the Black Forest in Germany acquired with the NASA/JPL AIRSAR system in the summer of 1991. Radar illumination is from the top.

Germany acquired with the NASA/JPL AIRSAR system during the summer of 1991. The L-band image is shown for reference in Fig. 5-47. The bright feature in the left portion of the image is the town of Vilingen. The brighter right-hand portion of the image is a mixed forest consisting of spruce (*Picea abies*), pine (*Pinus sylvestris*) and fir (*Abies alba*) trees. The dry weight biomass ranges up to 50 kg/m^2. The darker areas in the upper portion and to the left in the image are mostly agricultural fields with varying amounts of biomass depending on the crop type and maturity of the plants.

Figure 5-48 compares the radar vegetation index at the three frequencies (C-band, L-band and P-band) of the AIRSAR system. The C-band image shows much higher values of the RVI in the agricultural areas, because the shorter wavelength is more sensitive to the smaller biomass in these fields. Fields with increased values of RVI generally had more vegetation on them at the time of acquisition. The forested area shows a high level of RVI at C-band, but somewhat less than some of the agricultural fields. The L-band image shows

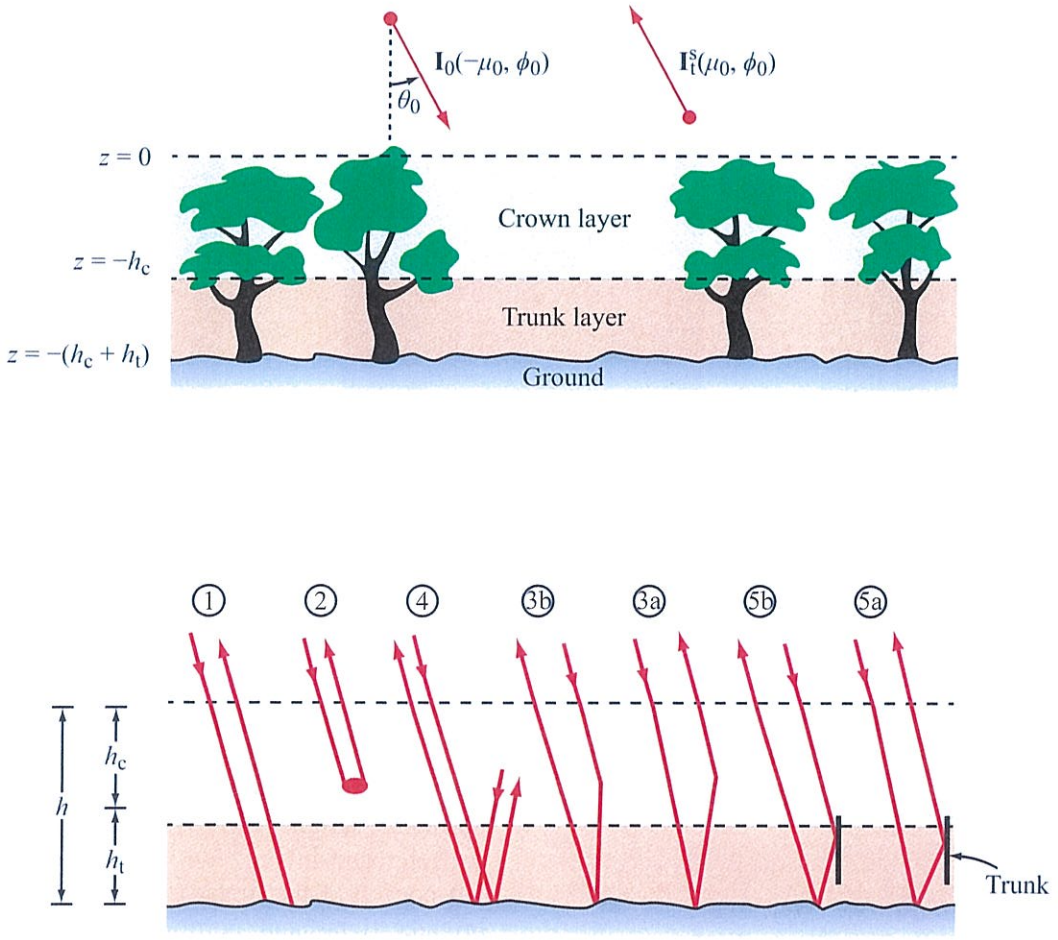

Figure 5-49: Scattering mechanisms for a forest canopy.

lower values of the RVI in the agricultural areas than the C-band image. This is consistent with the notion that L-band signals interact less with the relatively short vegetation than the shorter wavelength C-band signals. At L-band, the returns from the agricultural areas are probably still dominated by scattering from the underlying ground surface. The forest, on the other hand, shows a larger value of the RVI in the L-band than in the C-band image.

5-13.5 Freeman-Durden Decomposition

As discussed later in Section 11-13.3, the radar energy backscattered by a forest canopy contains contributions due to (a) direct scattering by the underlying ground surface, as depicted by ray 1 in Fig. 5-49, (b) direct and indirect scattering by the crown layer, depicted by rays 2, 3a, 3b, and 4 in Fig. 5-49, and (c) scattering by the ground-tree trunk combination, depicted by rays 5a and 5b. The ground-trunk scattering mechanism is an example of ***dihedral corner reflection***. Another example of this type of reflection is the reflection at

the corner between a ground surface and the vertical wall of a building. Accordingly, Freeman and Durden (1998) proposed a three-component decomposition for the covariance matrix of Eq. (5.168):

$$\langle \mathbf{C} \rangle = f_s \langle \mathbf{C}_s \rangle + f_d \langle \mathbf{C}_d \rangle + f_v \langle \mathbf{C}_v \rangle , \qquad (5.178)$$

where f_s, f_d, and f_v are the relative surface, dihedral, and volume contributions, and $\langle \mathbf{C}_s \rangle$, $\langle \mathbf{C}_d \rangle$, and $\langle \mathbf{C}_v \rangle$ are the associated covariance matrices. By applying certain assumptions about the sizes and orientation distributions of the volume scatterers in the crown layer, they were able to decompose the measured covariance matrix into its three components, as well as compute f_s, f_d, and f_v for every group of image pixels over which $\langle \mathbf{C} \rangle$ was measured. An example of their results is shown in Fig. 5-50 for the Black Forest area. The relative surface, dihedral, and volume contributions (f_s, f_d, and f_v) are displayed in blue, red, and green, respectively. The images in Fig. 5-50 indicate that volume scattering (represented by f_v in green) dominated in the vegetated areas, particularly at C-band where the penetration through the canopy is the smallest. The dihedral-corner mechanism (represented by f_d in red) is the dominant mechanism in the urban areas at all three frequencies. At P-band, where penetration through vegetation is the greatest, we see significant areas in yellow, which is a mixture of red and blue, indicating significant contributions due to both surface scattering (blue) and ground-trunk (red) reflections.

PROBLEMS

5.1 The scattering matrix of a dihedral corner reflector in the BSA convention is given by Eq. (5.140). Compute the corresponding modified Mueller matrix in the FSA convention.

5.2 Relate the modified Mueller matrix in the FSA convention to the modified Mueller matrix in the BSA convention.

5.3 The scattering matrix of a thin conducting cylinder is given by Eq. (5.142). Compute σ_{pq} for $pq =$ vv, vh, hv, and hh for a cylinder oriented at 45°. The cylinder is 3 cm long, its radius is 0.1 cm, and the frequency is 1 GHz.

5.4 A linear-detection radar is used to measure the backscatter from a large bare-soil field. Based on a large number of measurements, it was determined that the average value of the electric field amplitude is 0.2 V/m. Determine the most-probable single-observation electric field amplitude.

5.5 For a single radar observation, compute the lower and upper bounds in dB of the 75% range of fading for:

(a) Linear detection.

(b) Square-law detection.

5.6 Repeat Problem 5.5 for the average of three independent samples.

5.7 How many independent samples are required to reduce the 90% confidence interval for square-law detection to within ±0.3 dB?

5.8 Compute the normalized fading standard deviation for an $N = 2$ image generated by:

(a) Amplitude detection.

(b) Intensity detection.

(c) Square-root intensity detection.

5.9 An airborne sidelooking radar traveling at 200 m/s is used to measure the backscatter from a distributed target. The radar uses a 2 m long antenna, operates at 1 cm wavelength, and its detection mode is square-law. The target range is 10 km.

(a) Determine the 90% range of fading after averaging 4, 10, 100, and 1000 samples.

(b) As the radar beam sweeps across each resolution cell of width r_a, the number of independent samples inherent in the measured backscatter is $N_a = 2\beta_h^2 R/\lambda$ (from Eq. (14.123) in Chapter 14). Determine the distances that the radar has to travel so as to realize a total of $N = 4$, 10, 100, and 1000 samples.

5.10 The vertical ranges shown in Fig. 5-22(c) for $N = 16$ show no overlap between them. Does it then follow that it should always be possible to separate pixels of trees, grass, and soil from each other? Explain.

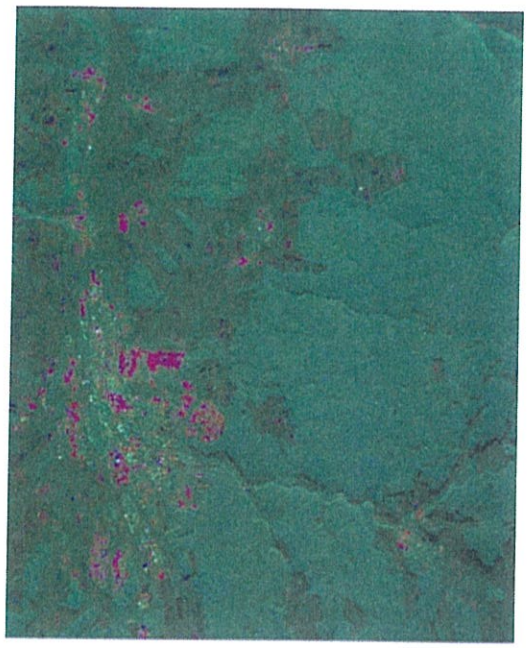

(a) C-band

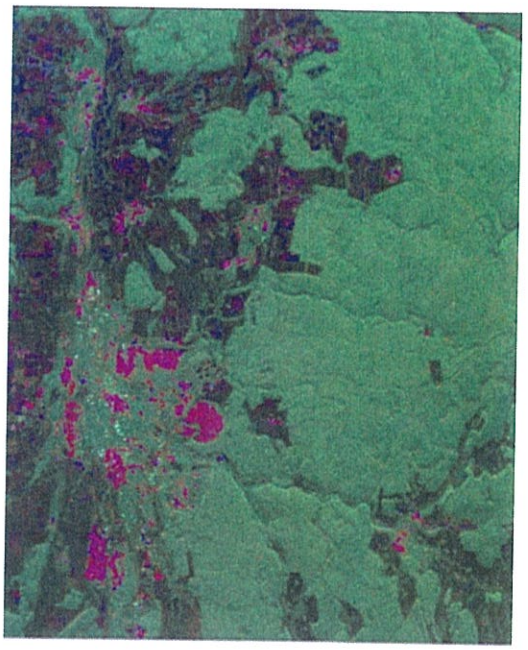

(b) L-band

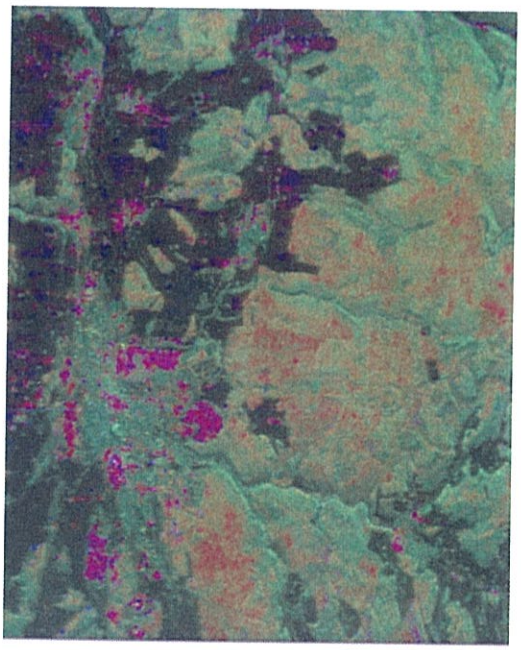

(c) P-band

Figure 5-50: Results of the Freeman-Durden decomposition for the Black Forest image at (a) C-band, (b) L-band, and (c) P-band. Surface, dihedral-corner, and volume scattering components are displayed in blue, red, and green colors, respectively.

5.11 What information about a random surface do the rms height and the correlation length convey? Explain with examples of smooth and rough surfaces.

5.12 A plane wave is incident at 30° upon a random surface with an rms height of 1 cm. Compute the ratio of the coherent reflectivity to the specular reflectivity at:

(a) $f = 0.5$ GHz.

(b) $f = 2$ GHz.

(c) $f = 10$ GHz.

5.13 Compute the hv-polarized radar cross section of a thin metal cylinder oriented at 30°, given that its length is 1 cm and its radius is 0.1 cm. The frequency is 3 GHz.

5.14 Select a polarimetric SAR image and then apply Computer Code 5.1 to generate images for the following combinations of receive/transmit polarizations:

(a) RHC/RHC.

(b) RHC/LHC.

(c) 45° Linear/LHC.

5.15 The average Mueller matrix of a soil surface measured by a polarimetric scatterometer is given by

$$\langle \mathbf{M} \rangle = \begin{bmatrix} 1.0 & 0.03 & 0 & 0 \\ 0.03 & 0.77 & 0 & 0 \\ 0 & 0 & 0.77 & -0.11 \\ 0 & 0 & 0.11 & 0.77 \end{bmatrix}.$$

Compute and plot the co-pol phase pdf.

5.16 The average covariance matrix of a grass-covered surface measured by a polarimetric radar in the BSA convention is given by

$$\langle \mathbf{C} \rangle = \begin{bmatrix} 1.0 & 0 & 0.7 \\ 0 & 0.06 & 0 \\ 0.7 & 0 & 0.9 \end{bmatrix}.$$

Compute:

(a) The target entropy.

(b) The pedestal height.

(c) The radar vegetation index.